

# Graphene on various substrates



Dissertation zur Erlangung  
des Doktorgrades der Naturwissenschaften  
(Dr. rer. nat.)  
der Fakultät Physik  
der Universität Regensburg

vorgelegt von  
Ulrich Wurstbauer geb. Stöberl  
aus  
Vilshofen an der Donau

2010

---

Promotionsgesuch eingereicht am: 12.01.2010

Die Arbeit wurde angeleitet von: Prof. Dr. Dieter Weiss

Prüfungsausschuss:

Vorsitzender: Prof. Dr. Milena Grifoni

Erstgutachter: Prof. Dr. Dieter Weiss

Zweitgutachter: Prof. Dr. Franz J. Gießibl

Weiterer Prüfer: Prof. Dr. Christian Schüller

Datum des Promotionskolloquiums: 29. 03. 2010

# Contents

<b>1</b>	<b>Introduction</b>	<b>1</b>
<b>2</b>	<b>Background</b>	<b>5</b>
2.1	Structural and electronic properties . . . . .	5
2.2	Transport properties . . . . .	12
2.2.1	Minimum Conductivity . . . . .	12
2.2.2	Quantum Hall effect . . . . .	13
2.2.3	Interference phenomena . . . . .	17
<b>3</b>	<b>Experimental methods</b>	<b>21</b>
3.1	Scanning electron microscope . . . . .	21
3.2	Atomic force microscope . . . . .	22
3.3	Imaging ellipsometry . . . . .	25
3.4	Magnetotransport measurements . . . . .	28
<b>4</b>	<b>Preparation and detection of graphene</b>	<b>31</b>
4.1	Fabrication of graphene samples . . . . .	31
4.1.1	Roads towards graphene . . . . .	31
4.1.2	Preparation of graphene on various substrate materials . . . . .	34
4.1.3	Preparation of graphene samples for electrical measurements . . . . .	37
4.2	Detection and the number of layers . . . . .	40
4.3	Detection methods – an overview . . . . .	51
<b>5</b>	<b>Mechanical and optical properties</b>	<b>53</b>
5.1	Mechanical Properties . . . . .	53
5.2	Optical Properties . . . . .	59

---

<b>6</b>	<b>Electronic Properties</b>	<b>63</b>
6.1	Transport behavior . . . . .	64
6.1.1	Contact and gate characteristics . . . . .	64
6.1.2	Temperature dependent intrinsic conductivity . . . . .	65
6.1.3	Charge neutrality point . . . . .	66
6.2	Magnetotransport behavior . . . . .	68
6.3	Aging process of graphene . . . . .	76
6.4	Phase coherent transport . . . . .	79
6.4.1	Weak localization . . . . .	79
6.4.2	Universal conductance fluctuations . . . . .	85
6.4.3	Comparison with graphene on SiO <sub>2</sub> . . . . .	85
6.5	Discussion . . . . .	86
<b>7</b>	<b>Conclusion</b>	<b>89</b>
<b>A</b>	<b>Abbreviations</b>	<b>92</b>
<b>B</b>	<b>Recipes</b>	<b>93</b>
<b>C</b>	<b>Lists of wafers, samples and measurement equipment</b>	<b>97</b>



# Chapter 1

## Introduction

In the last years, one of the most abundant chemical elements in universe that is present in all known life forms, namely carbon (C) has aroused exorbitant interest all over the world. Carbon atoms bound in a two-dimensional honey-comb lattice built from benzene rings is called graphene and can also be interpreted as a basal plane from graphite or an unrolled carbon nanotube. For a long time strictly two-dimensional crystals have been believed to be thermodynamically unstable, however it is possible to mould two-dimensional crystals on top of a sustaining (flat) three-dimensional substrate coupled simply by van-der Waals forces [1, 2]. Since the seminal experimental realization in 2004 by A. Geim and co-workers [1] and the simultaneously but independently published measurements of the quantum Hall effect from Andre Geim's and Philipp Kim's groups [3, 4], in the only one atom thick graphene sheets attracted much interest from fundamental research in physics and chemistry, over nanotechnology to development of device concepts. Referring to the authors of reference [5] (and references therein) this can be attributed to three main reasons. Firstly, due to peculiarities in the dispersion relation and hence, the linear band structure for low energies, charge carriers in graphene monolayers behave like "massless Dirac fermions" and in bilayers like "massive chiral fermions" [2, 6]. Therefore the electron transport is described by the Dirac equation allowing access to quantum electrodynamics in a simple condensed matter table top experiment without extensive colliders such as the **L**arge **H**adron **C**ollider (LHC) [7]. In this way, a counterintuitive relativistic process, Klein tunnelling of relativistic particles - also know as Klein paradoxon was experimentally observed for the first time in graphene [8, 9]. Quantum electrodynamics and the introduction of a pseudospin due to two sublattices led to the understanding of the half-integer quantum Hall effect [2–4, 10].

Second, graphene is a promising candidate for device application because of its superlative properties, often valid also for bilayer and few-layer graphene [11]. The charge carriers exhibit a giant intrinsic mobility still at room temperatures leading to a mean free path of a few microns making them capable to built spin valve-, superconducting- or ballistic transistors [6] and ultra-high frequency devices [12, 13]. Graphene can sustain high current densi-

ties and shows record thermal conductivity. By the way, graphene is the strongest material, is very stiff and impermeable to gas, transparent and suitable for foods [14]. These eligible properties make them promising for a wide field of application from gas sensors for individual molecules, over transparent electrodes e.g. for solar cells and sandwich-materials to hold longer fresh or makes materials more robust to microelectronics. The development of graphene devices may help to preserve the validity of the well known Moore's law [15] for a longer time or promote "green technologies" where reduction of power consumption, thermoelectric properties [16] and hence also heat transfer plays an important role.

The third reason for the current interest in graphene is the fact that "flat" graphene has intensely been investigated theoretically for more than 60 years [17]. Because graphene is the basic materials e.g. for three-dimensional graphite, one-dimensional carbon nanotubes and zero-dimensional buckyballs, it is not surprising that a lot of the famous properties were predicted long before the experimental realization.

However some findings are still unclear. Since room temperature mobilities up to  $\sim 10^5 \text{ cm}^2/\text{Vs}$  are calculated [18], and even  $\sim 2 \times 10^5 \text{ cm}^2/\text{Vs}$  [19] are expected in a relevant range of carrier concentration from temperature dependent measurements, an experimental confirmation of such high values for the mobilities are still lacking. The consensus exist that a fundamental limit of the mobility in graphene is due to electron-phonon scattering. Despite the origin for the low mobilities observed in numerous experiments is still under debate. It is known that the conductivity in suspended and thermally cleaned graphene can be significantly enhanced [20, 21] and it has been reported that also the use of  $\text{Pb}(\text{Zr}_{0.2}\text{Ti}_{0.8})\text{O}_3$  (PZT) as substrate material increases the mobility of few layer graphene [22]. We had to mention that the commonly used substrate is Si/SiO<sub>2</sub> with a certain thickness of the oxide layer due to the visibility of even monolayer flakes under an optical microscope [23]. The influence of the underlying substrate seems to dominate the mobility of the graphitic sheets. Possible scatterers are (charged/magnetic) impurities [24] and moreover, the interaction between graphene and the substrate determines the frequency of the out-of-plane (flexural) vibrations, both influencing the transport properties at finite temperatures. In addition, electrostatic interaction between a single graphene sheet and a SiO<sub>2</sub> substrate is dominated by polar modes at the SiO<sub>2</sub> surface [25].

The motivation of this thesis was to facilitate investigations of graphene on various substrates and to explore the influence on the transport properties. We decided to use crystalline semiconducting GaAs-based substrates grown by molecular beam epitaxy due to their high tunability. Furthermore, GaAs is the best understood semiconductor for ultrafast electronics, optoelectronics and quantum electronics applications [26]. The combination of these two materials may auxiliary lead to opportunities in device applications and enables the investigations of graphene with surface acoustic waves. Because of the mostly used amorphous SiO<sub>2</sub> substrate material, the latter was not possible far to now. First promising tests of probing graphene with surface acoustic waves have already been enabled and carried out in cooperation with J. Ebbecke from the Mads Clausen Institute, University of Southern Denmark in the framework of this thesis. An optical micrograph of such a sample



**Figure 1.1:** Optical micrograph of a graphene sample, prepared for surface acoustic wave experiments. The graphene on the right is contacted by the lower right two aluminum contacts (bright). The interdigital transducer for the surface wave generation is visible in the left part of the image. These two main components are zoomed in at the corresponding insets.

is depicted in Figure 1.1.

During our work, we became aware from Raman investigations of graphene on GaAs [27] and graphene on GaAs/AlAs heterostructures that is used to tune the visibility of graphene on such a substrate [28]. To best of our knowledge, no transport investigations has been done on graphene or thin graphite lying on top of GaAs or InGaAs.

The thesis is organized in following way. After this short introduction the basic theoretical concepts are given in chapter 2. First the lattice structure, the resulting dispersion relation and peculiarities with respect to the number of layers of a graphene sheet will be introduced. Afterwards the transport properties such as the minimum conductivity and the magnetotransport behavior with the half-integer quantum Hall effect in graphene mono- and bilayer is briefly discussed. This chapter is closed with the basic concepts to some quantum interference phenomena, namely weak localization effects and universal conductance fluctuations.

In chapter 3 the experimental set-ups and technologies used in this thesis are collected. For graphene detection optical and scanning electron microscopes are used, for detecting the morphology atomic force microscope and to observe the optical properties imaging ellipsometry is applied to the graphitic sheets. Magnetotransport measurements are done in dependence of the temperatures down to  $T = 1.7$  K and with magnetic fields up to 10 T. Graphene preparation on different substrates and the especially the graphene detection, localization and the counting of the number of layers is covered in chapter 4. One focus

lies hereby on the challenging detection and classification of graphene on non Si/SiO<sub>2</sub> substrates with a certain thickness of the oxidized layers, where the graphitic flakes are not visible with an optical microscope. We visualize how we were able to overcome this problem by an entanglement of different experimental efforts. In this way also the preparation of field-effect transistor like devices for transport measurements can be done.

In the next chapter, chapter 5, the mechanical and optical properties of graphene will be discussed. These results are a direct benefit from some efforts with the detection. On the one hand the flexibility of graphene was investigated in detail with atomic force microscopy and on the other hand the dispersion relation including refraction and extinction indices could be determined from the imaging ellipsometry data.

Chapter 6 deals with electrical, transport and magnetotransport properties of graphene on mainly GaAs and InGaAs substrates. Fundamental transport measurements in dependence of field effect and temperature have been carried out on graphene on different substrates as well as comprehensive investigations of weak localization signatures at low magnetic fields.

The last chapter 7 briefly recapitulate the contents and achieved results of this work. A comparative discussion and a short outlook closed this thesis.

# Chapter 2

## Background

Carbon is a very common material, often connected to energy processes, such as in the Bethe-Weizsäcker-cycle (also known as CNO cycle) in stars or in photosynthesis of plants. As condensed matter two modifications of carbon are known: diamond and graphite. The hybridization and the resulting crystal structure distinguish between these two materials. The latter, graphite, consist of numerous layers of carbon atoms arranged in a honeycomb lattice that are stacked in an ABA configuration. The binding of the C atoms within a plane are very strong, whereas the coupling from one basal plane to the other is very weak. The crystal structure of one basal plane and only a few stacked planes, called graphene and few layer graphene or thin graphite, will be described in the first part of this chapter. In the following the basic concepts are introduced for understanding the experimentally observed electronic and magnetotransport properties in this two dimensional crystal. Therefore, the band structure and the electronic properties are described depending on the number of layer. Next the dependence on magnetic field will be discussed. Finally, experimentally detected phase coherent transport phenomena are shortly described, namely weak localization and universal conductance fluctuations.

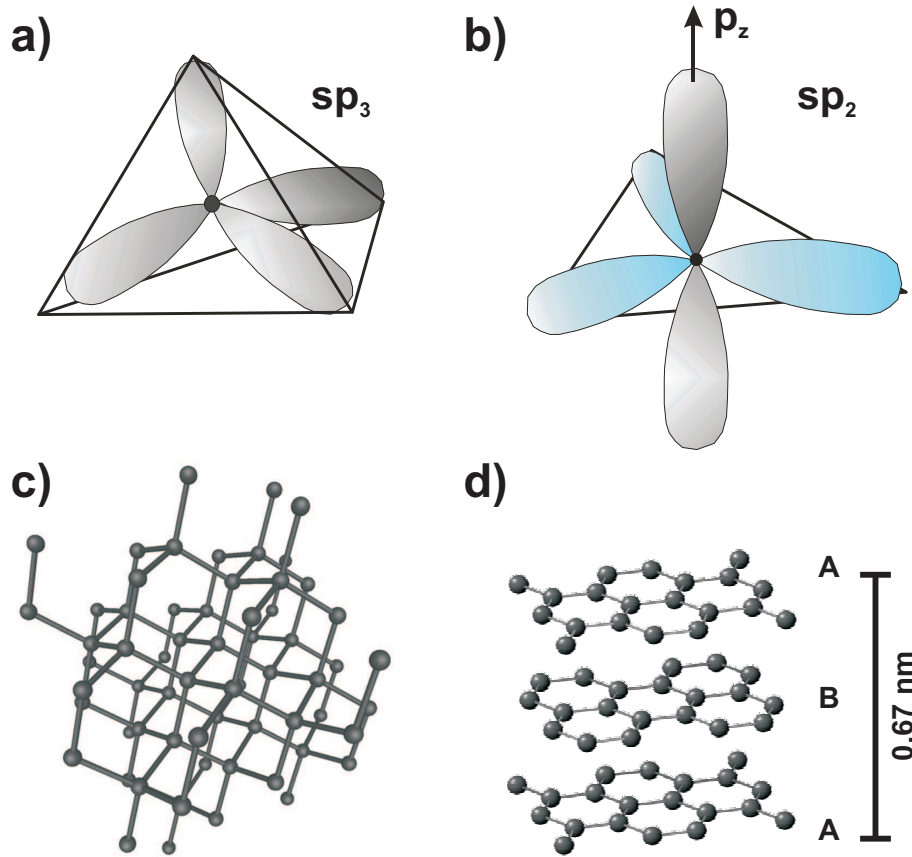
### 2.1 Structural and electronic properties

As already mentioned there are two possible forms of condensed carbon matter - diamond and graphite. They differ in the state of hybridization of the carbon atoms leading to two very different materials. Carbon atoms have the following starting configuration:

$$1s^2 2s^2 2p^2 \quad (2.1)$$

The two  $1s^2$  electrons from the innermost shell do not contribute to the chemical bonding and are no longer taken into account.

To assemble molecules or solids from carbon atoms, bonds in between are needed. This

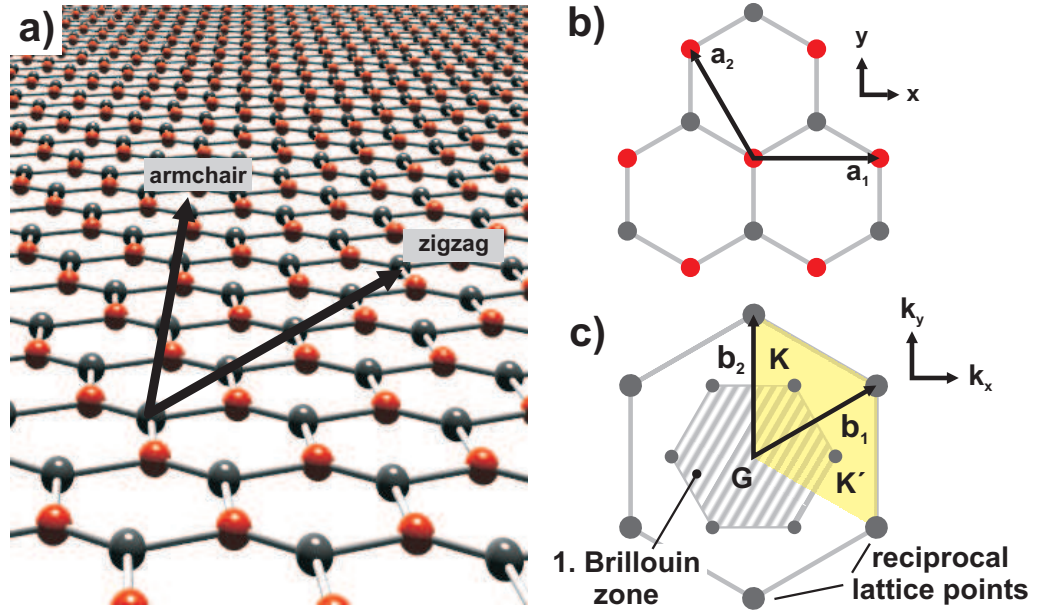


**Figure 2.1:** Comparison between a)  $sp^3$  and b)  $sp^2$  hybridization (taken from reference [29]) and the resulting crystal structure c) diamond and d) graphite [30].

can be achieved in different ways<sup>1</sup>. The two most interesting options to build a solid are the so called  $sp^2$ - and  $sp^3$  hybridization. Therefore one or two electrons of the  $2p$ -level combine with one of the  $2s$  electrons to three or four hybridized orbitals for  $sp^2$  and  $sp^3$  hybridization, respectively. The  $sp^3$  hybridization leads to tetrahedral bonds, originating the rigidity of diamond for instance.

Graphite is based on  $sp^2$  hybridized bonds. The  $sp^2$ -orbitals define three  $\sigma$ -bonds within a plane with an angle of  $120^\circ$ . A schema of the hybridization is drawn in Figure 2.1 a) for the  $sp^3$  and in b) for the  $sp^2$  hybridization. The resulting crystals are shown in c) for the diamond and d) for the graphite lattice structure with ABA stacking. The distance between two planes in graphite is 0.335 nm. A basal-plane of the graphite lattice is called graphene. From the  $120^\circ$  angle of the bonds in such an  $sp^2$  arrangement a hexagonal lattice follows. The lattice of a graphene plane and some fundamental crystal properties are depicted in Figure 2.2. The two main directions in the two-dimensional lattice are called zigzag and

<sup>1</sup>Probably one reason why carbon is very often present in nature and carbon research is such manifold.



**Figure 2.2:** a) Perspective view of a hexagonal lattice. Armchair and zigzag direction are denoted by arrows. A hexagonal lattice with equal atoms can be reduced to two sublattices shown by black and grey spheres. b) The construction of the lattice in real space with the lattice vectors  $\vec{a}_1$  and  $\vec{a}_2$ . c) The reciprocal lattice which is again based on hexagons with the corresponding lattice vectors. The hatched hexagon is the first Brillouin zone. The yellow parallelogram shows a unit cell with the two inequivalent points K and K'

armchair and are marked with arrows in Figure 2.2 a). The hexagonal lattice in real space is shown in Figure 2.2 b). In the selected representation the base vectors are  $\vec{a}_1 = a \cdot (1, 0)$  and  $\vec{a}_2 = a \cdot (-1/2, \sqrt{3}/2)$  with  $a = \sqrt{3}a_0$  and  $a_0 = 1,42\text{\AA}$  the distance between two neighboring carbon atoms. In Figure 2.2 c) the corresponding reciprocal lattice with the first Brillouin zone (hatched hexagon), the reciprocal unit cell (yellow) and the reciprocal base vectors are given. Some distinct points at the zone boundary K and K' are labeled. The graphene layers in graphite are only weakly coupled with the unchanged  $p_z$  orbital also shown in Figure 2.1 b). This remaining valence electron gives rise to the  $\pi$  bond which will provide delocalized electrons in the plane forming a bonding  $\pi$  and an antibonding  $\pi^*$  band.

Because the hexagonal lattice is built only by carbon atoms, in real space as well as in k-space the crystal lattices can be described by two inequivalent triangular sublattices. As a consequence, two in real space neighboring carbon atoms occupy non-equivalent sites as demonstrated in Figure 2.2 with red and grey atoms. The band structure of the for electric properties relevant  $\pi$  bands can analytically be calculated with a tight-binding approach using a separate Bloch function ansatz for the two inequivalent lattice sites. Carefully computing this ansatz as described in details for instance in reference [31] leads

to following dispersion relation:

$$E(k_x, k_y) = \pm \gamma_0 \sqrt{1 + 4 \cos\left(\frac{\sqrt{3} a k_x}{2}\right) \cos\left(\frac{a k_y}{2}\right) + 4 \cos^2\left(\frac{a k_y}{2}\right)} \quad (2.2)$$

with  $a = \sqrt{3}a_0 = 0.256$  nm and  $\gamma_0 \approx 2.8$  eV the nearest neighbor hopping energy. The "+" and "-" sign in equation (2.2) the signs for the occurrence of electrons and holes as charge carriers, respectively. Another mentionable fact is also found in equation (2.2): For some particular values of  $\vec{k}$  the whole root cancels out and the energy of electrons and holes becomes zero. Together with the  $\pm$  sign this already shows the semi-metal character of graphene. Accordingly, conduction and valence band, generated by the binding  $\pi$  and the antibinding  $\pi^*$  bands, respectively, touch each other exactly at all inequivalent K and K' points. Moreover, the bands are parabolic at the Gamma point in the middle of the zone center and a band gap opens at the M point which is in the middle of the Brillouin zone edge.

The dispersion relation  $E(\vec{k})$  for a full hexagon in k-space is plotted in Figure 2.3 a). The situation for low energies in the first Brillouin zone terminated by K and K' is enlarged in Figure 2.3 b). In the intrinsic (undoped) case, the valence band is fully occupied and the conduction band is empty. This causes the Fermi energy  $E_F$  to intersect the bands exact at K and K'. Hence, in case of neutrality, states exist at  $E_F$ , which are half hole-like and half electron-like. This is why the K and K' points are labeled as charge-neutrality points. However, these points are also referred to as Dirac-points. For low energies only a linear term of equation (2.2) survives:

$$E(|\vec{k}|) \approx \sqrt{3}\pi\gamma_1 a |\vec{k}| \quad (2.3)$$

In comparison to most of the commonly considered semiconductors/semi-metals, the band structure in the for electronic properties interesting low energy region is linear. Thus the charge carriers behave like relativistic Dirac fermions and hence, the description for low energies is similar to a photonic dispersion relation:

$$E(p) = c^* \cdot p \quad (2.4)$$

with an effective speed of light of  $c^* \approx 10^6$  m/s. The speed of light is translated into a solid state physics term with the Fermi velocity  $v_F$ . One consequence is that the effective mass of the charge carriers in graphene is equal to zero  $m^* = 0$  [3, 14, 32]. The gray background in Figure 2.3 b) indicates the first Brillouin zone in reciprocal space. Since the boundaries of the Brillouin zone and the Dirac points coincide it is obvious that only one complete double cone must be considered, since all other points in reciprocal space can be reached by a reciprocal lattice vector.



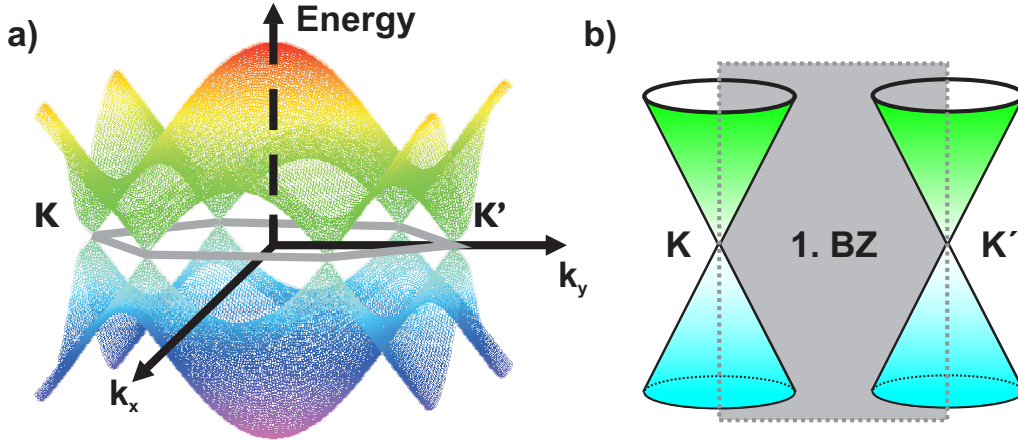
Resulting from the two sublattices and as a direct consequence a further quantum number, the so called pseudo-spin is introduced accounting the valley-degeneracy [2, 32]. A good quantum number for this description is the chirality, the projection of the pseudo-spin onto the wave vector  $\vec{k}$ . Normally chirality is conserved. The fact that there is an additional degeneracy (described by the pseudo-spin) automatically leads to a four-fold degeneracy in the description of graphene: each charge carrier can be spin up/down and at valley K or K'. This effects among others the quantum Hall effect as will be described later. The properties of the pseudo-spin can be described by a so called spinor like structure as known from relativistic quantum mechanics. Together with the linear dispersion relation it can be shown that a charge carrier in graphene must be described rather by relativistic Dirac equation than by Schrödinger equation and hence they are often named Dirac fermions [2–4, 10, 32].

This extraordinary band structure of graphene attracted theorist long before graphene was experimentally realized [17, 33, 34]. However, since the experimental observation of the four-fold degeneracy by quantum Hall measurements it was realized that graphene offers the access to quantum electrodynamic phenomena in a solid state environment.

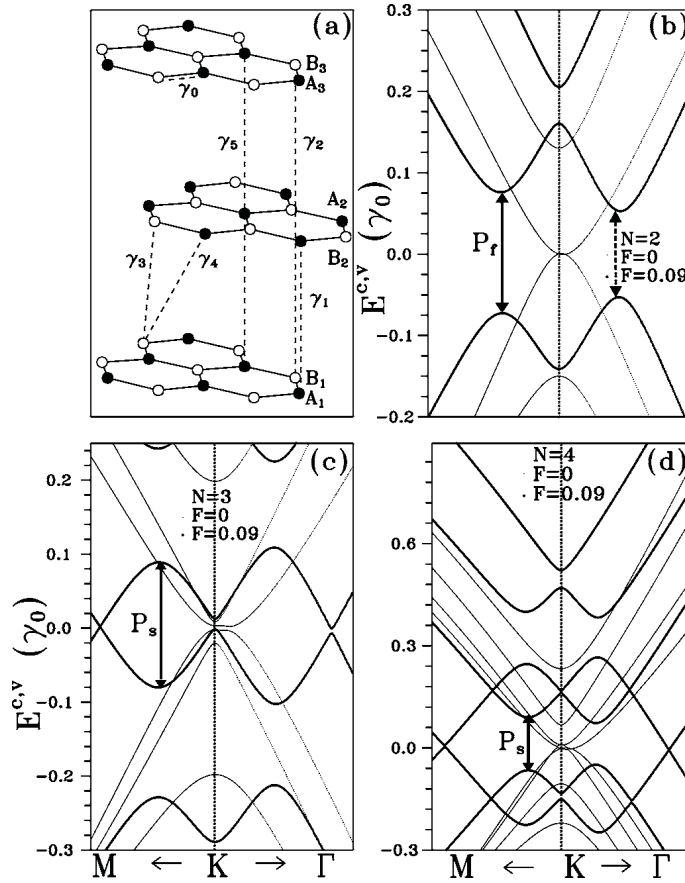
### From graphene to graphite

Graphene is the base of graphite, which is constructed from many A-B stacked graphene layers. The interlayer coupling is transferred mainly by van-der Waals forces and hence weak as already mentioned above. The band structure, however, is very sensitive to the number of layers. By adding one additional layer a so-called bilayer graphene system is created. One layer more leads to trilayer graphene and the next one to four-layer graphene and so on, ending up with three-dimensional graphite, where some layers more or less do not change the properties any more. By adding up layers, the unit cell changes each time and consequently the electronic properties, too. The threedimensional properties of graphite are more and more recovered. In the ideal case the layers have an ABA stacking, also known as Bernal stacking (compare Figure 2.1 d) and Figure 2.4 (a)). The properties of more than ten layers should be quite similar to those of graphite [2]. The situation for graphene consisting of one, two, three or four layers will briefly reviewed, following reference [35]. Related drawings are reproduced in Figure 2.4.

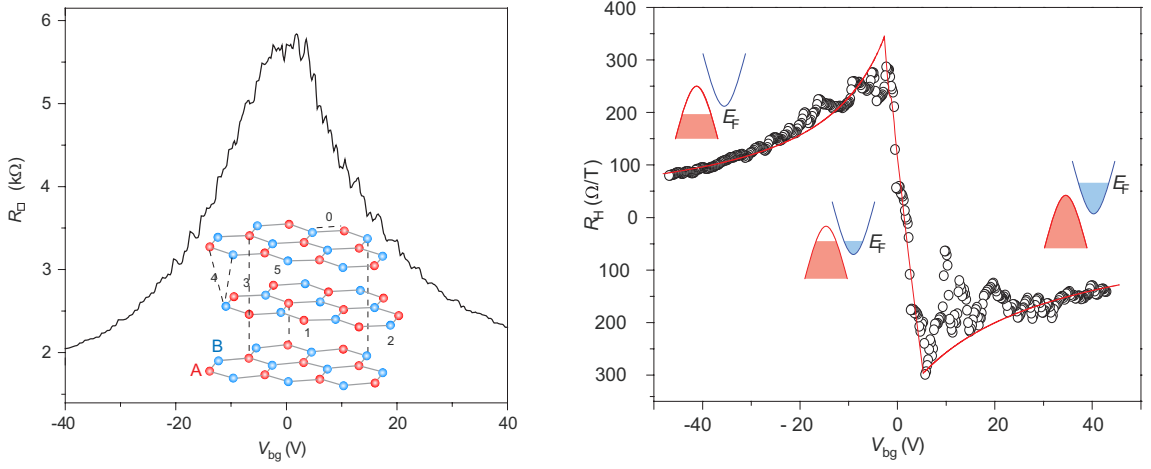
Starting with a bilayer system the unit cell is already a three dimensional one counting four atoms, two for each layer. Besides a band splitting of two parabolic bands, a parabolic dispersion relation for valence and conduction band is recovered at low energies. Again, valence and conduction bands touch each other at K and K', for bilayers without asymmetries between or in the layers. This situation is depicted in Figure 2.4 (b) without electric field (thin lines). Consequently, undoped bilayer graphene has also no bandgap and hence behaves like a semi-metal. In the case of trilayer graphene the situation gets more complicated. Theoretically, a band gap opens, that would make trilayer graphene a semi-



**Figure 2.3:** Dispersion relation of graphene. In b) the important low energy region is drawn. Two double cones result at the K and K' points. Shaded in grey denotes a part of the first Brillouin zone.



**Figure 2.4:** a) The geometric structure of the trilayer graphene.  $\gamma_0$  is the intralayer interaction and  $\gamma_i$ 's indicate the interlayer interactions. The light (heavy) curves in (b), (c), and (d), respectively, exhibit the energy dispersions of the bilayer (N=2), trilayer (N=3), and four-layer (N=4) graphene in the absence (presence) of electric field ( $F$ ) in units of  $\gamma_0/(e\text{\AA})$ , taken from reference [35]. The x axes describe directions from one Dirac point K to points of high symmetry ( $\Gamma$  and  $M$ ) and have different lengths.



**Figure 2.5:** Reprints of the transport properties of a trilayer graphene taken from reference [36]. In a) the gate dependent sheet resistance is plotted and in b) the corresponding Hall resistance for a fixed perpendicular magnetic field of  $B=9$  T is shown. The three insets schematically depict the position of the Fermi energy ( $E_F$ ) at different values of  $V_{bg}$ , from [36]

conductor [35] but experimental investigations point to the semi-metallic like behavior with overlapping conduction and valence bands [36]. The next layer would theoretically recover a semi-metal behavior for four-layer graphene. But the classification between a semi-metal or semiconductor with a small band gap seems to be a difficult task for theorists due to various contributing parameters [35, 37–40] and hence should not be discussed in more detail here. In experimental reality, trilayer graphene behaves, similar to graphite, like a semi-metal with overlapping parabolic valence and conduction band at K and K' points as measured by M. F. Craciun *et al.* [36] and shown in Figure 2.5. This band overlap is reported to be tunable by field-effect [36]. Two relevant graphs of this reference are reprinted in Figure 2.5. In Figure 2.5 a) the sheet resistance  $R_{\square}$  of a trilayer graphene in dependence of the applied backgate voltage and in Figure 2.5 b) the corresponding Hall resistance at  $B = 9$  T are shown. Both measurements were done at low temperatures [36]. The sheet resistance as a function of the backgate voltage shows a distinct peak. Its position is equal to a characteristic sign reversal in the Hall resistance. The maximum in the sheet resistance (compare Figure 2.5 a)) is attributed to the existence of a charge neutrality point (CNP) where the electron density in the system is equal to the hole density and the Fermi energy  $E_F$  lies at  $E = 0$ . Especially from Hall resistance data in Figure 2.5 b) it follows that trilayer graphene is a semi-metal with overlapping conduction and valence band as depicted in the inserted schemas of Figure 2.5 b). A maximum in the sheet resistance, or equivalently a minimum in the conductivity as a function of the gate voltage is also observable in mono- and bilayer graphene that appears at  $E_F = 0$ , where valence and conduction bands touch. For intrinsic (undoped) mono- and bilayer graphene exist, contrary to the findings in trilayer graphene, only holes for  $E_F < 0$  and electrons for  $E_F > 0$ , meaning that there is no band

overlap.

Finally it should be noticed that the description of graphite (so adding up many more layers) is already quite old and a lot of work bases on the Slonczewski-Weiss-McClure model which describes the coupling between layers with hopping terms between  $\pi$  orbitals in different layers [17, 32–34]. The multi-layered structure of graphite makes it a highly anisotropic crystal and explains its softness and lubricant properties<sup>2</sup>.

Regrettably, the number of layers can often only be determined with a uncertainty of one or two layers in this thesis. In such a case this sample will be referred as "graphene", meaning the whole range from monolayer to **Few-Layer Graphene** (FLG), but much thinner than graphite. This seems reasonable, because especially the transport in the classical regime is quite similar for single to few-layer graphene.

## 2.2 Transport properties

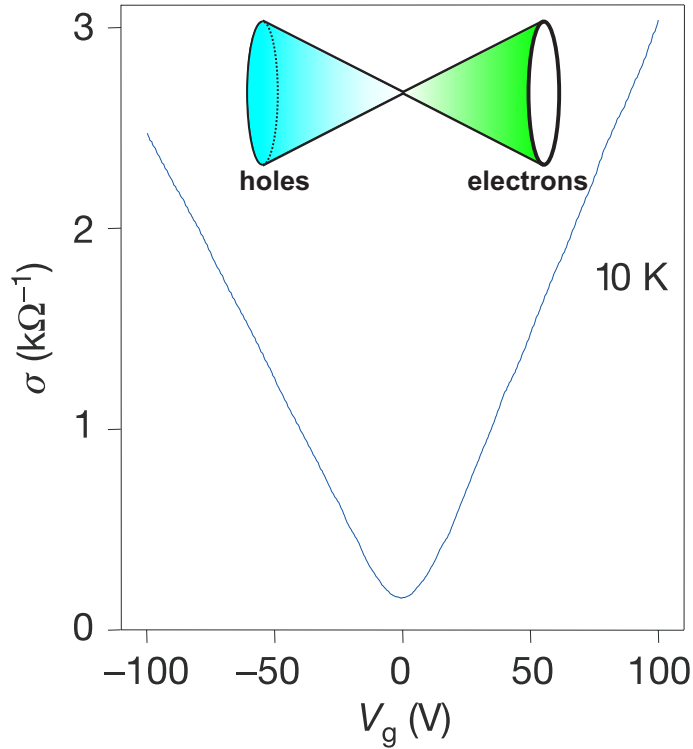
The previous discussed band structure is responsible for different phenomena occurring in electrical measurements in graphene. These are the minimum conductivity, classical and quantum Hall effect and phase coherent phenomena, namely weak localization and universal conductance fluctuations. These are introduced in the next paragraphs.

### 2.2.1 Minimum Conductivity

As already stated and shown for the case of trilayer graphene (Figure 2.5) one property of graphene and few-layer graphene is their missing band gap. The type of charge carriers is determine by the position of the Fermi energy  $E_F$ . Its position can be changed by an electric field that can be generated by applying a positive or negative gate voltage. A direct consequence is the strong dependence of the conductivity of the position of  $E_F$  and hence from the gate voltage. The minimum conductivity appearing for  $E_F = 0$  and hence lying exactly between valence and conduction band was one of the first reported experimental finding of graphene [1, 3, 4]. A typical measurement of this phenomenon (taken from reference [3]) is reprinted in Figure 2.6. The inserted double cone of the low energy part of the dispersion relation helps explaining the slope of these experimental findings. By sweeping the gate voltage  $V_g$  from -100 V to +100 V the Fermi level is shifted on the double cone from the valence band on the left to the point where valence and conduction band touches in the middle, to the conduction band on the right. This affects both, charge carrier density and simultaneously the conductivity. First, the hole density is linearly reduced down to the Dirac point, where the conductivity minimum is reached. Then the type of the charge

---

<sup>2</sup>Probably nearly everybody uses this probabilities in everyday life by writing with a pencil.

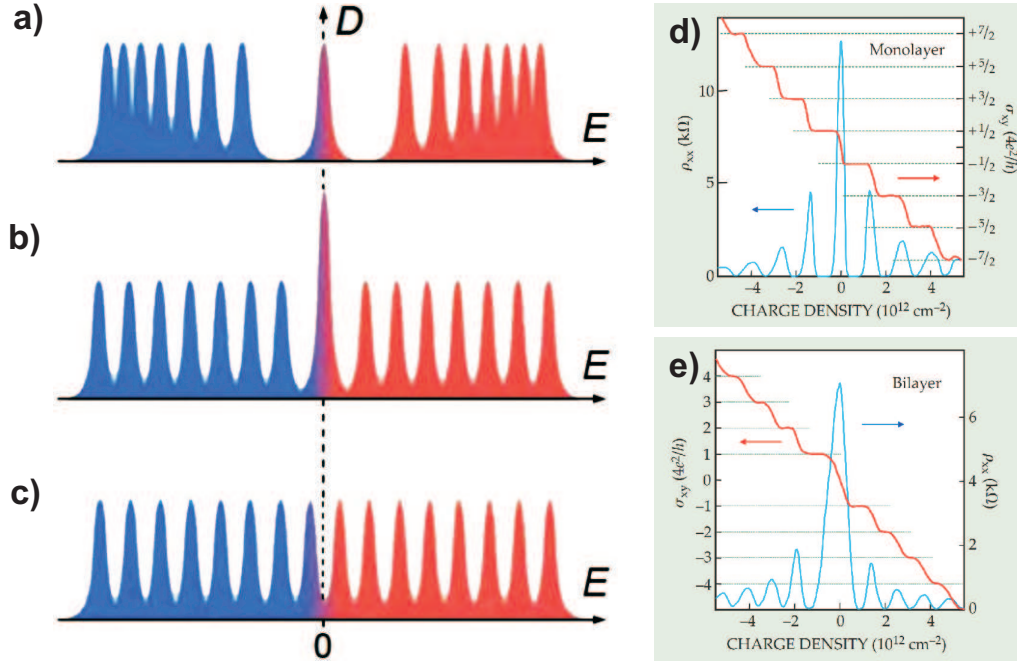


**Figure 2.6:** Gate dependent conductivity of a graphene monolayer, adapted from [3]. The conductivity does not vanish at the Dirac point. The inset shows one double cone of the dispersion relation.

carriers changes, as proven by Hall measurements. Further increasing the applied gate-voltage increases the electron density and thus the conductivity increases again linearly. At the Dirac point, also referred to as charge neutrality point, the conductivity reaches a minimal however finite value. But - as it was quickly realized - the conductivity never falls below a certain value. Regarding the band structure one would conclude that at the crossing points of the bands the number of carriers tends to zero and thus the conductivity should also vanish. But in contrast, a minimum conductivity in the range of  $\sigma_{min} = 4e^2/h$  is found experimentally in many samples [1–3]. Theoretically a value of  $\sigma_{min} = 4e^2/h\pi$  is predicted [41, 42], but the detailed origin of this phenomenon is still unclear and under debate [2].

### 2.2.2 Quantum Hall effect

The unconventional **quantum Hall effect** (QHE) found in graphene [3, 4] was one of the driving forces in the early days of experimental graphene research and pushing investigations on the whole material system a lot. The QHE was one of the most significant



**Figure 2.7:** The sequence a)-c) describes the energy dependent density of states  $D(E)$  at a finite magnetic field perpendicular to the plane of the charge carriers a) for massless Dirac fermions in single layer graphene, b) for massive Dirac fermions in bilayer graphene and c) for Schrödinger electrons with two parabolic bands touching each other at zero energy [2]. d) and e) Resistivity (red) and Hall conductivity (blue) as a function of charge carrier density at finite magnetic field [10]. The measurement of the quantum Hall effect in d) corresponds to a monolayer [3] and shows the half-integer quantum Hall effect. The quantum Hall effect in e) reflects the quantum Hall effect in bilayer graphene, the missing plateau at zero carrier density is clearly visible [43].

discoveries [44] of the 1980s and is an effect that has so far only been observable in high quality semiconducting two dimensional charge carrier systems. Before going into the details of the outstanding effects in graphene, QHE in conventional systems with a parabolic dispersion relation will shortly be revisited after a few words about the concept behind the classical Hall effect.

### From classical Hall effect to (half-)integer quantum Hall effect

The classical Hall effect can be observed by measuring a conductor's resistance perpendicular to the current, if a magnetic field is applied again orthogonal to current and voltage probes. The electric field induced by the voltage compensates the Lorentz force (produced by the magnetic field affecting the charge carrier). Thus the resulting voltage is proportional to the magnetic field:  $|U_{xy}| = I \cdot B / (|dne|)$  with  $I$  the flowing current,  $B$  the absolute value of the magnetic field,  $d$  the width of the conductor,  $n$  the charge carrier density and  $e$  the

electron charge. By normalizing this voltage-drop by the current  $I$  the following expression for the Hall resistance  $R_{xy}$  is deduced.

$$R_{xy} = \frac{B}{|dne|} \quad (2.5)$$

The Hall resistance is proportional to the magnetic field  $B$  and can be used to determine the charge carrier density  $n$  if the sample thickness  $d$  of the three dimensional sample is known. For two-dimensional charge carrier systems the Hall resistance  $R_{xy}$  is directly proportional to  $B$  and indirect to  $e$  and  $n$ .

But what happens if the same measurement is carried out with a high mobile two-dimensional charge carrier system at low temperatures and a high magnetic field? As demonstrated by K. v. Klitzing *et al.* in 1980 [44], under such conditions the Hall resistance gets quantized and exhibits constant values over a certain magnetic field range, what is referred to as quantum Hall plateaus. The resistance at the plateau takes the following values

$$R_{xy} = \frac{1}{\nu} \frac{h}{e^2} = \frac{1}{\nu} \cdot 25812.8 \, \Omega \quad (2.6)$$

with  $\nu$  being an integer. In the presence of a finite perpendicular magnetic field the density of states of a real two dimensional charge carrier system (only the lowest subband occupied) condenses into equidistant highly degenerated delta shaped peaks, the so-called Landau levels (LL). These peaks are broadened by disorder. The integer  $\nu$  is the so called filling factor. For a non spin-degenerated system it is defined as:

$$\nu = \frac{nh}{eB} \quad (2.7)$$

The energy of such a LL in a conventional semiconductor is  $E_{N_{LL}} = \hbar\omega_C(N_{LL} + \frac{1}{2})$  with  $\omega_C = eB/m^*$  the cyclotron frequency and  $\hbar$  the Planck constant  $h$  over  $2\pi$  and the effective mass  $m^*$ . The equidistant spacing of the LL level can be seen from this relationship. A schema of the LL of a conventional two dimensional system is depicted in Figure 2.7 c), a series of broadened peaks of the distance of  $\hbar\omega_C$ . That is also the situation expected and already experimentally verified for FLG [45].

In the case of massless Dirac fermions as present in graphene monolayers the spectrum of the Landau levels takes a different form:

$$E_{N_{LL}} = \pm v_F \sqrt{2eB\hbar(N_{LL} + \frac{1}{2} \pm \frac{1}{2})} \quad (2.8)$$

In this equation  $v_F$  is the Fermi velocity that is approximately  $1/300$  of the speed of light ( $v_F \approx c/300$ ),  $\hbar$  is again the reduced Planck constant and  $N_{LL}$  refers to the Landau level

index. This sequence of Landau levels is drawn in Figure 2.7 a). The " $1/2$ " term in equation (2.8) considers the spin and the " $\pm 1/2$ " term the pseudospin, which is originated by the double valley degeneracy of the bandstructure as defined before. The " $\pm 1/2$ " term gives rise to the unconventional so called half-integer QHE and a very big difference in the LL spectra compared to conventional QHE systems. For massless Dirac fermions there exists a zero energy state at the 0th LL, meaning that this lowest LL is occupied by both holes and electrons. For conventional parabolic systems with Schrödinger-like fermions this lowest energy level is shifted by  $1/2 \hbar \omega_C$ . Additionally, the  $\pm 1/2$  in equation (2.8) shifts the whole QHE spectrum by  $1/2$  in comparison to conventional systems. Therefore, this QHE is denoted as half-integer QHE in contrast to the integer QHE in conventional parabolic system. However, the half-integer QHE must not be mixed up with the fractional quantum Hall effect, which can be described in the picture of composite fermions [46].

There is another noticeable property in equation (2.8). The distance between two Landau level peaks depends on the square-root of the energy. Together with high mobility and Fermi velocity this dependence (especially the big energetic distance between  $N_{LL} = 0$  and  $N_{LL} = \pm 1$ ) allows to measure QHE at room temperature for the first time [47]. With respect to spin and pseudospin the degeneracy in the LL spectrum is  $f = 4$ . This four-fold degeneracy of graphene was already mentioned in the discussion of the band structure. To sum up, the position of the quantum Hall plateaus are described in graphene monolayers by modifying equation (2.6):

$$R_{xy} = \frac{1}{v} \frac{h}{e^2} = \pm \frac{1}{4 \cdot (N_{LL} + 1/2)} \frac{h}{e^2} \quad (2.9)$$

In the case of massive Dirac fermions that are found in bilayer graphene another unusual QHE occurs. The Landau quantization is shown in Figure 2.7 b) and is described by

$$E_{N_{LL}} = \pm \hbar \omega_C \sqrt{N_{LL} \cdot (N_{LL} - 1)} \quad (2.10)$$

Evidently two possible solutions exist for a zero-energy state,  $N_{LL} = 0$  and  $N_{LL} = 1$ . Apart from a missing plateau for zero energy originated by this additional degeneracy, the Landau level peaks are now equally spaced again and therefore a conventional sequence of quantum Hall plateaus is observed.

$$R_{xy} = \frac{1}{v} \frac{h}{e^2} = \pm \frac{1}{4 \cdot N_{LL}} \frac{h}{e^2} \quad (2.11)$$

The experimental findings for both monolayer and bilayer confirm this results. The half-integer steps of  $4e^2/h$  for a graphene monolayer are shown in Figure 2.7 d) in blue and in the corresponding longitudinal resistance exhibiting SdH oscillations are clear fingerprints of massless Dirac fermions in graphene. In Figure 2.7 e) the same measurement for a bilayer graphene is given. There is really no plateau at zero energy and since the number



of states in that situation is twice compared to higher levels, the step in the Hall resistance at the (missing) 0th LL must be twice, too. The amplitude of the SdH for this LL is also much higher and much more pronounced than those for higher LLs.

### 2.2.3 Interference phenomena

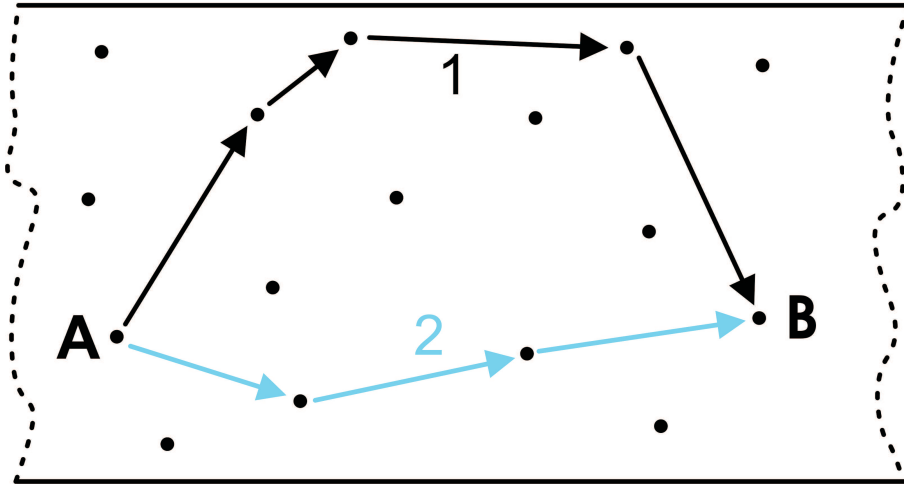
For simplicity the following is described for electrons even if the argumentation for holes is analog. Before the wave character of electrons and its consequences for charge transport is addressed, the classical picture of transport in matter (e.g. a metal) is shortly revisited. The so called Drude model describes charge transport in matter by a classical approach. The electrons are viewed as particles that are accelerated by an applied electric potential. Scattering on heavier and relative immobile positive ions localized in the crystal, the acceleration of the charge carriers is stopped and the movement of the electrons is slowed down. With reaching an equilibrium between acceleration and slowing a stationary current density  $j = -en_e v_D = \frac{e^2 \tau n_e}{m} E$  arises (with  $n_e$ : electron density,  $v_D$  drift velocity and  $\tau$  mean free time between ionic collisions). From this current density the term for the conductance can be deduced:

$$\sigma = \frac{j}{E} = \frac{e^2 \tau n}{m} \quad (2.12)$$

This description holds as long as the electron's wave character can be neglected. If the dimensions of the systems get smaller and the temperature is lowered, quantum mechanical interference effects influence the transport and must be taken into account for the description of the transport. Two effects are briefly considered in this thesis, namely weak localization (WL) and universal conductance fluctuations (UCFs). More comprehensive discussions of these effects can be found in literature [48–51].

Systems in which the quantum mechanical character of charge carriers becomes visible are called mesoscopic system. Their lengths scales are in the order of the phase coherence length  $L_\phi$ . This length is a very important quantity and refers to the mean free path a charge carrier can travel phase coherently. In other words, the mean free path is the length scale, where the phase information of a charge carrier is stored. Due to the diffusive motion of charge carriers, the phase coherence length is connected to the diffusion constant  $D$  and the coherence time  $\tau_\phi$  by  $L_\phi = \sqrt{D \cdot \tau_\phi}$ . The situation in mesoscopic systems, where phase coherence transport must be considered is sketched in Figure 2.8. Starting at point A and ending at point B two different possible path are drawn. The black points demonstrate scatterers. For a quantum mechanical description of the transmission probability from A to B all partial waves of the charge carriers with their complex amplitudes  $A_i$  must be considered, since all interfere at point B. The total transmission probability is given by:

$$T = |A_1 + A_2|^2 = |A_1|^2 + |A_2|^2 + 2|A_1||A_2|\cos(\varphi_1 - \varphi_2) \quad (2.13)$$



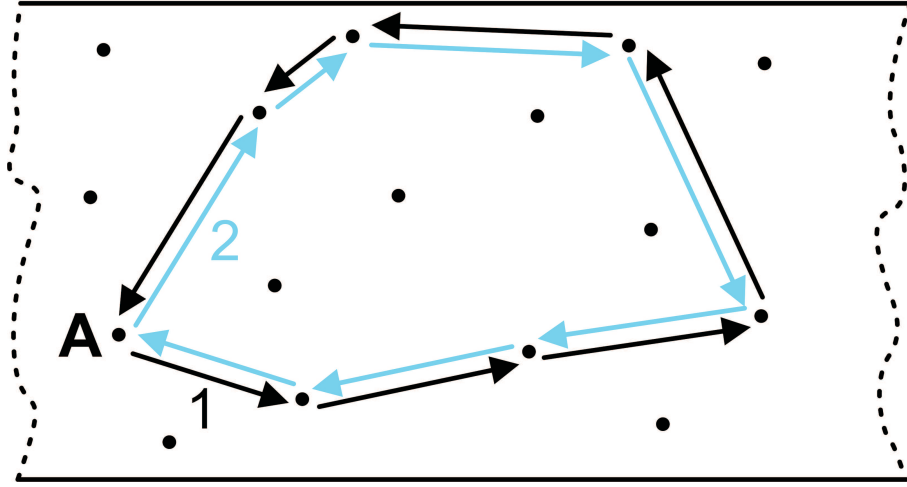
**Figure 2.8:** The way from A to B can be traveled on different ways (e.g. 1 and 2). The partial waves of all possible way starting at A interfere at P, from [50].

with  $\varphi$  the phase of each partial wave. The classical limit is reached if the phase information or phase coherence is destroyed by scattering (e.g. by inelastic scattering). Then the third term representing phase-interference in the partial waves in equation (2.13) vanishes.

### Weak localization

A special case of trajectories is given in Figure 2.9. The paths of two partial waves are chosen in such a way that both describe a more or less regular loop (the exact shape is irrelevant) in opposite direction. Both partial waves interfere constructively at the initial point, if time reversal symmetry excludes phase differences between these two partial waves. The probability for such wave pairs for constructive interference is equivalent with backscattering, which is doubled compared to the classical description, since  $A_1 \equiv A_2$  and  $\cos(\varphi - \varphi) = \cos(0) = 1$  [50]. The electron is localized within this path and can not contribute to the current resulting in an increase of the resistance. The description is valid in absence of an internal or external magnetic field and the effect is called weak localization (WL).

However, an applied magnetic field breaks the time reversal symmetry. This can be visualized regarding the enclosed area. In the case of an applied external magnetic field, a magnetic flux is defined by this area. Since the waves on these paths travel in opposite directions, this flux adds phases with opposite sign to the wave functions, which is known as Aharonov-Bohm effect. Thus the interference term in equation (2.13) does not give one any more. So backscattering is reduced, the electron begins to delocalize and contributes to the conduction. Therefore the resistance shrinks by applying a magnetic field. The enclosed areas are not equal since the points of scattering are randomly distributed in the



**Figure 2.9:** Two partial waves propagating on the same path in opposite direction. The constructive interference at the initial point A leads to a (weak) localization and hence the conductance of the sample is reduced, taken from reference [50].

sample. As a consequence by increasing the magnetic field the weak localization gets damped and finally vanishes.

Weak localization as a quantum correction to conductivity of two-dimensional system has been studied for more than 20 years [49, 52]. It has already been shown [53, 54] that WL measurements in graphene cannot only provide information about the dephasing but also on elastic scattering mechanisms [55, 56]. Elastic scattering can take place within a single valley (intra-valley) and between valleys (inter-valley). So the pseudo-spin has also to be considered since it controls the phase of the wavefunction. Intra-valley scattering cancels the conservation of chirality and thus suppresses WL. Such scattering can occur on lattice defects or dislocations and due to the so-called trigonal warping [55]. In contrast, inter-valley scattering restores WL. The WL correction to the Drude conductivity of a graphene monolayer is given by [55, 57]:

$$\delta\sigma(B) = \frac{e^2}{\pi h} \left\{ F\left(\frac{\tau_B^{-1}}{\tau_\phi^{-1}}\right) - F\left(\frac{\tau_B^{-1}}{\tau_\phi^{-1} + 2\tau_i^{-1}}\right) - 2F\left(\frac{\tau_B^{-1}}{\tau_\phi^{-1} + \tau_i^{-1} + \tau_*^{-1}}\right) \right\} \quad (2.14)$$

where  $F(x) = \ln(x) + \Psi\left(\frac{1}{2} + \frac{1}{x}\right)$ ,  $\Psi$  is the Digamma function and  $\tau_B^{-1} = 4eDB/\hbar$  with  $D$  as diffusion constant. Further is  $\tau_\phi$  the dephasing time. Inter-valley scattering is characterized by  $\tau_i$ , whereas intra-valley scattering is described by  $\tau_*$ . In the latter scattering on defects, which break chirality, as well as on dislocations and ripples, which destroy the interference by their effective random magnetic field, are combined. The corresponding lengths scales are given by  $L_{\phi,i,*} = \sqrt{D \cdot \tau_{\phi,i,*}}$ , with  $D$  again the diffusion constant.

In bilayer graphene the WL correction must be modified and can be described by [54, 56]:

$$\delta\sigma(B) = \frac{e^2}{\pi h} \left\{ F\left(\frac{\tau_B^{-1}}{\tau_\phi^{-1}}\right) - F\left(\frac{\tau_B^{-1}}{\tau_\phi^{-1} + 2\tau_i^{-1}}\right) + 2F\left(\frac{\tau_B^{-1}}{\tau_\phi^{-1} + \tau_i^{-1} + \tau_*^{-1}}\right) \right\} \quad (2.15)$$

The difference between equation (2.14) describing a monolayer and equation (2.15) for the bilayer case is the changed sign in the third term. It is also remarkable that for  $\tau_i^{-1}, \tau_*^{-1} \rightarrow \infty$  meaning that the corresponding scattering mechanism are not present any more, both equation are transformed into the conventional expression for WL in a two dimensional system with two valleys as it is valid for FLG for equal or more than three layers.

### Universal conductance fluctuations

The positions of scattering centers are more or less randomly distributed in a real conductor. As depicted in Figure 2.8 the phase differences at a final point depend strongly on the exact paths a charge-carrier takes. In the same manner the transmission probability is dependent on these individual paths. Therefore the conductivity of a mesoscopic sample, for which the size is on the order of the phase coherence length, depends on the exact configuration of the scattering centers and consequently is specific for each individual sample.

As already explained, the phase differences get changed by an applied magnetic field. This generates aperiodic, reproducible fluctuations in the magnetconductance of a sample. The fluctuations base on the configuration of the scattering centers and hence these fluctuations are often referred to as "magnetic fingerprint" of a sample.

For a phase coherent conductor the amplitude of these conductance fluctuations is independent of the absolute conductance value and can be expressed with the following relation:

$$\delta G = \sqrt{\langle (G - \langle G \rangle)^2 \rangle} \approx \frac{e^2}{h} \quad (2.16)$$

From this independence of the absolute value the fluctuations are universal and therefore called **Universal Conductance Fluctuation (UCF)**. For a real conductor equation (2.16) is only slightly modified since the result  $e^2/h$  is multiplied with a value with magnitude  $\approx 1$ .

# Chapter 3

## Experimental methods

The basic requirement for investigations of graphene on other substrates than SiO<sub>2</sub> with a certain oxide thickness is to overcome the problem with minor visibility of the graphitic layers in an optical microscope on such substrates. Therefore we utilize a combination of several microscopy techniques.

Within this chapter, all used experimental methods including microscopy techniques for detection of graphene, imaging ellipsometry to investigate the optical properties and the set-up for electrical characterization and magnetotransport measurements at low temperatures will be introduced and described.

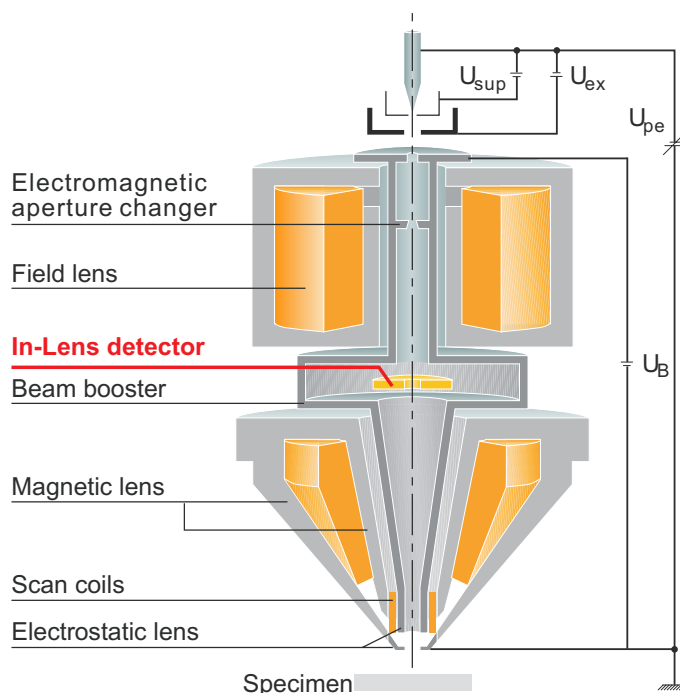
### 3.1 Scanning electron microscope

For detection and determination of the lateral dimensions of graphitic layers on semiconducting substrates a Scanning Electron Microscopy (SEM) was preferred albeit height and number of layer of the flakes was not observable. The used LEO 1530 SEM is equipped with a GEMINI column that is schematically depicted in Figure 3.1.

To get an image from the sample, an electron beam is focused to the region under investigation of the specimen. Therefore, the electrons in the available SEM are released from a field emitting crystal and accelerated into the column containing magnetic and electrostatic lenses. The electrons always pass this system with the maximum possible energy of the SEM, in our case  $E_i = 30$  keV. Shortly before the electrons hit the specimen they are decelerated to the desired primary energy.

After interaction with the specimen surface and volume, the scattered primary electrons (PE) and secondary electrons (SE) are detected. An image is generated by moving the electron beam via scan coils on a raster over the sample and counting the incident, scattered electrons at each point. The number of electrons corresponds to the gray scale value in the image as demonstrated e.g. in Figure 4.7 b).

There are different detectors for SEM, e.g. the most common one is the so called Everhart-



**Figure 3.1:** Schema of GEMINI column of the used SEM. The in-lens detector is marked in red [58].

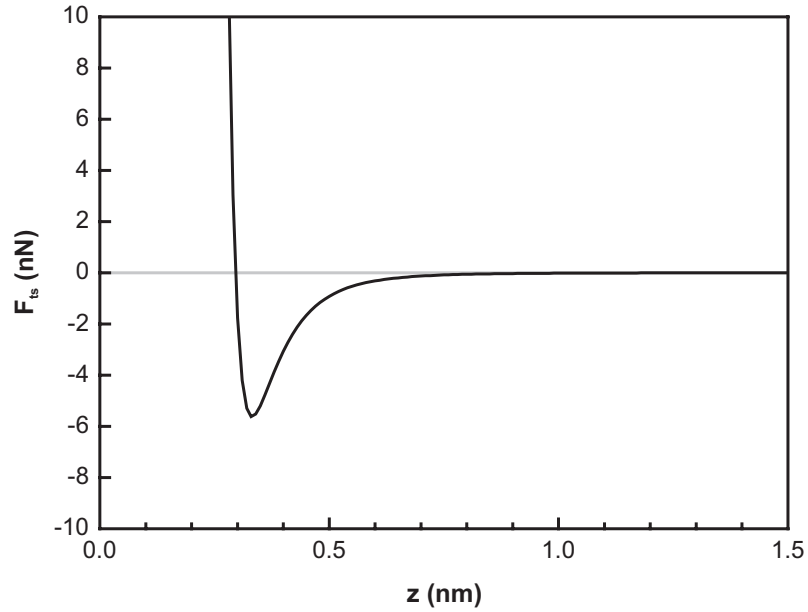
Thornley detector, but as it turned out [59] from the three available detectors at our SEM only the In-Lens detector enables imaging of graphene. For that reason only this detector is described in the following.

Let us return to the interaction of the incident electrons with the specimen. Some of these electrons and also the SE will be attracted by the potential in the column. Due to the reverse movement of these electrons the potential is now attractive and accelerating. These electrons can only be captured with a detector which is placed inside the lens system. From that the name In-lens is derived.

The configuration of this SEM routinely achieves lateral resolutions smaller than 10 nm with a high surface sensitivity which is necessary for the detection of the graphitic layers. Additionally the SEM is equipped for electron beam lithography (EBL). This technique is needed for sample preparation and described in Chapter 4.1.3.

## 3.2 Atomic force microscope

As already mentioned, SEM images give clear information about the position and shape of the flakes of interest, but not their height or number of layers. However, both values, especially the number of layers, are needed to classify the graphene sheets and to distinguish between monolayer, bilayer and few layer samples. Therefore, an additional microscopic



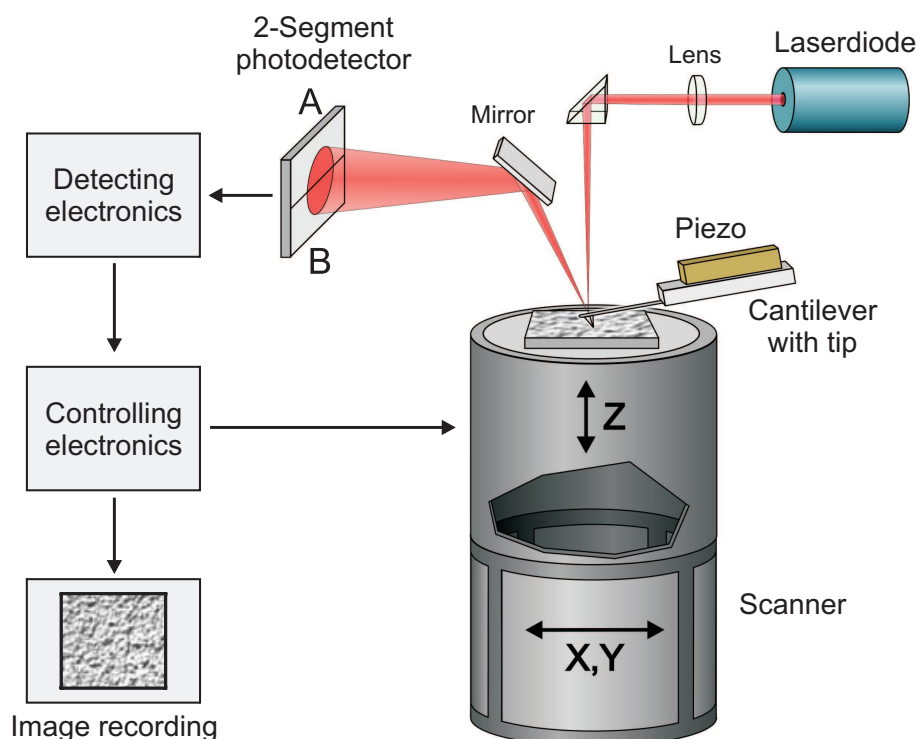
**Figure 3.2:** Lennard-Jones potential describing the force between tip and sample  $F_{ts}$  as a function of the distance between tip and surface. The force-distance curve is non monotonic and generated by short-range and long-range forces.

approach is necessary to provide some information about the topography of a sample. These needs can be met by an **A**tom**i**c **F**orce **M**icroscope (AFM). Since the first AFM [60] was developed by modifying scanning tunneling microscopy (STM) technique [61] in 1986, the elementary working principles are similar.

A sharp tip, which ideally consists of a single atom, is scanned over the surface giving the x- and y-coordinates of the data. The determination of the z-coordinate depends on the chosen AFM mode but in principle all of them measure the force acting between tip and sample. The characteristic force-distance curve is described by a Lennard-Jones potential and shown in Figure 3.2. The expression of the Lennard-Jones potential is (with  $C_1$  and  $C_2$  as constants):

$$V(z) \propto \frac{C_1}{z^{12}} - \frac{C_2}{z^6} \quad (3.1)$$

The details of tip-sample force characteristics are determined by both long- and short-range contributions, e.g. electrostatic, magnetic and van der Waals forces. Additionally, under ambient conditions the sample surface is covered by a thin water film leading to meniscus forces. Contribution and distinction between different forces is rather complex. Interesting reviews on this topic can be found in literature [62–64]. The potential is characterized by two regions where the potential gradient has the same sign and a minimum between these two regions. This leads to the development of several AFM modes since the first AFM was reported [60]. Two main groups are distinguishable, contact modes and



**Figure 3.3:** Drawing of the used *DI Multimode IIIa*-AFM. The tip is at a fixed position and the sample is move by the scanner. The measured signal is the potential difference between the upper and lower half of the photo detector [65].

non-contact modes. All contact modes work on the branch with negative slope the non-contact modes in the region with the positive one. An imaging mode that combines both regions (working near the minimum of the potential) is the so called *tapping mode*<sup>TM</sup>. Here the tip is oscillating with a rather high amplitude  $\sim 100$  nm. This mode was used for all AFM investigations in this thesis since it is a rather simple mode, delivering good results also under ambient conditions. Another advantage of this mode is the energy stored in the oscillating system making it robust against glue residues that are also on the substrate surface. The AFM used in this work was a *Veeco DI Multimode IIIa*. Its components are shown in Figure 3.3. The sample is mounted on a tube that contains piezo elements for a movement in 3 dimensions. The cantilever with the tip is mounted above the sample and fixed in space, meaning that the sample is moved with respect to the tip. The cantilever is excited by another piezo element. The bending of the cantilever is picked by an optical system consisting of laser lens, deflecting prism, mirror and dual segment photodetector. The deflection of the laser at the photodetector is proportional to the force on the cantilever. The recorded quantity in tapping mode is the amplitude modulation. By changing the tip-sample distance, the resonance frequency of the oscillating cantilever is changed resulting in a modulation of the amplitude. The feedback loop acts on this modulation and



the controller makes a z-movement so that the initial amplitude is recovered. In that way the tip sample distance is kept constant. The z-movements are recorded providing the height information and the topography of the sample surface [59, 65]. Other quantities can additionally be recorded such as the phase or the amplitude of the signal.

### 3.3 Imaging ellipsometry

#### Principles of ellipsometry

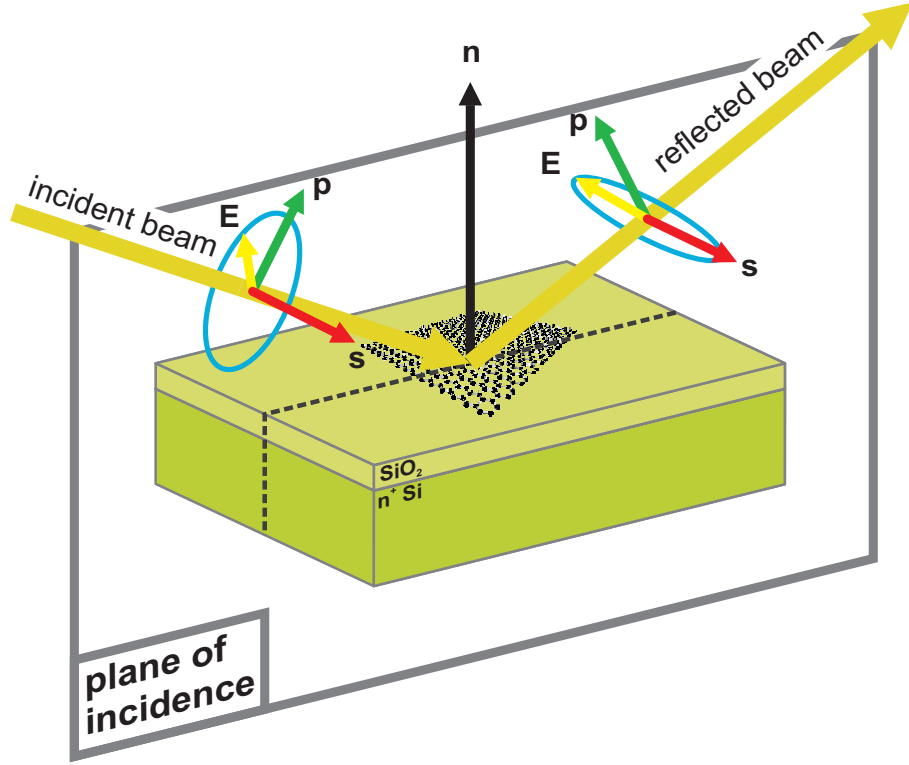
A completely different approach for the characterization of thin films is ellipsometry. This optical, nonperturbing and contactless method has been known for more than 100 years [66] and is very sensitive on the dielectric properties of matter. The change of the known polarization of an incident light beam by reflection on a sample's surface is used to describe optical properties of surfaces and thin films [67–69]. From this either the dispersion relation  $\tilde{n}$  written in terms of refraction index  $n$  and the extinction coefficient  $\kappa$  or the dielectric function  $\tilde{\epsilon}$  with its real- and imaginary part  $\epsilon_1$  and  $\epsilon_2$  can be calculated. Those quantities are related as follows:

$$\tilde{n} = n + i\kappa; \quad (3.2)$$

$$\begin{aligned} \tilde{\epsilon} &= \epsilon_1 + i\epsilon_2 \\ &= (n + i\kappa)^2 \end{aligned} \quad (3.3)$$

The refraction index  $n$  indicates the phase velocity, while  $\kappa$  is related to the amount of absorption loss of light propagating through matter, since every electromagnetic wave light moves on a straight line. But a beam of light is not unambiguously described by its direction of propagation. Additionally, the oscillation orientation of the electromagnetic wave must be defined. This is done with the polarization of an electromagnetic wave. By convention, the polarization is equal to the direction of the wave's electric field vector  $\vec{E}$  [67]. Both the electric and the magnetic part oscillate with the same frequency and the electric field can be separated in two independent linear oscillation. The relative phase between these two linear components define the polarization. If both oscillations are in phase the light beam is called linear polarized, if there is a phase shift of  $\pm 90^\circ$  the polarization vector describes a circular motion. With any other phase difference the resulting light beam is elliptically polarized.

Another property of light is the fact that it is a transverse wave, meaning that the polarization is perpendicular to the direction of propagation. The best coordinate system for the description of light interacting with matter is sketched in Figure 3.4. A beam of monochromatic or quasi-monochromatic light is reflected on a surface under an oblique angle of incidence (AOI) with respect to the surface normal  $\vec{n}$ . The initial beam and the final (reflected) beam define a plane of incidence. Now two additional coordinates are defined:



**Figure 3.4:** Drawing of the principles of ellipsometry introducing a suitable coordinate representation that is parallel  $p$  or orthogonal  $s$  to the plane of incidence.

The first one is parallel to the plane of incidence, denoted by  $p$  and the other is orthogonal to the plane denoted with  $s$ . Due to the properties of transverse waves both coordinates are orthogonal to the travel direction of the beam of light.

With the reflection on the surface,  $s$  and  $p$  component deliver different phase shifts which leads to a change of the polarization. This is a measure of the optical properties of the surface.

$$\vec{E}_{out} = \bar{R} \cdot \vec{E}_{in} \quad (3.4)$$

$$\begin{pmatrix} E_{out,p} \\ E_{out,s} \end{pmatrix} = \begin{pmatrix} R_{p,p} & R_{s,p} \\ R_{p,s} & R_{s,s} \end{pmatrix} \begin{pmatrix} E_{in,p} \\ E_{in,s} \end{pmatrix} \quad (3.5)$$

The incident electric field vector  $\vec{E}_{in}$  is transformed into the outgoing vector  $\vec{E}_{out}$  by the reflection matrix  $\bar{R}$ . This matrix includes all layers leading to a phase shift in  $p$  and  $s$  components. For isotropic materials  $\bar{R}$  is diagonal ( $R_{s,p}, R_{p,s} = 0$ ) and the ratio  $\rho$  of the complex reflection coefficients  $R_{s,s}$  and  $R_{p,p}$  is expressed by two so called ellipsometric

angles  $\Psi$  and  $\Delta$ .

$$\rho = \frac{R_{p,p}}{R_{s,s}} = \frac{E_{out,p} / E_{in,p}}{E_{out,s} / E_{in,s}} \quad (3.6)$$

$$\begin{aligned} &= \frac{|R_{p,p}|}{|R_{s,s}|} \cdot e^{i(\delta_{p,p} - \delta_{s,s})} \\ &= \tan \Psi \cdot e^{i\Delta} \end{aligned} \quad (3.7)$$

The last equation is given by the following definition:

$$\tan \Psi = \frac{|R_{p,p}|}{|R_{s,s}|} \quad (3.8)$$

$$\Delta = \delta_{p,p} - \delta_{s,s} \quad (3.9)$$

The goal of ellipsometry is the determination of the reflection matrix. Since this is a rather complex situation, an appropriate model for the surface must be developed. If the measured values in terms of angles  $0^\circ \leq \Psi \leq 90^\circ$  and  $-180^\circ \leq \Delta \leq +180^\circ$  fit to this model, the optical properties of the investigated sample are well described by the model.

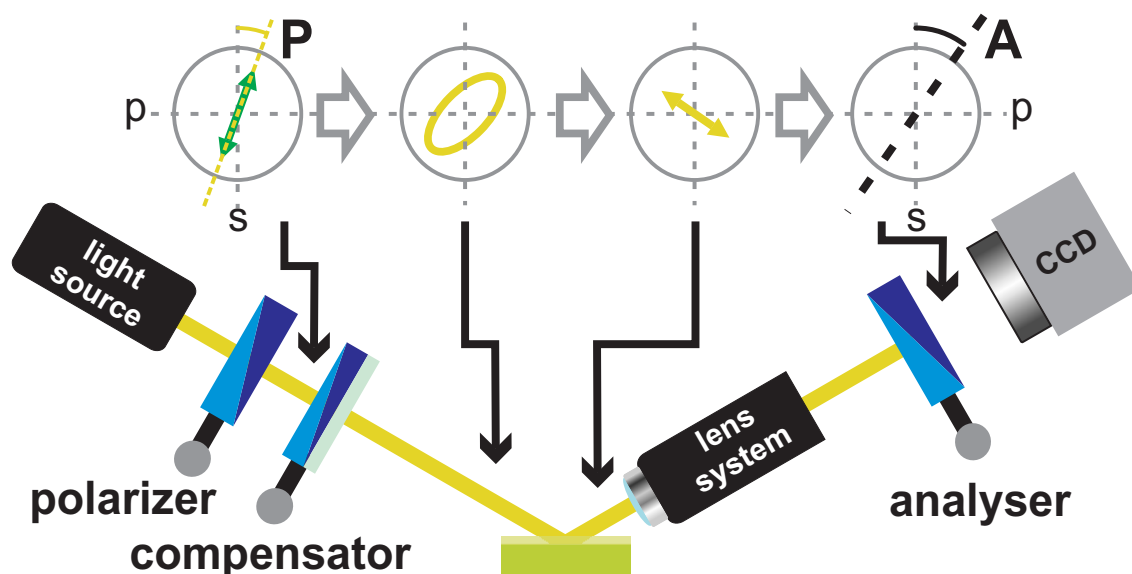
### Setup for imaging ellipsometry

Conventional ellipsometry is limited in lateral resolution to the diameter of a light spot of typically 100  $\mu\text{m}$ . This can be overcome by adding a lens system as additional optical element to the setup, as depicted in Figure 3.5. This leads to **Imaging Ellipsometry** (IE). The incident beam is first polarized (P), passes through the compensator<sup>1</sup> (C), is reflected by the sample surface (S) and focused by a lens through an analyser (A) onto a CCD camera. This is a so called PCSA-setup. A focused image can be obtained by moving the focus line over the sample by a lens to level the angular light incident. The lateral resolution of IE is only given by the numerical aperture of the microscope objective and reaches  $\sim 1 \mu\text{m}$ .

The required quantities in equation (3.7) can be measured by the concept of nulling ellipsometry. The steps performed in such a measurement are schematically depicted in Figure 3.5. The nulling condition at which the light intensity at the CCD camera is minimal is generated in such a way, that the polarizer and/or compensator is rotated until the reflected light is linearly polarized. Then the analyzer detects this state by a rotation until the minimal intensity is reached which is equivalent to a  $90^\circ$  rotation between the analyzer's axis and the linear polarized reflected light. This gives the orientation of electric field and simultaneously the state of polarization of both the incident and reflected beam.

One advantage of this technique is that only a minimum in the light intensity at the CCD

<sup>1</sup>The compensator is a  $\lambda/4$  plate



**Figure 3.5:** Setup for imaging ellipsometry. The circles show the polarization direction for nulling imaging ellipsometry after each component.

camera must be found and that only angles of the optical components have to be determined which can accurately be done. A more detailed discussion on imaging ellipsometry on multi-layer systems is given in literature [70].

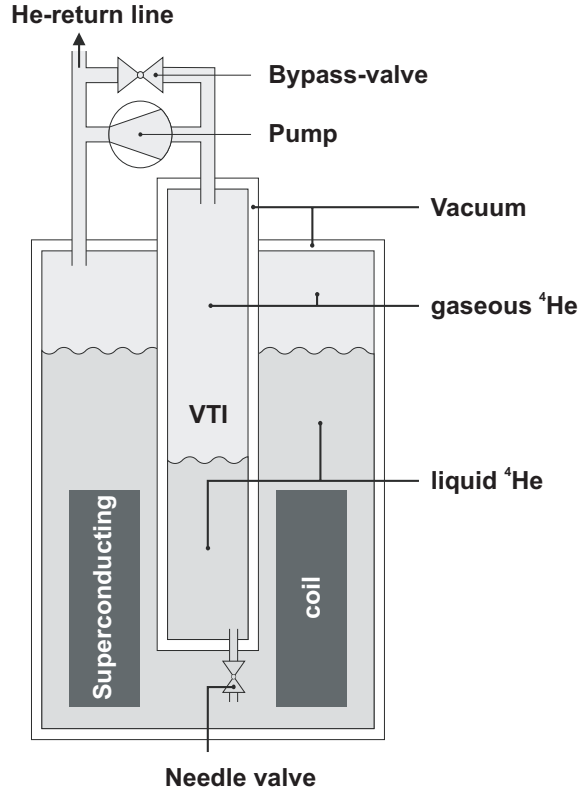
The nulling imaging ellipsometer *nanofilm\_ep3-se* (Accurion, Göttingen, Germany) delivers different wavelength ranging from  $\lambda = 360$  nm to  $\lambda = 1000$  nm (bandwidth  $\pm 20$  nm). For higher light intensities the system is equipped with a laser ( $\lambda = 532$  nm). A 20x- or 50x-objective are available, the latter gives  $68 \times 79 \mu\text{m}^2$  field of view. All measurements were carried out in cooperation with Accurion.

### 3.4 Magnetotransport measurements

The second part of this work does not deal with microscopic studies of the graphene but with the investigation of the electronic properties of those layers. In the following the used setup is shortly described.

The magnetotransport measurements were performed in an  $^4\text{He}$ -Oxford-Cryostat (Figure 3.6) with a **V**ariable **T**emperature **I**nsert (VTI) and a superconducting magnet that can achieve a maximum magnetic flux density of 10 T. The sample is placed with help of a sample holder inside the VTI which is connected to the surrounding liquid Helium reservoir via a needle valve. All other parts of the VTI are decoupled from the bath by a inner vacuum shield.

The sample holder is designed for a standard 20 pin chipcarrier and equipped with a Si-



**Figure 3.6:** Drawing of the cryostat. Magnetic fields up to 10 T can be applied. The sample is mounted in the VTI which enables temperatures from  $T=1.7$  K to nearly room temperature [71].

diode sensor to take the temperature close to the sample by its temperature dependent resistance. The sample temperature can differ a lot to the temperature measured at the VTI during cooling down, hence the diode is needed to get reasonable curves of the temperature dependent resistivity of the samples. Filling the VTI volume with liquid Helium leads to a standard temperature of  $T = 4.2$  K. The temperature can be reduced to  $T \approx 1.7$  K by reduction of the gas pressure in the VTI by pumping. A resistance heater allows temperature up to  $T \approx 200$  K.

Electrical characterization of the samples and magnetotransport measurements have been performed using standard DC and AC set-ups [50,51,72]. DC measurements were carried out with a parameter analyzer and low frequency AC measurements with up to four Lock-In amplifiers depending on the number of contacts. One was used as voltage source which generates combined with a ohmic resistor an oscillating current. Typically 100 nA were used with an excitation voltage of  $U_0 = 0.1$  V and a  $1 \text{ M}\Omega$  resistor. An oscillation frequency of 17 Hz or 13 Hz was chosen to avoid noise injection especially by the power line. All instruments were additionally thoroughly grounded. Gate voltages were applied

via DC voltage sources. The measurement instruments are read out by a computer which is connected to the setup via GPIB.

## Chapter 4

# Preparation and detection of graphene

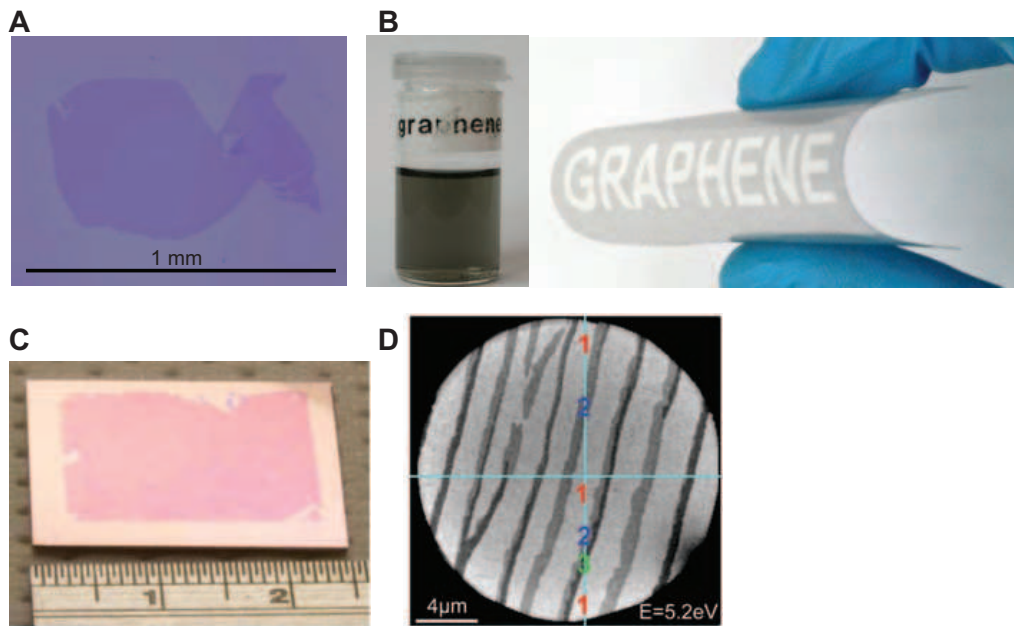
Graphene, a one atom thick sheet of carbon atoms, has to be sufficiently isolated from its environment and need at the same time a substrate to be stabilized. Without lying on a surface a two-dimensional crystal can not exist thermodynamically and will be crinkled [73,74]. Nature strictly forbids the formation of a two-dimensional (solid state) material [2, 14]. The conflict that a substrate is required but influences of the environment including bounding to the substrate have to be prevented is challenging in particular with regard to the reproducible fabrication of graphitic flakes with evaporation techniques on an industrial scale with feasible properties [14]. In this chapter first an overview about state of the art fabrication methods to produce graphene sheets will be given. Advantages and disadvantages of the different techniques will be briefly discussed. Next the different substrate materials used in this thesis will be introduced, in particular the inconvenient crystalline III-As based substrates. Then the steps from peeling off a sheet of graphene by micromechanical cleavage to a contacted and wired graphene sample for electrical characterization will be described in the following.

The challenge of identification and classification of graphitic sheets on arbitrary substrates can be solved with comparison of different microscopy and spectroscopy methods such as scanning electron microscopy, atomic force microscopy, imaging ellipsometry and Raman spectroscopy. This will be described in the second part. A comparison of the detection methods will close the chapter.

## 4.1 Fabrication of graphene samples

### 4.1.1 Roads towards graphene

Graphene can be made in two principle ways. One way is the mechanical cleavage of bulk graphite into individual atomic planes and deposition on a substrate. The other one is the growth of graphene on top of an appropriate substrate and transferring it to an intended

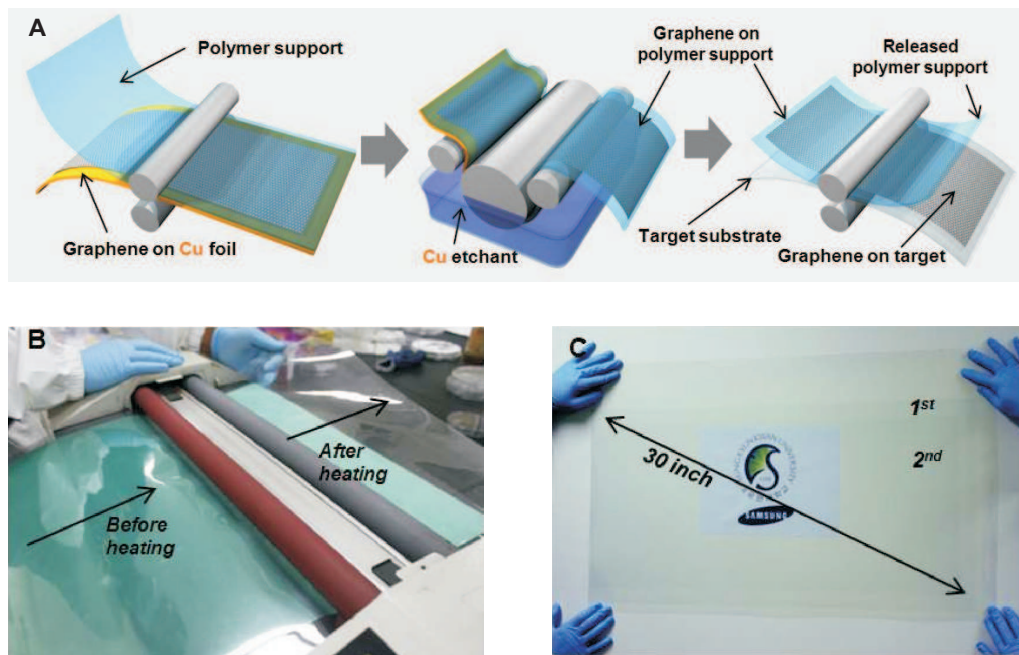


**Figure 4.1:** Making graphene. **A:** Large graphene crystal prepared on an oxidized Si wafer by the scotch-tape technique. **B:** Left panel: Suspension of microcrystals obtained by ultrasound cleavage of graphite in chloroform. Right panel: Such suspensions can be printed on various substrates. The resulting films are robust and remain highly conductive even if folded. **C:** The first graphene wafers are now available as polycrystalline one- to five-layer films grown on Ni and transferred onto a Si wafer. **D:** State-of-the-art SiC wafer with atomic terraces covered by a graphitic monolayer (indicated by "1"). Double and triple layers ("2" and "3") grow at the steps, image and description from reference [14].

surface or the reduction of SiC under high vacuum [14]. An overview of the different techniques is given in more detail in references [2, 14, 75]. For the reduction of graphene, (0001) 6H-SiC wafers are heated to  $T \sim 1300^\circ\text{C}$  under ultrahigh vacuum conditions [76, 77] or under an argon atmosphere [78]. This seems to be a very promising way because of the insulating substrate essential for electronic devices. SiC exhibits a Si and a C terminated faces resulting in two different growth modes. Si terminated faces constitute single, double and tri-layer graphene, and on C terminated faces multilayer sheets. Among others there are still some difficulties like lattice mismatch between SiC and graphene, strong coupling to the substrate, an intermediate layer and the rotational disorder (no Bernal stacking) [14, 76–78].

The other epitaxial process is the growth of graphene on ultraflat metallic surfaces (e.g. Cu, Ni) by **C**hemical **V**apor **D**eposition (CVD). This procedure has been known for a couple of years [79]. The graphene layers grow on the catalytic metals (e.g. copper foils) at temperatures up to  $1000^\circ\text{C}$  using a mixture of methane and hydrogen, resulting in layers with  $\sim 1\text{cm}^2$  [80]. Nickel and copper were already used for growing single graphene

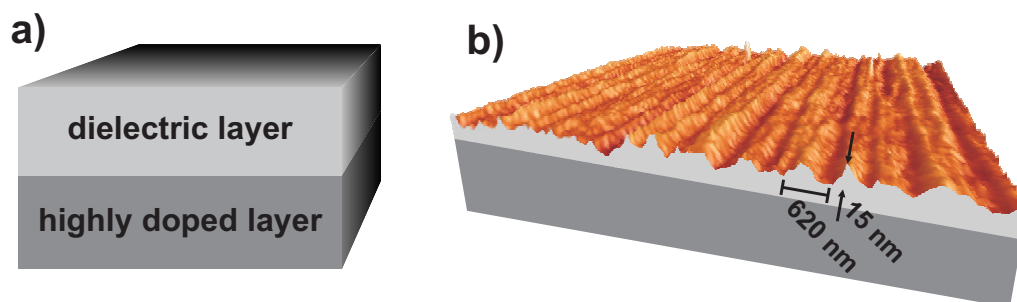




**Figure 4.2:** **A** Schematic of roll-based graphene production. The films grow on a Cu foil. With the usage of a supporting polymer the copper can be etched away and the graphene can be transferred on a target substrate. **B** picture of the transfer step. **C** a transparent ultra-large-area graphene film on a PET sheet, adapted from reference [83].

layers [80–83]. Actually considerable efforts are needed and done to improve the transfer step of the atomic layers from the metal to insulating substrates. In a recent preprint the breakthrough for the fabrication and transfer of very large high-quality graphene sheets with a roll-based production method was reported [83]. The principles of this production techniques and the resulting graphene sheets are depicted in Figure 4.2. Raman spectra suggesting very good crystal quality and purity of the material, high transparency and sign of conductivity minima at room temperature close to zero gate voltage, indicating low intrinsic doping, have been reported for the 30 inch large graphene mono- and bilayers as well as it is possible to measure quantum Hall effect on these layers [83].

The second route is to separate the planes of a piece of bulk graphite into individual graphene flakes. This can be done on the one hand in solution by pure ultrasonic cleavage or chemically assisted to make the sonification more efficient. This leads to a stable suspension of graphene crystallites with submicrometer size that can be used to make polycrystalline films and composite materials [14]. On the other hand individual graphene sheets can be peeled off from a piece of bulk graphite by an adhesive tape and transferred to a substrate. This technique often is referred to as the "scotch tape method" which was the first one used to prepare graphene. The development of this method by A. Geim and coworkers in 2004 was the kick-off for the intense graphene research over the last



**Figure 4.3:** a) schema of the used substrates - a highly doped layer that is usable as backgate electrode is covered by a dielectric material; b) 3D-AFM picture of the used InGaAs substrate - the surface has a periodic like morphology with a periodicity of  $\sim 600$  nm and a height of  $\sim 15$  nm. This values change slightly on the entire wafer.

years [1]. This easy and cheap method allows the fabrication of high-quality graphene samples with very high electron mobility for basic research and to prove basic device concepts [14]. However, the method is very time consuming, generates only samples below 1 mm of edge length [14], mostly only in the range of tens of micrometers handicapping the detection on non Si/SiO<sub>2</sub> substrates as will be described below and hampering e.g. transport experiments in different geometries on one flake for better comparison. Nevertheless, we have applied micromechanical cleavage to fabricate our graphene samples to be independent from other groups. This approach will be introduced in more detail subsequent to the presentation of the used substrates.

#### 4.1.2 Preparation of graphene on various substrate materials

As previously described most of transport investigations have been carried out on graphene on Si/SiO<sub>2</sub> with a certain thickness of oxide due to the visibility even of monolayers under an optical microscope. The influence of the substrate, especially substrate phonon-modes and (un-) charged or magnetic impurities have been theoretically covered [84–86], but minor experimental work has been carried out of exfoliated graphene on non Si/SiO<sub>2</sub> substrates. There are few optical investigations of graphene on GaAs, sapphire and glass [27, 28, 87] and a report of the mobility enhancement for few-layer graphene lying on top of a ferroelectric  $Pb(Zr_{0.2}Ti_{0.8})O_3$  (PZT) substrate that is ascribed to reduced scattering due to strong screening of PZT [22]. The mobilities are comparable to those in suspended flakes. The mechanisms limiting the mobility and the influence of the substrate e.g. on quantum interference phenomena such as weak localization phenomena (WL) remain still unclear. This is why we are interested on graphene on crystalline semiconducting substrates. In the following the preparation of such graphene devices for optical and electrical measurements will be described.

substrate name	doped layer	dielectric material	$d_{\text{dielectric}}$ (nm)
SiO <sub>2</sub>	n <sup>+</sup> Si	amorphous SiO <sub>2</sub>	300
GaAs	n <sup>+</sup> (001)-GaAs	crystalline AlGaAs	600
GaMnAs	n <sup>+</sup> (001)-GaAs	crystalline GaMnAs	35
InGaAs	n <sup>+</sup> (001)-GaAs	crystalline InAlAs	1512

**Table 4.1:** Table listing the used wafer, together with some characteristic values. All thicknesses of the dielectric materials are the nominal values.

### Substrate materials and preparation

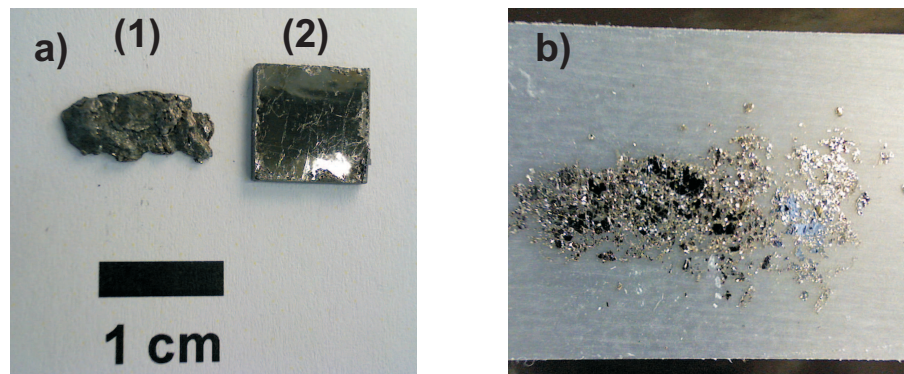
All used substrates consist of a similar two layers structure. The thicker layer is highly doped and the thinner one on top acts as dielectric material and simultaneously as the real substrate upon which the graphene sheet is deposited. The principal layer sequence is depicted in Figure 4.3 a). The highly doped layer works as back-gate electrode to have the possibility to change the Fermi-energy  $E_F$  in the graphitic flakes via field effect. Besides the standard substrate of 300 nm SiO<sub>2</sub> on highly n-doped Si, we used GaAs-based crystalline substrates grown by **M**olecular **B**eam **E**pitaxy (MBE) in the group of Prof. Werner Wegscheider in Regensburg and the Si/SiO<sub>2</sub> wafer are commercial ones (supplier: *Si-Mat* Company Landsberg/Lech, Germany). The MBE growth allows precisely tailored substrates with a high crystal quality and purity. All III-As substrates are grown on highly n-doped (001) GaAs wafers and listed in table 4.1 and referred to as semiconducting substrates if there is no need to distinguish them. The dielectric layer consists either of undoped GaAs, an undoped GaAs/AlGaAs layer sequence, slightly Mn doped insulating GaMnAs layer or undoped InGaAs layer on top of an undoped metamorphic buffer. More details on the growth can be found in literature [88] and an overview of the most important sample parameter is given in table 4.1. The exact layer structures are given in Appendix C. Apart from the InGaAs substrates all other substrates are rather smooth with a **R**oot **M**ean **S**quare (RMS) roughness of less than 1 nm. Because of the metamorphic growth the InGaAs wafer feature an intrinsic texture, which is illustrated by a stereoscopic AFM image in Figure 4.3 b), where the periodic cross-hatched morphology is clearly visible. Due to peculiarities at the MBE growth, height and periodicity changes a little over the entire wafer [88]. In the shown region the height from bottom to apex is about  $\sim 15$  nm and the vertical extent of one period is  $\sim 620$  nm. As depicted the morphology does not exhibit a homogeneous sinusoidal periodicity, because the shape of the elevations sometimes has a sharp profile and additional bumps. The GaAs/AlGaAs multilayer and the GaAs substrates are nominally undoped, but there is also an intrinsic amount of impurities in the crystal with a density well below  $10^{16} \text{ cm}^{-3}$ . The Mn doping of the GaMnAs wafer has to be done at very low growth temperatures involving lattice defects and this is why we have some magnetic moments and a p-type doping from the Mn in the range of  $10^{18} \text{ cm}^{-3}$  and simultaneously n-type doping from Mn interstitials and As antisite defects both acting

as double donors. The GaMnAs is insulating especially at low temperatures but there is a huge amount of charged impurities that could act as scatterer [88]. We have to mention that some Ga droplets are sometimes present on the surface of the semiconducting MBE grown substrates known as oval defects, but for transport experiments these parts of substrates have not been used. With this variety of substrates it should be possible to study the influence of impurities in the substrate and rough surfaces on the properties of graphene in comparison to the standard amorphous SiO<sub>2</sub> substrates.

For graphene deposition the substrates with resist-protected surfaces are cleaved into typically 3.5×3.5 mm<sup>2</sup> pieces. Some pieces are patterned by optical lithography and metal evaporation with a grid for better reorientation and finding of graphene flakes, especially IE and Raman experiments were carried out on such samples. This is also very useful for SiO<sub>2</sub> substrates, but it turned out that the practicability is limited for semiconducting substrates. For those a SEM is needed to find the graphene flakes and alignment marks can be processed by **Electron Beam Lithography (EBL)** directly around the interesting flake resulting in both a better workflow during graphene detection and higher accuracy for electric contacting the flakes. Lithographic techniques will briefly be described below and recipes lists of the different steps can be found in appendix B. For electrical characterization the samples are patterned with a contact to the highly doped back gate electrode. After the sample surfaces are carefully cleaned in acetone and isopropanol ultrasonic bath and dried with a dry nitrogen flow, the substrates are ready for graphene deposition.

### Deposition of graphene by micromechanical cleavage

As already mentioned, graphene is deposited on the substrate surface by micromechanical cleavage as numerously described in literature and in references therein [6, 89]. Natural graphite is mined all over the world, but there are also some ways to synthetically produced graphite. We used both synthetic **H**ighly **O**riented **P**yrolytic **G**raphite (HOPG) (Supplier: *Schaefer Technologie GmbH* Langen, Germany) and natural graphite (Supplier: *NGS Naturgraphit GmbH* Leinburg, Germany). Pictures of the basic materials are given in Figure 4.4 a). To peel off graphene from graphite and subsequent transfer it to the substrate adhesive tapes (Supplier: *Scotch Magic Tape 3M*) are used. Therefore a piece of graphite is pressed onto the tape and the rest is removed. Folding and opening the tape several times peels off individual flakes and spreads them over the entire tape. The procedure can also be done or repeated with further tapes. At some spots of the tape there will remain some (large) graphitic flakes. A picture of the adhesive tape with graphene is shown in Figure 4.4 b). In the next step the substrate is put onto the tape, slightly pressed on and carefully removed. Van-der Waals forces between graphene and substrate are strong enough to allow flakes to withstand cleaning in acetone and isopropanol to remove glue residues caused from the adhesive tape. After detection of the graphene flakes and if required the patterning of alignment marks with EBL and Ti/Au ( $\sim 5$  nm/40 nm) evaporation visible in Figure 4.5 b), the sample can be prepared for electrical measurements.



**Figure 4.4:** Materials for graphene preparation. a) Two kind of graphite have been used: natural graphite (1) and HOPG (2). b) Graphitic flakes are cleaved using Scotch tape. A part of such a strip lies on a black background

Since the detection of graphene on non-SiO<sub>2</sub> substrates is very special, it will be described in detail in an own section at the end of this chapter.

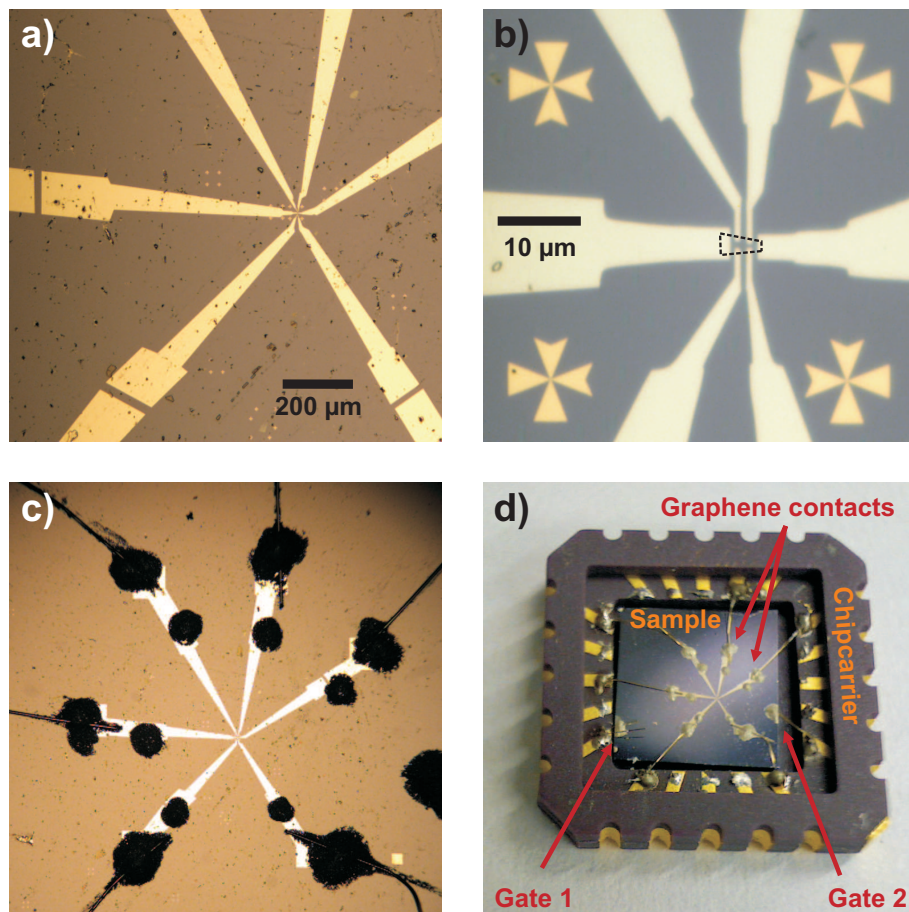
### 4.1.3 Preparation of graphene samples for electrical measurements

For electrical characterization and transport measurements in field effect transistor like devices at least 2 ohmic contacts to the graphitic layer and one ohmic contact to the gate electrode is needed. Mostly 2 contacts to the gate are prepared prior to graphene deposition and the number of contacts to the graphene flakes depends on size and shape of the flake. The contacts are aligned in a van-der Pauw geometry [90].

#### Contacts to the gate-electrode

For the contact to the gate electrode, the dielectric layer was etched away with **Reactive Ion Etching (RIE)** in the case of SiO<sub>2</sub> and wet chemically in the case of semiconducting substrates. Next Ti/Au (5 nm/150 nm) as contact to the n-doped Si layer and Pd/Ge (25 nm/50 nm) to the n-doped GaAs layer was evaporated. After the lift-off process, the contacts are annealed under a forming-gas atmosphere at 450 °C for 20 min (Si) and at 250 °C for 60 min for GaAs. The gate-contact characteristic was checked at room temperature as well as at  $T = 4.2$  K and with the described steps highly linear current-voltage characteristics have been observed for the semiconducting substrates (see also chapter 6.1.1) and sufficiently linear behavior for the Si layers. We tried two alternative and very easy routes to prepare the contact to the gate electrode either by soldering it with In on the scratched surface of substrate comparable to the fabrication of ohmic contacts to two dimensional electron gases in GaAs/AlGaAs heterostructures [88] or by using conductive silver at the substrates back-side. However, in both cases and for all substrates still a





**Figure 4.5:** Optical images of a graphene on GaAs sample. In a) the gaps in some of the leads are visible. b) A zoom in to the graphene layer, indicated by the dashed line. c) The sample is connected to the chip carrier and the gaps are closed by conducting silver. d) The complete chip carrier with the sample mounted, ready for transport measurements.

Schottky barrier between the doped semiconductors and the metal is formed resulting in a diode-like contact characteristic.

### Contacts to graphene

Contacts to graphene are prepared by electron beam lithography. This technique combines the property of a SEM to move a defined electron beam on a certain path with the sensitivity of an appropriate resist for exposure with such an electron beam to write the desired structure into the resist. The long chains of such a polymer based resist (in this work **P**oly**m**ethyl**m**ethacrylate (PMMA) was used) get cracked by the energy of the accelerated electrons. With a suitable developer it is possible to dissolve the shortened chains

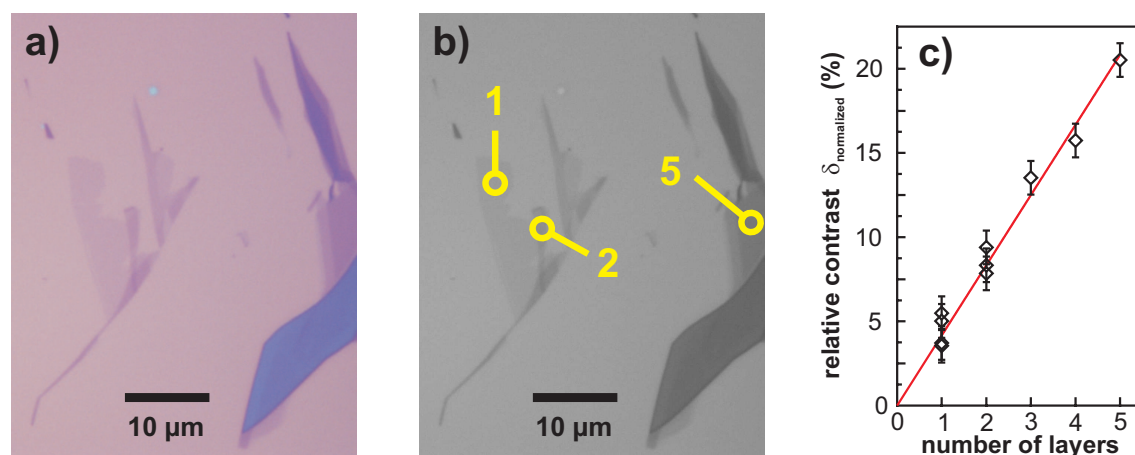
with respect to the longer unchanged ones that still cover the surface. Since no masks are needed individual geometries with high lateral accuracy can be realized. Routinely dimensions smaller than 100 nm can be achieved and with special techniques below 10 nm [51]. More details on the used EBL system can be found in references [65, 91, 92], realization and preparation of very small nanostructures can be found e.g in references [50, 51].

After the spin coating of the sample with a PMMA double layer system and baking the resist layers (the exact parameters are given in Appendix B), the writing process starts with aligning the sample in the SEM using the alignment marks defined before and then the contact layout is written into the resist. The geometry is individually designed for each graphene flake. For required accuracy the contacts are written in several steps in concentric areas starting with the innermost area, where the contacts have an overlap with graphene. To overcome uncertainties by movement of the sample-stage, the first and second part of the contact leads are written without moving the sample-stage. Since the whole layout is too big to write it within one scanning area, now the sample-stage is moved and the next fields can be written, if the single elements of the next field overlap by  $\approx 20 \mu\text{m}$  to make sure that the elements are connected. After exposure, the resist is developed and then metal is evaporated. Lift-off is done in warm acetone that removes the remaining resist and simultaneously the metal on the unexposed areas. Finally only the written parts are covered with metal. Palladium (Pd), Ti/Au and Cr/Au were evaporated as contact materials. The best results and lowest contact resistance ( $\lesssim 1 \text{ k}\Omega$ ) were achieved with 40 nm Pd. Consequently, Pd was used to prepare ohmic contacts to graphene at most of the samples.

The design and the different steps are demonstrated on one sample shown in Figure 4.5. We want to refer to a peculiarity in the sample layout: To prevent the graphene flake from destruction by a electrostatic discharging during the preparation process, a small gap between inner leads and the outer part is introduced as clearly visible in Figure 4.5 a). This gap is closed as last preparation step as depicted in Figure 4.5 c).

### Assembly into chip carrier

The last preparation step is mounting the sample into a standard 20 pin chip carrier that is used for putting the sample into the sticks for transport measurements. Usually the electrical connections between the pads on the sample and the chip carrier are done with an ultrasonic wire bonder. With some experience and after destruction of some graphitic sheets we decided to connect the contact pads both to graphene and to gate electrodes with thin gold wires using conductive silver at the sample side and soldering with indium at the chip carrier side as depicted in Figure 4.5 c) and d). Finally the soldering at the chip carrier is secured with conducting silver and also the gaps of the contact leads at the sample are closed by painting with conducting silver. A sample ready for transport characterization is shown in Figure 4.5 d).



**Figure 4.6:** Optical micrographs of graphene and few layer graphene on SiO<sub>2</sub> and their relative contrast. a) Color image taken with white light. b) Image from a) in grey scale representation. The yellow numbers correspond to the number of layers. c) relative contrast normalized to the background. The number of layers and their contrast scales linearly.

## 4.2 Detection and the number of layers

It is not surprising that graphene can be deposited with the micromechanical cleavage technique on nearly every arbitrary substrates. The challenge to be solved is the detection of the atomically thin graphitic sheets. Typically the produced flakes are some μm to few tens of microns long and hence are clearly smaller (more than 100.000 times) than the dimension of the substrate ( $\sim 3.5 \times 3.5 \text{ mm}^2$ ). As already mentioned, graphene on the standard Si/SiO<sub>2</sub> substrate is visible under an optical microscope, but this is not the case for the other used substrates. Here a combination of different microscopy and spectroscopy techniques is necessary to find and classify graphene on arbitrary substrates. Those will be introduced in the following.

### Optical microscopy

For this method an optical microscope is used and the resulting contrast between graphene and the background is evaluated. This is a very impressive technique, since the optical microscope only leads to a magnification and the detection of monolayers is "only" done by the human eye. Therefore, it is possible to scan rather fast over the surface and the detection of graphene is not very time-consuming. The drawback however is that this technique only works with the use of Si/SiO<sub>2</sub> substrates with certain thicknesses of the oxide layer [23, 93–95] or substrates having similar optical properties as e.g. 300 nm SiO<sub>2</sub> [28, 96]. The oxide thickness of 300 nm is a very crucial parameter and a deviation of more than  $\pm 5\%$  leads to a strong decrease of the contrast [2] between graphene and



the bare substrate. The mostly used thickness is 300 nm due to the possibility to see monolayers of graphene with white light illumination without any filter [23, 93–95] what is accessible with nearly every optical microscope.

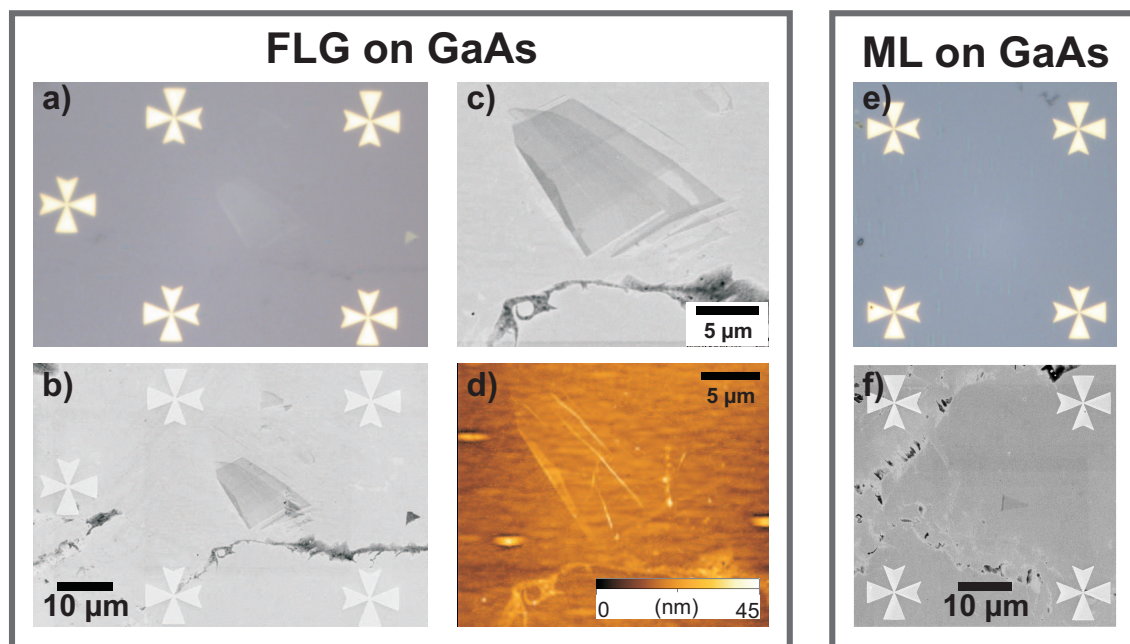
Such an optical image is shown in Figure 4.6 a) and b). In Figure 4.6 a) the RGB colors are taken with a CCD camera mounted on the microscope and in Figure 4.6 b) the colors are transferred to grey scale representation. The yellow numbers correspond to the number of layers in the circled areas. These numbers are determined by taking the relative contrast between the grey scale values  $G$  of the image [23, 93–95]:

$$\delta = \frac{I_{carbon} - I_{background}}{I_{background}} \quad (4.1)$$

The grey scale values for the above data are averaged over 20 pixel values for the carbon area and the background, respectively. It is worth mentioning that the background value changes a little over the image. Therefore it is necessary to determine the background values in the neighborhood of each carbon area. In Figure 4.6 c) the relationship of different regions of Figure 4.6 b) is plotted (only three selected areas are circled in the image). A linear relationship between the number of layers and the relative contrast can be deduced. In this image the slope of the linear fit has a value of 0.042 denoting that each layer absorbs  $\sim 4.2\%$  of incident light. The given errors are overestimated compared to the RMS values due to the uncertainties in random choice of the pixels. The slope changes a little from sample to sample but a few percent seems to be realistic [95, 97]. The deviations might be caused by small angle deviation from non identical sample mounting on the microscope, different numerical apertures of the used objectives or changes of the background by e.g. tape residues. With some experience the number of layers can be distinguished with high accuracy employing this technique. Other methods such as Micro-Raman, magnetotransport measurements [98] or AFM have confirmed the number of layers determined with the optical microscope available in our group.

It was already mentioned that the substrate material, even the oxide thickness is a very crucial parameter for this method. This annoying fact is confirmed in this work. Here the focus was not changing the  $\text{SiO}_2$  thickness but the whole base material was switched to III-As semiconductors. In Figure 4.7 a) and e) two examples of optical microscope images of a few-layer graphene (FLG) and a graphene monolayer (ML) on GaAs substrates are depicted. These images are taken with white light illumination. The FLG flake is hardly visible in an optical micrograph and nothing is visible for the ML graphene. Only the SEM image in Figure 4.7 f) shows that there is a flake and with help of AFM measurements the height was determined to less than  $\lesssim 1$  nm and therefore this flake can be classified as a monolayer.

From this results it follows that another microscopy technique is needed for locating graphene on the semiconducting substrates.



**Figure 4.7:** Comparison between different microscopy techniques applied to a few-layer graphene a)-d) and a monolayer graphene flake e) and f). Yellow/white crosses are metallic alignment marks. a) Optical microscope and b) SEM image of the same flake, even a few layers are not clear distinguishable at the optical microscope image in contrast to a SEM picture. c) zoomed SEM micrograph of image b) - different layers are clearly visible. d) AFM investigation of the flake confirms the layered structure of the flake. The oval white spots are Gallium droplets embedded in the substrate. e) A graphene monolayer is not visible in white light of the optical microscope. f) The monolayer is clearly detectable in SEM.

### Scanning Electron Microscopy

Another option for microscopy is the use of a SEM. This leads to images of higher resolutions but it is much more time consuming since only one single detector is addressed and therefore the image is serially generated.

To take SEM images typical acceleration voltages of a few kV ( $U_{acc} \leq 6$  kV) were used and in particular for GaAs normally 2 kV are applied. As it has been shown in previous work [59] an inlens detector is necessary to obtain good images from graphitic sheets. To avoid damages of the graphitic layers [99, 100] the resolution was often reduced and only the minimized needed exposure time was chosen. The mechanism to built a picture from graphene with a SEM is not well understood so far and is beside the focus of this work. Nevertheless, one possible mechanism can be discussed here. The experimental findings are the following (for a SEM image of FLG on GaAs see Figure 4.7 c)):

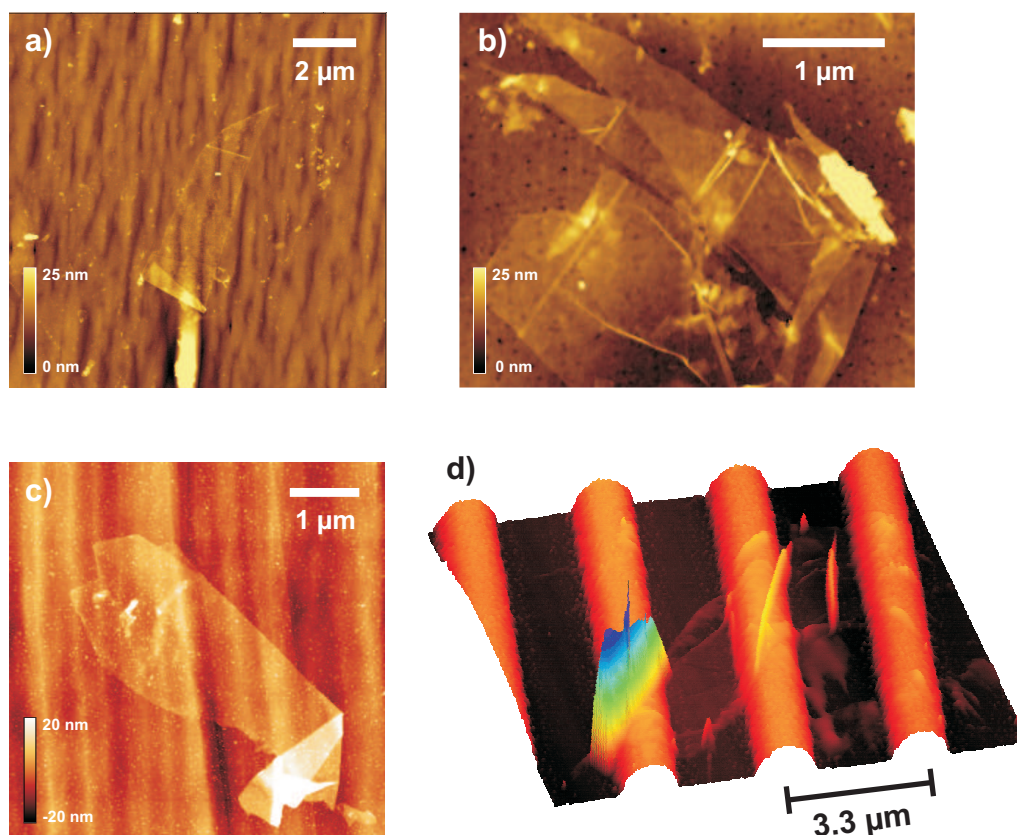
- Few layer graphene down to monolayers are darker than the surrounding substrate

- Within one flake, thicker regions (more layers) appear darker than thinner ones
- The increasing contrast works up to a layer thickness of  $d \sim 15$  nm.
- For thin graphite layers (thicker than  $d \sim 15$  nm) the situation is inverted. The thicker the flakes the brighter the SEM image ending with the high contrast known for graphite and more generally for metals.

The picture generation in SEM is mostly determined by secondary electrons (SE). These are created by repeated random scattering and absorption of the incident primary electrons (PE) with a teardrop-shaped volume of the specimen (interaction volume) [101]. Since the FLG sheets are thinner than a typical interaction volume (penetration depth  $\gg 100$  nm), the SE are also generated within the substrate and have to pass the carbon layer on top. As they have less energy than the PE, there is some probability that a low energetic SE can not pass through the FLG. It is absorbed within the FLG. This could explain the darker color of the FLG and the increasing contrast with increasing layer thickness, because the flakes become darker for thickness  $d$  up to  $\sim 15$  nm. The finding that thin graphite layers again get brighter might be explained by a SE generation within the semi-metallic graphite, where it is easier to release an electron from the metallic material. It seems that the image formation must be described by two different mechanisms, however detailed studies are lacking at the moment. Investigations of the origin of these contrasts might be done e.g. by systematically exploring the dependence of the contrast on the acceleration voltage or capturing images in a tilted geometry. A similar effect was found by reflection measurements in the optical regime [93]. There a contrast inversion for an increase of the layer number is reported, too. This effect is visible in the optical image of graphene on  $\text{SiO}_2$  in Figure 4.6 a).

Examples for such SEM images are assembled in Figure 4.7 b), c) and f). In contrast to optical microscope the single layer graphene is also detectable with SEM (Figure 4.7 f). The FLG including its substructure is clearly visible in Figure 4.7 b). The images show the same regions of a sample. The FLG in Figure 4.7 a) to d) shows the mentioned increase in the contrast for increasing number of layers. The AFM image in Figure 4.7 d) confirms the layered structure of the flake with more than two sheets.

These findings enable the detection and locating of single and few-layer graphene samples on all introduced semiconducting substrates by means of SEM. The disadvantage of this technique is the slow image capturing speed and that no distinct number of layers can be determined since the contrast varies from sample to sample. There a cross-check with another technique is needed. Possible explanations for the changes might be surface inhomogeneities from peeling away the adhesive tape during preparation. Another source for different behavior could be different discharging by either non-uniform sample mounting or non-uniform conductivity of the substrate. The latter could be excluded, since the conductance is averaged over a large volume and MBE growth is rather a reliable technique.



**Figure 4.8:** AFM images of graphene layers on different substrates: a) Graphene on GaAs-substrate with a layer thickness of  $\sim 0.7$  nm, b) on GaMnAs-substrate with a layer-thickness of  $\sim 1.5$  nm, c) on InGaAs-substrate with a layer thickness of 1.6 nm; additionally resist residues are spread over the flake, d) Few-layer graphene ( $\sim 5$  nm high) on pre-patterned  $\text{SiO}_2$  halfcylinders with a height of the cylinders of  $\sim 85$  nm. Graphene follow textures of the substrates very closely as visible for all shown substrates.

### Atomic Force Microscopy

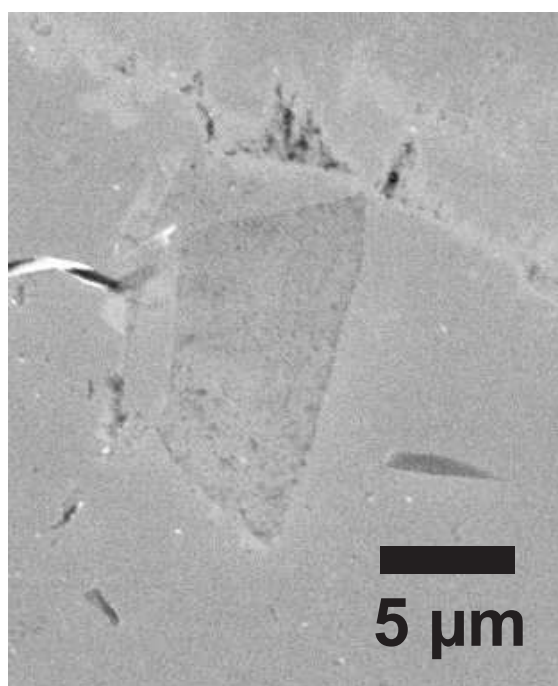
As remarked above with SEM images it is not possible to distinguish the exact number of layers of a graphitic flake. This is why an additional experimental method is needed to confirm the SEM results. Contrary to optical microscope and SEM images, AFM investigations allow deeper insight about lateral shape and surface morphology, because the lateral resolution is increased (routinely  $\lesssim 10$  nm) and the measured data additionally contains information about the topography of the surface. These advantages are balanced by the disadvantages that the scan speed and scan field are further reduced. Therefore it is obvious that scanning every flake or whole samples with AFM takes far too long.

The most interesting quantity is the height of the flakes that have been located by SEM. The layer thickness can be determined by AFM, however still for polished and carefully

cleaned  $\text{SiO}_2$  substrates the height of a monolayer graphene seems not to be a fixed value. From measurements of HOPG step heights for a graphene monolayer of  $\sim 3.4 \text{ \AA}$  would be expected. This value is independently determined by early **X-Ray Diffraction** (XRD) measurements [102–104] that already gave a precise view on the crystal structure of graphite. But for the case of an isolated graphene lying on a substrate the reported values are widely spread between the expected  $3.4 \text{ \AA}$  and  $10 \text{ \AA}$  [75, 105–107]. These deviations are not yet fully understood. Some groups claim that there is especially water underneath the carbon layer, others address a properly chosen working point in the force-distance curve to solve all the problems [107, 108] and references therein. But it must be additionally considered that both the different technique (AFM in contrast to XRD) and the different situation of isolated layers lying on an amorphous substrate in contrast to a regularly ordered crystal in case of graphene on HOPG may lead to deviation in the step heights. Keeping these difficulties in mind some pictures of graphene and FLG are exemplarily arranged in Figure 4.8. In the Figure 4.8 a) to c) graphene layers with a height less than  $\sim 1.6 \text{ nm}$  are shown. All three flakes are deposited on semiconducting substrate. The locating of the flakes was performed by SEM as described above. The substrate materials are GaAs a), GaMnAs b) and InGaAs c). In Figure 4.8 d) the substrate ( $\text{Si/SiO}_2$ ) was pre-patterned to get a larger periodicity ( $\sim 3.3 \mu\text{m}$ ). This flake is approximately  $5 \text{ nm}$  thick. Not only the relative big height of the half cylinders of approximately  $90 \text{ nm}$  but also all other surface textures are followed very closely from all graphene sheets investigated on the different substrates. This will be discussed in more detail in chapter 5.1. Additional difficulties in the correct interpretation of the AFM measurements are also visible in Figure 4.8, especially in image c). Small white dots are spread all over the image indicating very high spots. As shown later, these spots are resist residues. After a flake is located by SEM alignment marks are patterned with EBL and metal evaporation. These marks are used to relocate the flakes in the AFM or other methods. The resist residues are present due to the fact that the spinned PMMA can not be totally removed during lift-off even with additional cleaning. Therefore some small spikes are left on the surface. The density of the peaks (peaks per area) varies as clearly visible in Figure 4.8. In nearly every AFM image after a patterning step these peaks are detectable. These peaks further hamper the measurements of the graphene height since they are  $\sim 4 \text{ nm}$  high which is more than the doubled height of the desired flake thickness [109]. This adds an additional error to the measurements but the alignment marks patterning can not be avoided in the available AFM since the rough positioning system of the AFM allows only a positioning of  $\sim \pm 20 \mu\text{m}$ . A grid patterning before the graphene deposition as known from  $\text{SiO}_2$  substrates reduces the contrast in SEM and hence is not feasible, too.

### Micro-Raman

A reliable method to identify or prove the number of layers, especially for graphene ML and graphene bilayer (BL) is Raman spectroscopy. Inelastic scattering of monochromatic

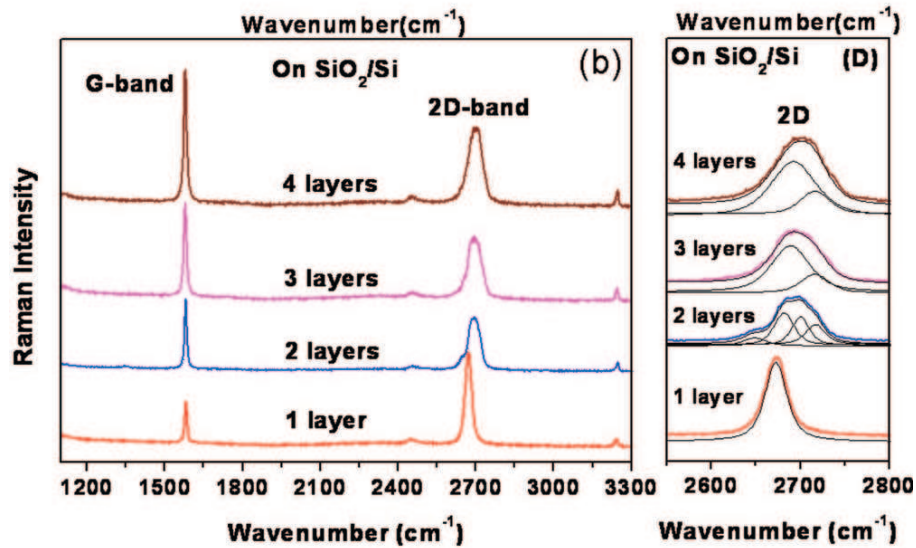


**Figure 4.9:** SEM image of a bilayer graphene on InGaAs that was confirmed by Raman.

light gives clearly distinguishable signatures for graphene ML, BL and FLG up to about 5 layers [5, 110]. Scaling down the spot size of the exciting light by optical means together with a movable stage allows the observation of frequency shifts in Raman signal with a high spatial resolution and leads to Micro-Raman images. The lateral resolution achieved by this technique is a few 100 nm.

As shown in Figure 4.10, Raman signals of a ML graphene sheet consists of G ( $\sim 1584 \text{ cm}^{-1}$ ) and D' ( $\sim 2700 \text{ cm}^{-1}$ ) line and eventually a D peak ( $\sim 1350 \text{ cm}^{-1}$ ) apparent for disturbed graphene, e.g. graphene with broken symmetry by edges or high a defect density. The number of layers can either be determined by the intensity of the G-line that increases with increasing number of layers or by the shift of the D' line and changes in the RMS, or equivalent with the number of Gaussians needed to fit the curve of the D' peak. Increasing the number of layers shifts the D' peak to higher energies [5, 45]. The Raman spectrum for a graphene monolayer and bilayer graphene taken from reference [110] is shown in 4.10 clarifying the above described characteristics. These features allow a detailed study of the properties of such small graphitic crystallites and have already been reported [45, 111]. But for graphene layers on semiconducting substrates the situation seems to be more complicated. While detection and characterization of mono- and few-layer graphene on top of GaAs substrates with Raman spectroscopy has already been demonstrated in ref-





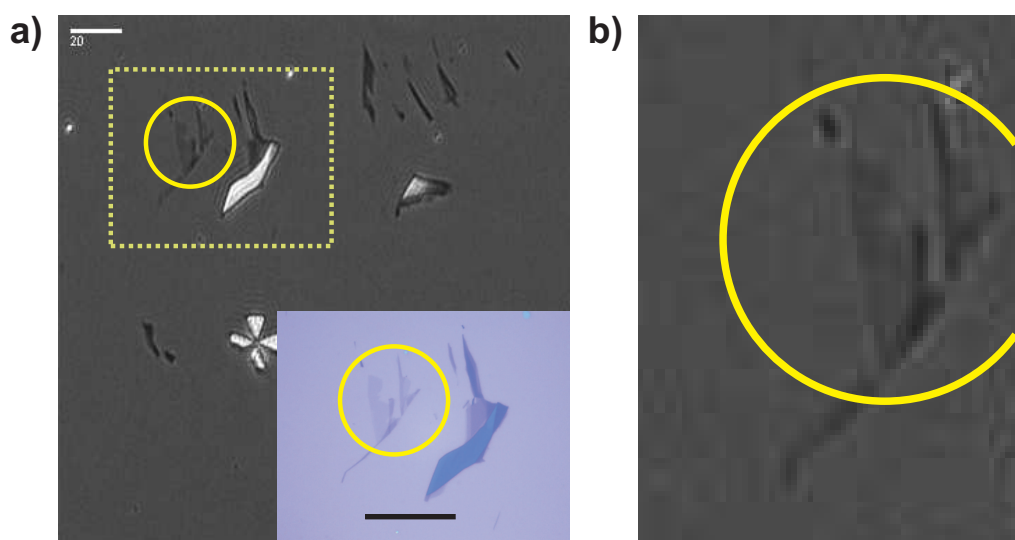
**Figure 4.10:** The Raman spectra of monolayer, bilayer, three layers, and four layers graphene on  $\text{SiO}_2$  (300nm)/Si substrate (left panel). The enlarged 2D-band regions with curve fit are shown in the right panel, taken from reference [110].

erences [27, 87], first attempts failed to confirm the number of layer on our GaAs substrate by measuring the Raman spectrum, since the signal was superimposed by photoluminescence of the substrate [112]. The measurements have been carried out by M. Hirmer in the group of Prof. C. Schüller. Despite difficulties, an interpretation of the Raman spectrum for one flake, shown in Figure 4.7, is tried identifying this flake as a graphene bilayer [112]. This problem could be even solved by doing confocal Raman spectroscopy, which would reduce the area under investigation and hence the signal from the underlying substrate. Otherwise the PL signal of the GaAs/AlGaAs substrate can be tailored by adapting the Al concentration and the layer sequence. This would allow to move the PL signal from the substrate away from the Raman shift generated from the graphene. However, this is in strong contrast to SEM and AFM investigations of the identical flake. Both prove the multi-layered structure of this graphene sheet. On InGaAs substrates the situation seems to be more promising. One flake showed a bilayer signature in the Raman spectra consistent with SEM images taken from this flake.

### Imaging Ellipsometry

Imaging ellipsometry (IE) on graphene is in an early state. Nevertheless we demonstrated successfully that detection of graphene on flat surfaces like  $\text{SiO}_2$  or GaAs and the determination of the optical constants of graphene is possible.

In Figure 4.11 a) a typical micrograph taken by the CCD camera of the IE is shown demon-

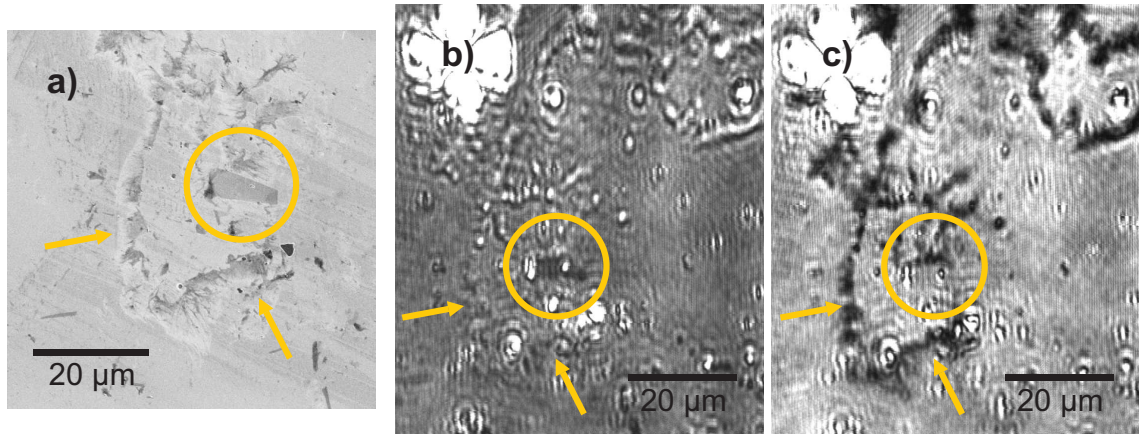


**Figure 4.11:** a) Imaging ellipsometry micrograph of flakes on  $\text{SiO}_2$  ranging from graphene to thin graphite. Inserted is the optical microscope image of the dashed area. Scale bars are both  $20\ \mu\text{m}$ . b) A zoomed view of the monolayer flake (marked in the images with circles) from a).

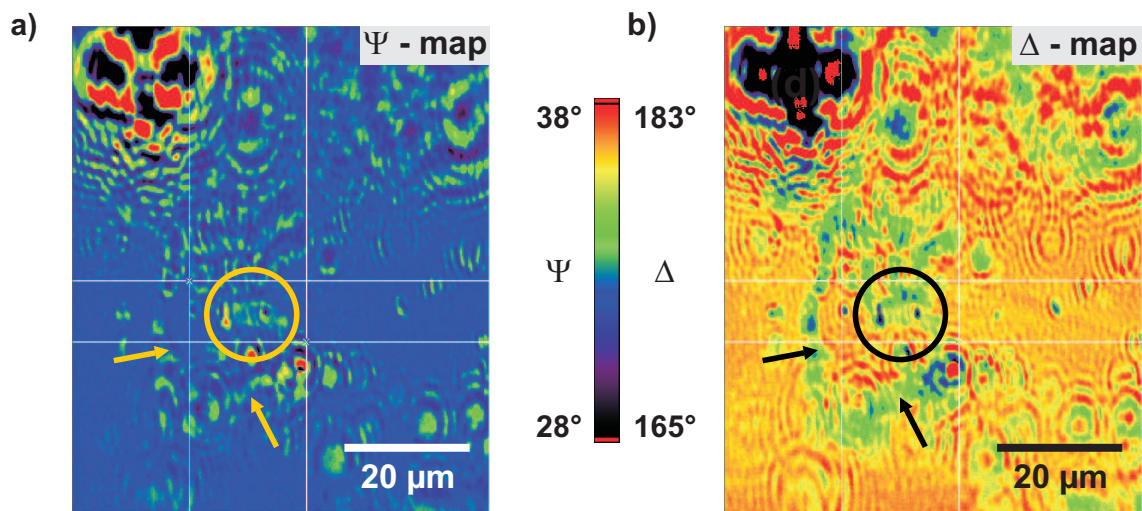
strating the possibility to distinguish between different flakes and areas with different number of layers. The inserted optical image of the dashed region shows that there are also areas covered with graphene monolayers. The optical contrast of this sample was also investigated in Figure 4.6, proving the number of layers. For clarity a higher magnification image of the relevant area is depicted in Figure 4.11 b).

Due to the fact that IE is a very sensitive technique for differences in surface properties, monolayer and thin graphite layers can be detected. Fortunately this seems not only limited to  $\text{SiO}_2$  substrates as verified in Figure 4.12 and Figure 4.13. There IE results of one area of graphene flakes on a GaAs substrate are collected. The circle is positioned around a FLG with a height of about 2 nm as determined by AFM. The arrows mark a "L"-shaped tape residue around the FLG. In the upper left part of the images an alignment mark is visible, except for the SEM micrograph in Figure 4.12 a) showing a smaller area of the sample. These SEM image already gives an impression of one difficult task: how to distinguish between graphene/FLG and possible residues or surface changes by peeling of the tape? The similar contrasts in SEM given by graphene and residues causes uncertainties in the correct classification of a contrast difference. IE overcomes these problems without any difficulty. This can clearly be seen in part b) and c) of Figure 4.12. These imaging ellipsometric micrographs are taken with different angles between polarizer/compensator, sample and analyzer, in detail in b) with an angle difference of  $12.936^\circ$  and in c) with difference of  $19.095^\circ$ . The analyzer is adjusted to  $32.920^\circ$  in b). In c) the analyzer orientation is  $30.326^\circ$ . This contrast inversion adjusts the images to be sensitive for the FLG in b) or contrarily for tape residues in c). The "L" shapes of the residues are strongly suppressed

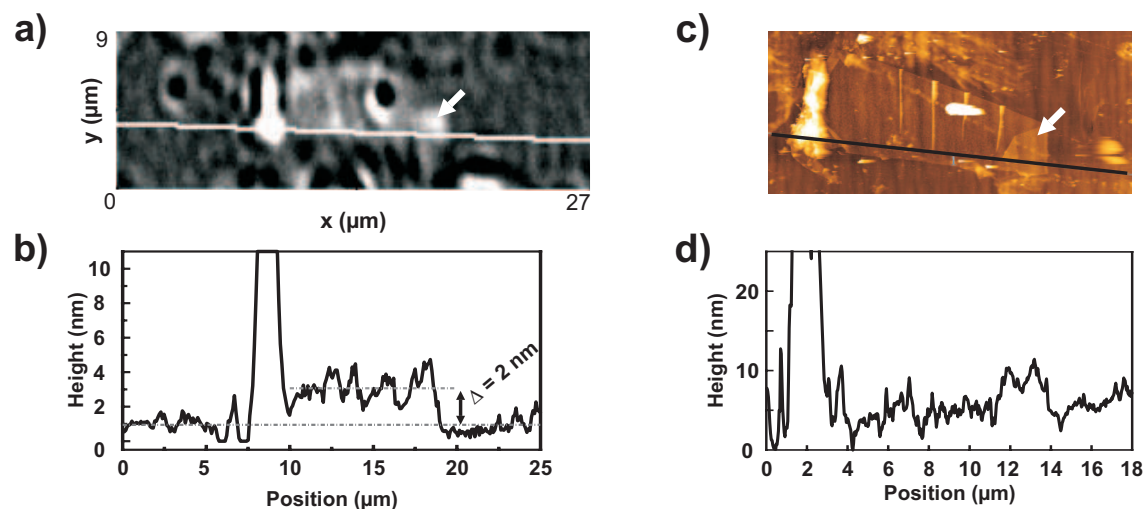




**Figure 4.12:** a) SEM image of a graphene flake on GaAs; b) IE picture optimized to show the flake, c) contrast inverted IE picture optimized for the background structures. The flake is marked with a circle, the arrows point towards some residues.



**Figure 4.13:**  $\Psi$ -map a) and  $\Delta$ -map b) of the FLG shown in 4.12 and the surrounding area; In the upper left corner a metal-evaporated cross for orientation is visible and leads to reflections. Circle and arrows mark FLG and the residues.  $\Psi$ -map shows FLG whereas  $\Delta$ -map does not, but shows instead the residues. Small elliptic disturbances due to residues from EBL-resist and graphene preparation. The small rectangulars in b) give the position of analyzed regions of interests.



**Figure 4.14:** a) converted  $\Psi$ -map into a thickness map of the flake shown in Figure 4.13; b) Line profile through the IE Image; c) AFM-Image; d) Line profile of the AFM-image. Folded region (arrows) of FLG is visible in both pictures.

in Figure 4.12 b), whereas the signal coming from graphene/FLG is well pronounced. By only rotating optical components of the setup the background structures became visible again and the graphitic flake becomes undetectable as demonstrated in Figure 4.12 c). It is worth to mention that even a small residue above the flake is resolved. This type of images are captured in real time by the CCD camera allowing a quick inspection of the sample surface.

Besides ellipsometric images also  $\Delta$  and  $\Psi$  maps can be captured (Figure 4.13 a) and b), respectively) again to get a possibility to distinguish between residues and graphitic layers. It seems that the  $\Psi$  map pronounces the flake in contrast to the residues and for the  $\Delta$  map the other way round. The circular like disturbances are originated from resist residues. One challenge using this technique is the interference fringes introduced especially from the reflecting metallic alignment marks or sample edges.

Since the InGaAs substrate has a rough surface it was only possible to visualize a thin graphite layer.

In addition to the simple detection of graphene a quick determination of the thickness is a big advantage of IE. By development of a model for the optical system, the  $\Delta$ - and  $\Psi$ -maps can easily converted to height-maps similar to the topographic images taken from AFM-measurements. For the model the refractive index  $n$  and the extinction  $k$  is needed. Their properties will be discussed in chapter 5.2 in more detail. In a first assumption they should be set to constant values, so that the thickness of the graphitic layer is the only free fitting parameter. Then the  $\Psi$ -map (Figure 4.13 a)) of a graphene sheet can be converted into a map of the topography as shown in Figure 4.14 a). In Figure 4.14 c) the identical flake is

mapped by AFM. The elevated bright regions on the left edge of the AFM image is caused by a residue comparable to the circular perturbations in the IE that can be ascribed to a particle laying on the flake. This particle is also visible in the SEM picture (Figure 4.12 a)). In Figure 4.14 b) and d) the height profiles along the drawn lines in a) and c) are plotted. In this way the height of the flake was determined to  $(2.0 \pm 0.6)$  nm with IE technique. This is in good agreement with AFM measurements performed on this flake which gives a height in the central region of about 2 nm.

### Transport

The last method that should be mentioned here are magnetotransport measurements of quantum Hall effect. As described in chapter 2.2.2, the quantum Hall effect is different for graphene ML and BL as demonstrated in Figure 2.7 d) and e). Therefrom measuring the QHE is a highly reliable method since the electronic properties of single and bilayer graphene are fundamentally different as has already been explained in chapter 2.2.2. Since this way is well described in literature [2, 6, 32, 89] and its background is well understood it should not be explained here in detail.

Graphene monolayers became famous for their so called half-integer quantum hall effect. Half-integer is used to distinguish it from the fractional quantum Hall effect. The plateaus sequence is spaced with integer steps of  $4e^2/h$  for both mono- and bilayer. In the case of a monolayer, the quantum Hall plateaus are multiples of  $(n + \frac{1}{2}) 4e^2/h$ . In contrast to that a bilayer exhibits the plateaus at integer multiples of  $\pm 4e^2/h$ . Additionally the zero plateau is missing in the bilayer case. Hence it is possible to distinguish between one or two layers from the position of the quantum hall plateaus. Even if this requires magnetotransport measurements and is therefore a rather ambitious approach and very time-consuming approach, it gives very reliable data.

## 4.3 Detection methods – an overview

A couple of ways for determination the number of layers were presented in this part of the thesis. At the end of the chapter the pros and cons of the different methods are summed up. The itemized experimental methods were:

- Optical microscopy
- Scanning electron microscopy
- Atomic force microscopy
- Micro-Raman

- Imaging Ellipsometry
- Magnetotransport

The most popular technique together with the highest performance is optical microscopy. It is a very fast technique and the number of layers can accurately be determined, if the substrate is suitable and at the same time this is the biggest disadvantage of this method. It is limited to Si/SiO<sub>2</sub> substrates with a certain thickness of the oxidized layer or to substrates with comparable optical properties [28].

The detection with SEM is also possible [109], even it is still necessary to apply a cross-check with another experiment. Actually, it is unclear if and how dramatic damages are introduced to the flakes [99, 100] by some carbon precipitation by SEM. SEM is more time consuming than optical microscopy but still faster than AFM. Since the layer thickness of single graphene layers seems to be quite different especially under ambient condition, even AFM does not provide a reliable proof of the number of layers. But for the semiconducting substrates even Micro-Raman measurements can fail as it has been shown. Difficulties here are the photoluminescence of the substrate and possible damage of the flake investigated with higher light intensities. But for further experiments the optical properties of the substrate could be tuned shifting the PL signal away, as already shown for the InGaAs substrate.

As another optical technique imaging ellipsometry was applied. The detection of graphene can be performed as fast as with optical microscopy. The limitation are that smooth surfaces are required. Additionally, IE allows to distinguish between graphene and tape residues within seconds. With a  $\Psi$  map and under some assumption a map of the topography can be created within minutes that gives similar results to AFM measurements. As a last method to distinguishing especially between monolayer and bilayer magnetotransport is listed. The difference between one and two layers is distinct. Since measurements of the quantum Hall effect are needed, a totally patterned graphene sample working at low temperatures is necessary to characterize the number of layer of a certain graphene flake. The preparatory work takes a couple of weeks for this method, if graphene on a semiconducting substrate is used.

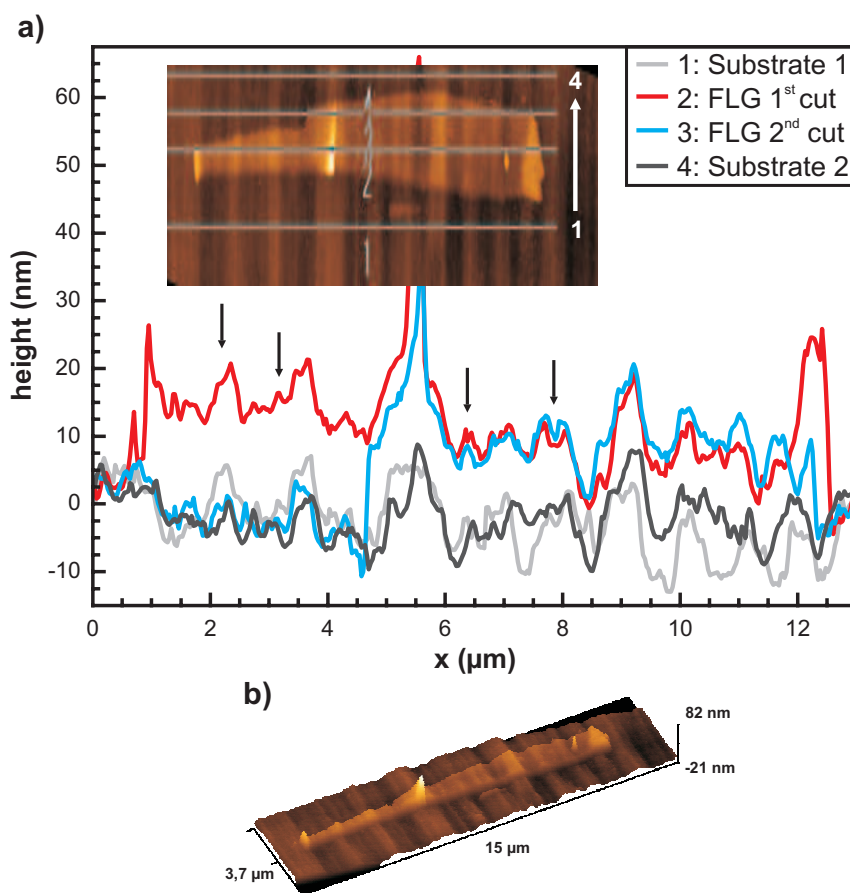
## Chapter 5

# Mechanical and optical properties

In the following chapter the mechanical properties deduced from the morphology of the graphene sheets after different treatment and the optical properties will be discussed. The mechanical properties directly follow from AFM investigations of the surfaces of pristine rough, flat and prepatterned substrates and the comparison of substrate and graphene after and before a lift-off process. The information about the flexibility and stiffness are more or less a coproduct of the efforts of detection and classification of the graphitic sheets as described in the previous chapter. Similarly the optical properties are a result of the successful attempt to utilize IE for detection and classification of graphene on various substrates. We were able to determine the dispersion relation of a graphene monolayer in the whole visible spectrum. We could extract both extinction and refraction and found that they depend stronger on the wavelength as it seems in literature [113]. This situation will be discussed at the end of this chapter.

### 5.1 Mechanical Properties

Graphene can be viewed as a crystal consisting of two surfaces without an interlayer. From this point of view it is no surprise that this material is very sensitive to its surrounding environment. Other interesting topics are the mechanical properties of a two dimensional sheet that could thermodynamically not be stable without support. Van der Waals interaction to the substrate surface stabilizes the graphene sheets. Fascinating mechanical properties such as stiffness and Young's modulus have already been studied with micro-mechanical resonators prepared of graphene as well as the usage of this light material as a very sensitive mass sensor [114–117]. But what about the flexibility and how closely do the intrinsic rippled sheets follow the (smallest and largest) curvatures of the underlying substrate materials? In this context another question arises about the origin of the ripples of graphene that seems to be intrinsic (to stabilize the crystal) and extrinsic due to some dirt between graphene and substrate or roughness of the substrate [25, 108, 118–120].



**Figure 5.1:** a) Line-cuts through substrate and a 14 nm thin graphite flake. The inset shows this flake. The y-axis is stretched by a factor 3. The peak at  $\sim 5 \mu\text{m}$  is due to some layers pointing upwards. Even thicker flakes are so flexible that they can follow unevenness of the substrate, marked for certain positions by black arrows. b) 3D view of the same flake also showing the identical topography between flake and substrate.

These corrugations can lead to local strain and hence to intrinsic fields inducing quantum coherence effects such as weak (anti) localization and universal conductance fluctuations due to **spin-orbit interaction** (SOI) [121–124]. Also the conductivity is strongly influenced by residues beneath substrate and graphene or on top of graphene, or by the corrugation. For this reasons extensive AFM investigations of graphene of various flat, rough and prepatterned substrate have been performed. The flexibility of layers with different thicknesses with respect to long periodicities and/or bigger amplitudes of the substrate surface has been observed. As already qualitatively shown in Figure 4.8, graphene sheets are very flexible and follow the substrate texture very closely. The  $\sim 1 \mu\text{m}$  periodicity of an InGaAs substrate shown in Figure 4.8 c) gives small trenches ( $\sim 15 \text{ nm}$  high) that are followed by this  $\sim 1.6 \text{ nm}$  thick flake on an InGaAs substrate. As known from the statement

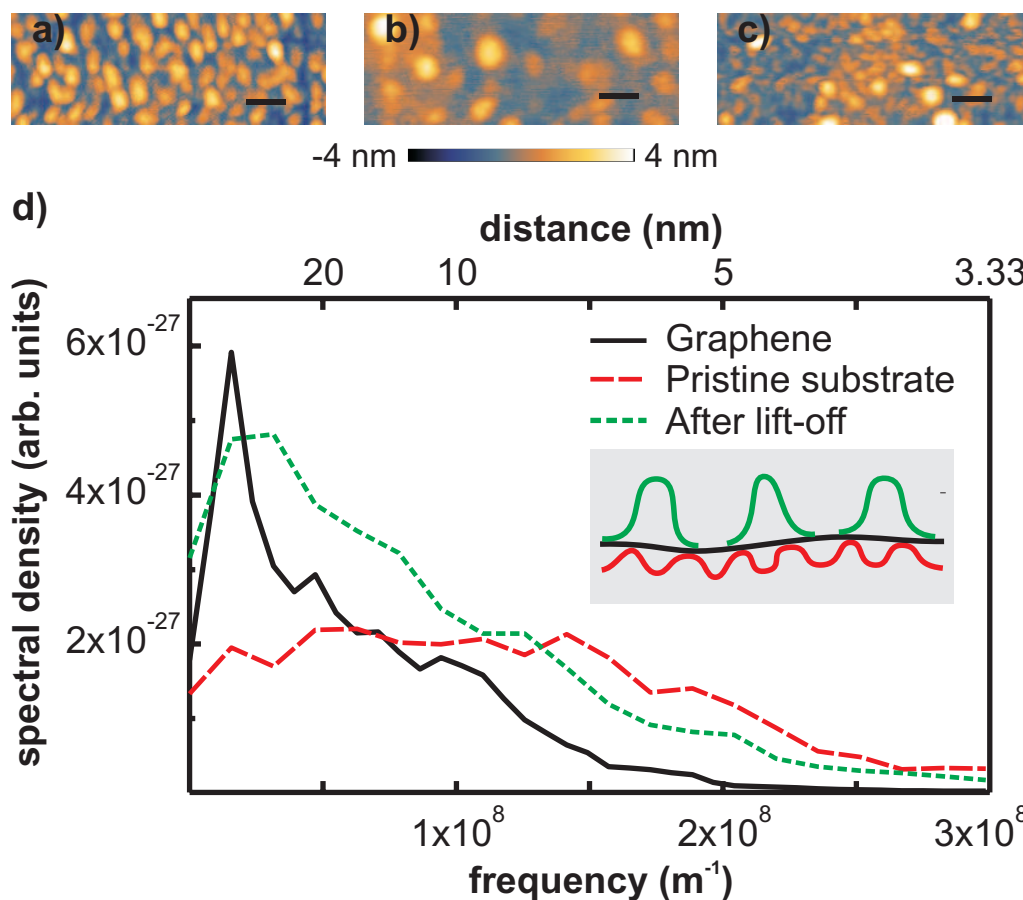
in chapter 4.2 the AFM step height is not suitable to count the exact number of layers of the flake, but it can be estimated between 2 and 4.

In Figure 4.8 d) an artificially modified SiO<sub>2</sub> substrate is used. The surface was prepatterned with half cylinders with a height of  $\sim 85$  nm and a distance of about 3  $\mu$ m and is exactly reproduced from an ultra thin graphite sheet with a thickness  $\leq$  than 5 nm. This finding demonstrates the high flexibility of graphene and ultra thin graphite sheets with a thicknesses  $\leq 5$  nm and varying number of layers ranging from 2 to 15 precisely following the curvature of larger structure.

To test the flexibility for thicker sheets, in Figure 5.1 the data taken on a 14 nm thick graphite flake on an InGaAs substrate are shown. The inserted image is stretched by a factor 3 for better visibility. The line scans through the flake (along the lines in the inset) show a quite accurate and detailed copy of the underlying substrate texture even for such a large number of graphene layers. Figure 5.1 b) is the unstretched 3D view of the same flake. This image shows as well the identical copy of the surface texture for such a large number of layers ( $> 40$  layers). This behavior is observed on all samples and all substrates with a graphite thickness of up to 40 nm even if the texture is smeared out as intuitively expected. Actually for more than 120 layers the influence of the substrates surface on this layer stack is great enough to create a bending in the out of plane direction.

To gain more insight into the flexibility of graphene sheets and the influence of the morphology of the substrates also on small length scales, detailed AFM scans of graphene flakes and of the corresponding substrates have been performed. To check for unwanted process residues on the substrates, also pristine substrates and substrates after an e-beam lithography step are compared. In Chapter 4.2 it was already introduced that the mechanical exfoliation technique with adhesive tape always leaves residues on the surface [125]. Therefore the areas outside the graphene flakes are not a proper reference. Instead, control samples have been treated with same lithographic processing, but without depositing graphene flakes. Typical AFM images are reproduced in Figure 5.2 a) to c). A high resolution AFM scan of a narrow region of the pristine substrate is depicted in Figure 5.2 a). The morphology of a graphene sheet (thickness  $\sim 1.3$  nm) on a GaAs substrate is displayed in Figure 5.2 b). In Figure 5.2 c) the surface morphology of a control sample without graphene after a standard lift-off process with PMMA is given. The roughness of the pristine substrate shown in Figure 5.2 a) does not appear in the image of the graphene flake in Figure 5.2 b). The flake seems to cover the fine texture originating from the substrate. But the inspection of the graphene surface displayed in Figure 5.2 b) reveals noticeable singular spots with a height of about 4 nm and a diameter of 30 nm. Similar spots appear on the reference samples after a lift-off process, but not on the pristine samples. Therefore, those spots seen on the graphene sample (Figure 5.2 b) ) must be PMMA residues, which lie on top of the graphene flakes, since the alignment markers are deposited after graphene preparation. A sketch of the situation is inserted in Figure





**Figure 5.2:** AFM-images of a) pristine undoped GaAs, b) graphene on GaAs, c) GaAs-substrate after lift-off. All scale bars 50 nm. d): power spectral density of AFM-images, the inset schematically drafts the situation. Graphene follows the bigger substrate texture but not the additional small structures. On top single PMMA residues are randomly positioned [109].

5.2 d). Those spots appear even though the PMMA was carefully removed in the lift-off procedure with warm acetone. A strong oxidizing agent or oxygen plasma are not suitable for more thorough cleaning since this could also damage the graphene flakes. Similar results (on SiO<sub>2</sub>-substrates) were reported in literature [108]. Since the substrates have an intrinsic surface roughness extending to high spatial frequencies, those can be used as a “test signal” to probe how closely the graphene flakes follow the underlying structure. Therefore a power spectral density analysis is done from the AFM images of graphene flakes and the underlying substrate, before and after lift-off processing. Each curve is the **Root Mean Square (RMS)** average of the radial 1D power spectral densities of the individual line scans of an AFM image. For the pristine and the resist covered surfaces the curves of several 400 × 200 nm<sup>2</sup> areas were averaged to reduce the variance in the data.



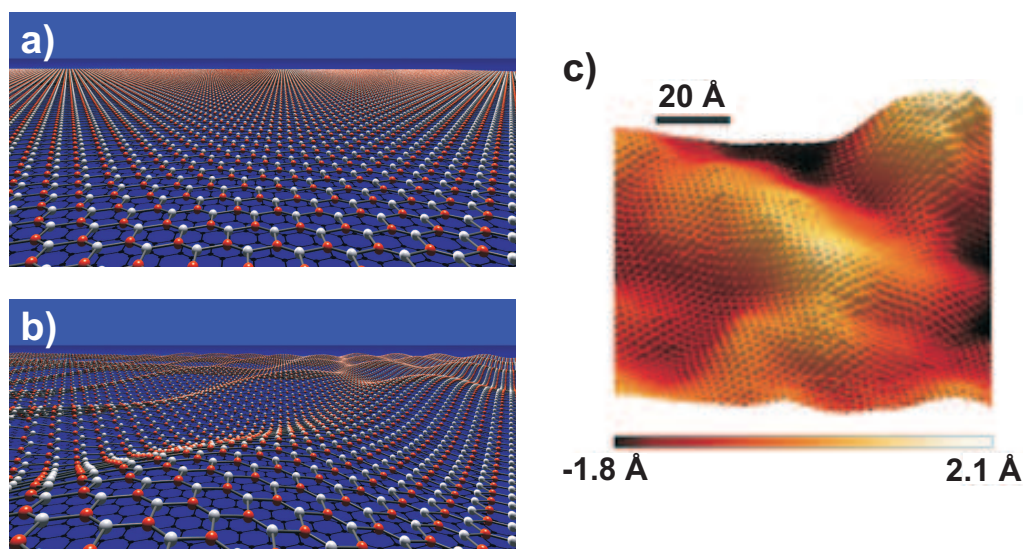
The graphene curve was determined from an  $800 \times 800 \text{ nm}^2$  image. The pristine GaAs surface has a rather flat spectrum up to  $1.6 \times 10^8 \text{ m}^{-1}$  which then gradually decays at higher spatial frequencies, presumably due to the limited lateral resolution of the AFM and the finite lateral size of the AFM tip. The graphene surface shows a similar spectral density at intermediate frequencies, but the decay occurs already at  $1.2 \times 10^8 \text{ m}^{-1}$  (corresponding to  $\sim 8 \text{ nm}$ ) and is somewhat more steep. This defines the cut-off frequency up to which the graphene follows the substrate corrugations. For higher frequencies the stiffness of graphene prevents the sheet from following the substrate in total [108]. The pronounced peak at low frequencies is found on the graphene samples and on the substrates after lift-off processing, but not on the untreated substrate, and hence can be attributed to the PMMA dots on top of the graphene.

These data and the fact that these spots can also be found on graphene on  $\text{SiO}_2$  after an EBL step (including a lift-off process), but not on graphene samples not coated with photoresist clearly reveals the existence of resist residues on the surface of graphene after the lift-off process. Another finding of these AFM investigations is the flexibility of graphene layers. The sheets can follow a continuous substrate texture from  $\sim 8 \text{ nm}$  to more than  $1 \mu\text{m}$ . Finally, AFM images and power spectral densities demonstrate that even with careful lift-off, an EBL step leaves unwanted PMMA residues on top of graphene as well as substrates.

### Discussion of mechanical properties

A very early result of theoretical physics was the thermodynamical instability of two dimensionals crystals by Landau and Peierls [73, 74] which was extended by Mermin [126]. Within this framework it was a surprise that two dimensional crystals can be experimentally realized [1, 127]. First of all it must be stated that the graphene layers are connected to a sustaining substrate. This probably leads to stabilization of the atomically thin flakes. A deeper insight of the behavior of suspended graphene layers was given by Transmission Electron Microscopy (TEM) [118, 119]. By analyzing the diffraction pattern the "rippled" structure of suspended graphene layers was first shown. These ripples create a quasi third dimensionality by a displacement of the atoms in an out of plane direction. This seems to be an intrinsic property of graphene flakes. In addition, the sustaining substrates also influence the microscopic topography of graphene. Both effects are demonstrated in Figure 5.3. The schemes show both a flat graphene sheet in Figure 5.3 a) and the rippled graphene sheet in Figure 5.3 b) similar to the findings of TEM investigations [118, 119]. In Figure 5.3 c) a stereoscopic STM-image of graphene's topography, taken from reference [128] is included to display the above described situation for graphene on substrates. The bigger surface modifications are introduced by the substrate, the small substructure are the resolved carbon atoms.

Especially the influence of the substrate's morphology on graphene layers has been confirmed and extended to larger structures within this thesis. The mechanical formations

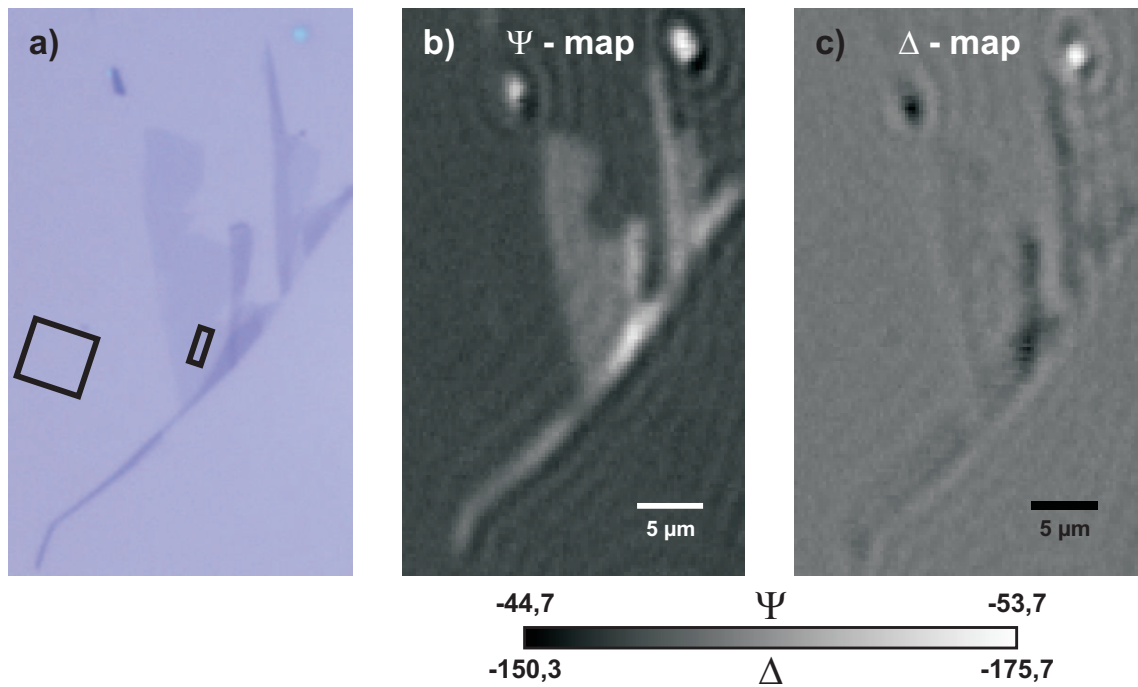


**Figure 5.3:** a) Schema of a flat graphene sheet and b) of a rippled graphene sheet imitating the situation for graphene found with TEM [118,119] c) Constant current STM topography of a graphene flake above a SiO<sub>2</sub> substrate. Corrugations with a lateral dimension of few nanometer and a vertical dimension of  $\sim 1.5$  Å are observed, introduced by the underlying substrate, taken from [128].

induced from the substrate into graphene is big and it is known that this bending of the sheet can be described as an additional potential [129]. This affects the scattering mechanism and therefore limits graphene's electronic properties [32]. Bending of graphene can also lead to strain in the sheet. Raman investigations of unstrained, strained and relaxed graphene reveal that graphene is very sensitive to tensile strain [130, 131].

Two conclusions can be deduced from this: First, if (electronic) properties of graphene are tried to be connected to graphene's morphology, the influence of the substrate and its morphology must carefully be checked. And the opposite direction: If influences from graphene's morphology should be avoided (e.g. reduce scattering or spin orbit interaction) a substrate is needed as flat as possible. AFM investigations for such a situation have recently been reported [106].

The impact of the number of layer on flexibility and stiffness of thin graphitic layers as demonstrated above, which is weak compared to most of the other solid state materials, can be explained analogue to a piece of paper positioned on a corrugated surface. For one or a few sheets, they will probably follow the surface. But if much more sheets are stacked on top of each other the finite thickness of the stack reduces the flexibility of the whole stack even for the lowest lying sheet. This analog is valid due to the fact that the graphene sheets are only weak coupled by van-der Waals forces comparable to the stacked sheets of paper. This enables a motion of the layers with respect to the neighboring layers which is needed for the observed low influence of the layer number on the flexibility of the whole stack.

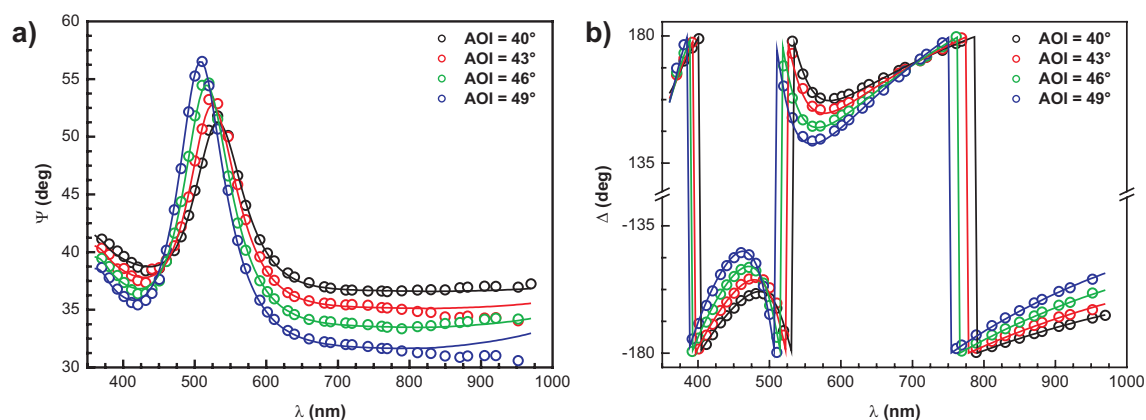


**Figure 5.4:** a) Optical image of a graphene monolayer on a SiO<sub>2</sub> substrate. The black rectangles shows exemplary two regions of interests for the investigations of the dispersion relation. b) The same area as  $\Psi$  and c) as  $\Delta$  map captured with IE.

## 5.2 Optical Properties

The development of the sample layout, measurements and investigations with imaging ellipsometry and the evaluation of the dispersion relation were carried out in close collaboration with *Accurion* Company in Göttingen. For determination of the optical properties, graphene on the standard SiO<sub>2</sub> substrate is used due to the possibility for characterization by optical microscopy and for comparison with results achieved by other groups and different techniques.

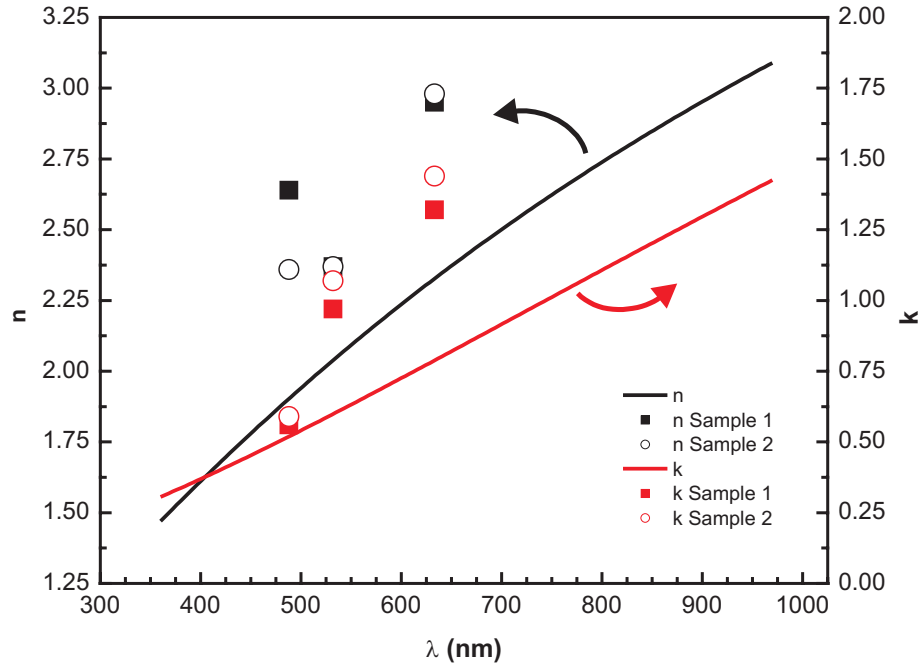
The starting point for the determination of the optical properties are the measured  $\Delta$  and  $\Psi$  maps that were already introduced in Chapter 4.2. The sample used here was carefully chosen and checked by optical microscopy and AFM for its monolayer nature. On this suitable flake first  $\Delta$  and  $\Psi$  maps are taken as shown in Figure 5.4 b) and c), the corresponding optical image is included in Figure 5.4 a). The disturbances visible as interference fringes especially in the  $\Delta$  map are mainly from the PMMA residue, also visible in optical image.



**Figure 5.5:** a)  $\Psi$  values and b)  $\Delta$  values of graphene for different wavelength at different angles of incident (AOI).

The  $\Psi$  map gives a better contrast of the carbon structure as the  $\Delta$  map and single and bilayer areas can be distinguished. The **Angle Of Incidence** (AOI) for these maps was 42°. Now the  $\Delta$  and  $\Psi$  values of different **Regions Of Interests** (ROI) are determined in dependence of the AOI and the used wavelength  $\lambda$ . The ROIs were chosen in such a way that several ROIs are representing graphene and separately the surrounding SiO<sub>2</sub> substrate, respectively. Exemplarily two such ROIs are shown in Figure 5.4 a). For all ROIs the spectroscopic data are measured, whereas the data for different ROIs within one kind of matter are consistent. Since the data are acquired with an optical setup that allows a resolution of  $\sim 1 \times 1 \mu\text{m}^2$  the values are already averaged over this area.

Finally, the  $\Delta$  and  $\Psi$  values for different wavelength and AOIs (Figure 5.5) are measured for these ROIs. The resulting plots are given in Figure 5.5 a) for the  $\Psi$  angle and in Figure 5.5 b) for the  $\Delta$  angle. The used AOIs ranged from 40° to 49° in 3° steps. A strong dependence on the used wavelength is observed for both quantities. The maximum value of  $\Psi$  and  $\Delta$  increases with increasing the AOI. The wavelength  $\lambda$  of the maximal value is shifted to shorter ones while increasing the AOI. Especially the wavelength range between  $\lambda \sim 400$  nm and  $\lambda \sim 600$  nm seems to give the biggest influence to  $\Delta$  and  $\Psi$  angles. With these data a further analysis can be done, leading to the optical dispersion of graphene. For this a model system is created, representing the three layers of the sample (graphene / 300 nm SiO<sub>2</sub> / Si). The way is the following: The expected  $\Delta$  and  $\Psi$  values for the model parameters (layer thicknesses, refraction index and extinction) are calculated and compared to the measured ones. Since the error between these values is too big, the parameters of the model are adjusted. In the ideal case the model system has exactly the same optical properties as the real sample and the parameters (e.g. the refraction index and extinction) of the model system are taken as the corresponding parameters of the sample. The way of calculating a dispersion relation from the IE data can be found in reference [70].



**Figure 5.6:** Dispersion relation of graphene on  $\text{SiO}_2$  substrate. The refractive index axis  $n$  is the left one and the extinction coefficient  $k$  one the right axis. The lines are fits of our measured  $\Delta$  and  $\Psi$  values to a Drude model. The scatter data are two samples from reference [113]. All data show a strong dispersion in the visible range, where the value of both the index of refraction and the extinction gets smaller for shorter wavelength.

During modeling it turned out that a careful adaption of the actual  $\text{SiO}_2$  thickness is necessary. Indeed, the variation of the oxide thickness is less than 1% ( $302 \pm 0.4$  nm instead of nominal 300 nm) but since IE is a very sensitive technique all parameters of the sample must be determined with high accuracy. For this purpose ROIs on the bare substrate have been used (the left rectangle in Figure 5.4 a)). With the adjusted oxide thickness and together with the thickness of the flake determined by AFM to about 0.7 nm calculations are done by using a Drude model [132]. The calculations have been performed at *Accurion* company using their IE software EP4\_model.

The resulting dispersion relation is shown in Figure 5.6. Both, the index of refraction  $n$  and the extinction coefficient  $k$  strongly depend on the applied wavelength and decrease with decreasing the wavelength  $\lambda$ .

### Discussion of optical properties

The interpretation of the dispersion relation shown in Figure 5.6 is in an early stage. The scattered data in Figure 5.6 are taken from reference [113] and correspond to the dispersion values for two samples at three wavelengths ( $\lambda = 488$  nm, 532 nm and 633 nm)

measured with picometrology. Since this method requires a laser light source only these three values are accessible and to the best of our knowledge no other experimental data on the dispersion relation exist. The strong dispersion is visible in our data as well as in the data of Wang et al [113]. They found that the dispersion is five times greater for both the real part and imaginary part compared to bulk graphite. The authors of reference [113] claim that this strong dispersion is likely caused by the strongly modified quantum level structure of one atom layer compared to graphite. The refractive index  $n$  resulting from IE seems to have a similar wavelength dependence as the picometrology ones. However the extinction seems not to be as strongly wavelength dependent as in the case of reference [113]. The origin of this is actually unclear. Another problem might be the description of a single atomic layer with a refraction index. Instead of that a description in terms of optical conductivity might help to avoid errors in the definition of refraction indices [133].

## Chapter 6

# Electronic Properties

Originally, the aim of this project was to study the influence of the substrate on the transport properties of graphene. However, to be able to perform electrical measurements of graphene on the crystalline GaAs based substrate we had to overcome difficulties mainly with the detection and classification of the graphitic sheets on these non SiO<sub>2</sub> substrates. During the successful, but time consuming path to develop appropriate methods for detection, interesting results about mechanical and optical properties of graphene have been found apart the main route. So much the better that we are able to conclude with this chapter the part of results in this thesis. It combines temperature and gate-voltage dependent transport and magnetotransport measurements on **mono-layer graphene** (MLG), **bi-layer graphene** (BLG) and **few-layer graphene** (FLG) sheets on GaA, InGaAs and SiO<sub>2</sub> substrates. Besides temperature dependent measurements of the intrinsic sheet resistivity and the conductivity around the charge neutrality point, signatures of quantized transport in the longitudinal and Hall resistance will be presented. Additionally, phase coherent transport phenomena such as weak localization (WL) and universal conductance fluctuations (UCFs) were intensely studied in dependence of temperature and gate voltage, and compared with the signals taken from graphene on SiO<sub>2</sub>. Finally, significant inelastic and elastic coherence lengths are extracted from the data. For comprehensive series of measurements and/or for repeating them, the aging process of the graphitic flakes will also be addressed. During this thesis more than 30 graphene samples on GaAs and InGaAs and a few on SiO<sub>2</sub> substrates have been prepared and investigated by means of electrical measurements. For clarity, we refer to the measured effects using the examples of the most prominent samples including mono- and bilayer graphene sheets. Most of the measurements have been carried out on graphene on GaAs.

## 6.1 Transport behavior

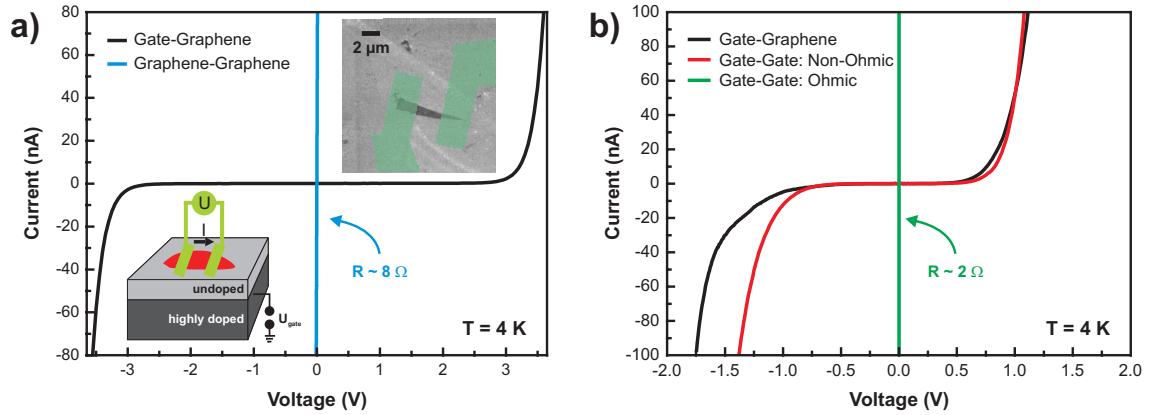
To avoid misinterpretations of the electrical measurements it is indispensable to have accurate knowledge about the characteristic of the contacts to graphene, the gate contact and about the dielectric layer. It is necessary to have ohmic behavior of the metallic contacts to graphene and gate and to know the voltage range which can be applied over the dielectric layer between gate-electrode and graphitic sample without significant leakage current. Thus, this chapter starts with this issue. We want to remark that all samples investigated by electrical measurements are collected, briefly described and the related flakes and contact geometry is displayed in Appendix C.

### 6.1.1 Contact and gate characteristics

In Figure 6.1 a) and b) I-V characteristics taken for different current paths in the transistor like device are shown. For clarity the lower left inset sketches the configuration. In the simplest case there are two metallic contacts (green) to a graphene flake on top of a substrate. The scheme also shows one contact to the highly doped part of the substrate used as backgate electrode. The two graphene contacts are also shown in the upper right inset what consists of a SEM image of a flake overlaid with two metallic strips.

In Figure 6.1 a) the I-V trace (cyan line) between two metallic contacts to graphene is depicted demonstrating linear and therefore ohmic behavior. We found that the contact resistance can be lowered to less than 1 k $\Omega$  for Pd contacts compared to those made with Ti/Au. Therefore Pd is mostly used for the contacts to graphene. Because of the formation of a Schottky barrier between metals and doped semiconductors [46], the preparation of ohmic contacts to the gate is more challenging. As shown in 6.1 b) (red trace), a diode like I-V characteristic results for not annealed contacts independent if they are soldered with In, glued with conducting silver-past or evaporated metals. Metal evaporation and heat treatment as described in detail in Appendix B for the different substrate materials leads to nice ohmic contacts to the highly doped semiconducting layer as demonstrated in 6.1 b) (green line). The dielectric layer in the case of the semiconducting substrate was an undoped semi-insulating GaAs/AlGaAs or InGaAs/InAlAs layer stack. Despite larger layer thicknesses, these dielectric layers have a rather low breakthrough voltage of only a few volts (typically  $\pm 3 - 6$  V) compared e.g. to SiO<sub>2</sub> substrates where more than 100 V can be applied. This is surprising, since GaAs and its ternary compounds have a higher permittivity as silicon dioxide. This low breakthrough voltages may be caused by the formation of deep traps and oval defects during the MBE growth [134–136]. The I-V characteristics of the dielectric layer of a GaAs substrate is shown in Figure 6.1 a) and b) as black traces. The diode-like trace shows an insulating behavior (current flowing  $\leq 1$  nA) within a few volts. If the applied voltage is too high, a significant current is flowing indicating the breakthrough of the substrate.



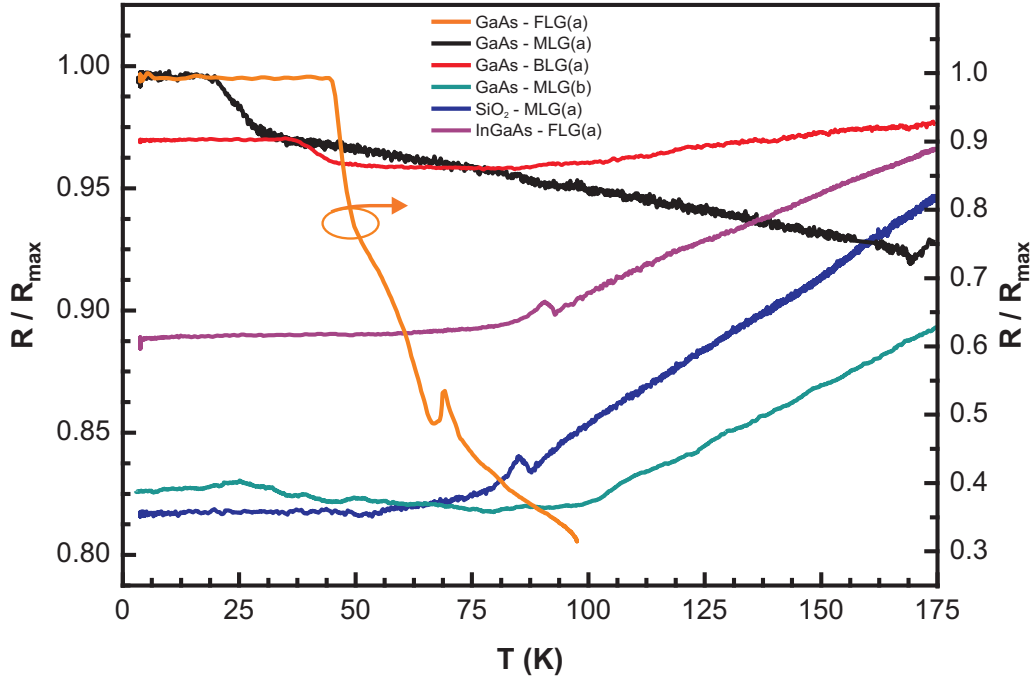


**Figure 6.1:** I-V traces for different samples and different current paths. a) Sample with improved (ohmic) gate contacts. The graphene-graphene I-V characteristics results in an ohmic resistance with  $R \sim 8 \Omega$ . The insulating voltage range over the dielectric layer is about  $\sim \pm 3V$ . Inserted is both a SEM image of the flake with overlaid contacts (upper inset) and a schematic drawing of the principal setup. b) I-V-traces with not optimized contacts to the highly doped backgate (black and red trace) in comparison with optimized gate contacts (green trace).

### 6.1.2 Temperature dependent intrinsic conductivity

The temperature dependent resistance of a couple of graphene samples with number of layers ranging from mono- to few layer flakes deposited on GaAs, InGaAs and  $\text{SiO}_2$  are collected in Figure 6.2. The cooling-down curves are measured in a two-terminal geometry by slowly cooling down the samples without magnetic or electric field from room temperature to 4.2 K. For better comparison of the different samples, the resistance  $R(T)$  is normalized to the maximum value of the resistance  $R_{max}$ . For most of the samples independent from substrate materials and number of layers, the resistance decreases with decreasing temperature until a saturation is reached between 100 K and 75 K. This behavior demonstrates metallic behavior and existence of a large amount of intrinsic charge carriers in these samples. The nearly linear  $T$ -dependence down to the saturation temperature together with the magnitude of the resistance change strongly points towards scattering between charge carriers and longitudinal acoustic (LA) phonons in graphene limiting the charge carrier mobility [22]. Note that the minor increase of the resistance after saturation seen for GaAs-BLG(a) (red trace) and GaAs-MLG(a) (black trace) seems to be induced by strong electron-electron interaction as will be discussed later. Saturation of the resistivity for temperatures below  $\approx 75$  K indicates the onset of another scattering mechanism that may be induced by the substrate. Similar behavior was reported, e.g. for FLG on  $\text{Pb}(\text{Zr}_{0.2}\text{Ti}_{0.8})\text{O}_3$  (PZT) and FLG/MLG on  $\text{SiO}_2$  [22].

Contrary, for some graphene samples on GaAs a increasing resistance with decreasing temperature and a saturation at reduced temperature between 30 K and 45 K was observed as depicted in Figure 6.2 for GaAs-FLG(a) (orange trace) and GaAs-MLG(a) (black

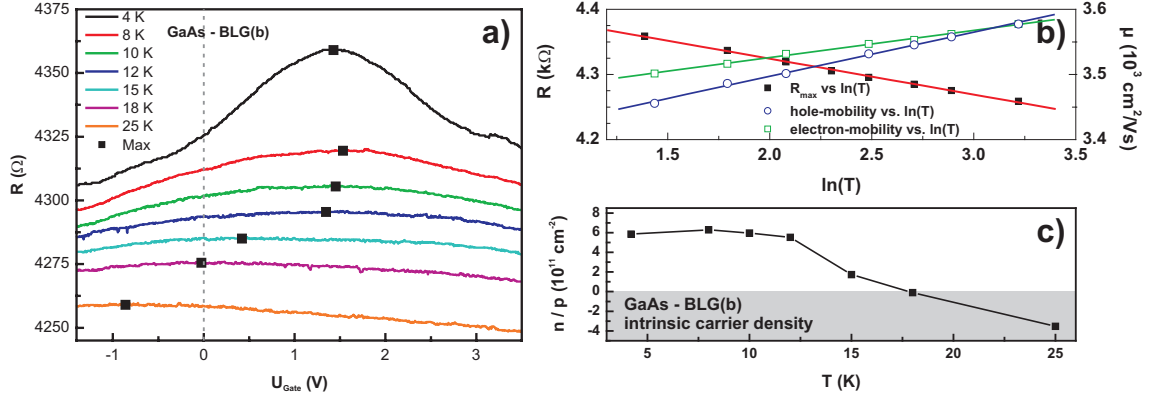


**Figure 6.2:** Cooling down curves of graphene on different substrate materials. The values are normalized to the maximum value within the measurement.

trace). This experimental finding points towards low intrinsic charge carrier density near the charge neutrality point (CNP) of the graphene flakes, high amount of electron-hole puddles or further interaction mechanisms leading to enhanced scattering of the charge carriers. However, on these two graphene samples no signatures for a CNP was found in the available gate voltage range, what seems to exclude a low intrinsic doping density to be the reason for the increasing sheet resistivity with decreasing temperature. The origin of this behavior and the appearance of a small local maximum in some samples, independent from positive or negative slope, is unclear up to now.

### 6.1.3 Charge neutrality point

As direct consequence of the specific band structure of graphene, the Fermi energy  $E_F$  can be shifted almost continuously by applying an electric field perpendicular to the sheet. Consequently, polarity and density of the charge carriers can accurately be tuned by putting the backgate electrode on a distinct potential. The position of the CNP, which can be determined by a maximum in the sheet resistance, relative to the applied gate voltage identifies polarity and density of intrinsic doping in the graphitic flakes. Due to lattice defects, doping, adsorbates, strain or influence of the underlying substrate the graphene sheets can intrinsically be doped [2]. In Figure 6.3 a) gate dependent sheet resistance of



**Figure 6.3:** a) Temperature dependence of the CNP of a BLG on GaAs. b) Resistance value  $R_{max}$  (black) of the CNP and hole-mobility (green) and electron-mobility (blue) as function of  $\ln(T)$ . c) Temperature dependence of the intrinsic charge carrier density and polarity. Negative values (grey region) denote electrons, positive values holes.

a bilayer graphene flake deposited on GaAs (GaAs-BLG(b)) is plotted at different temperatures. The observed positions and resistance values of the CNPs are marked with black squares. It is clearly visible that shape and position of the CNP changes with temperature. At  $T = 4$  K the resistance maximum is detectable at  $R \approx 4.6$   $k\Omega$  and  $V_{CNP} \approx 1.5$  V demonstrating a small shift of the CNP to positive gate voltage  $V_{Gate}$  in correspondence to a low intrinsic hole doping. The gray dash-dotted line marks  $V_{Gate} = 0$  V and is therefore related to the intrinsic carrier density. The intrinsic carrier density is calculated with  $n, p = \alpha_{GaAs} \cdot V_{Gate,eff}$ , where  $\alpha_{GaAs} = 4.1 \cdot 10^{11} \text{ cm}^{-2}/\text{V}$  is the charge injection parameter determined from Hall measurements as shown later and  $V_{Gate,eff}$  is the corrected gate voltage  $V_{Gate} - V_{CNP}$ . As clearly visible in Figure 6.3 c) a crossover of the CNP from positive to negative gate voltages can be observed suggesting a temperature dependent variation of density and polarity of the intrinsic carriers. The position of the CNP seems to be constant for  $T < 12$  K and the graphene is nominally undoped at about  $T = 18$  K. For  $T > 18$  K electrons become the dominant kind of charge carriers. Furthermore, the gate voltage dependent resistance maximum is broadened and the resistance value reduced for increasing temperature. This behavior may be connected to temperature dependent changes of the interlayer coupling, to a modified influence of the dielectric GaAs substrate, e.g. freezing out of traps in the GaAs layer or changed screening and/or to the formation of more or larger electron-hole puddles [137]. From the linear dependence of the sheet conductance  $\sigma_0$  on the carrier density and by using the charge injection parameter  $\alpha$ , the hole and electron mobility  $\mu$  was determined from the CNP measurements:

$$\sigma_0 = en\mu = e \frac{\epsilon_r \epsilon_0}{de} \cdot U_{Gate} \cdot \mu = \frac{U_{Gate}}{\alpha e} \mu \Rightarrow \mu = \frac{\partial \sigma_0}{\partial U_{Gate}} \cdot \frac{1}{\alpha \cdot e} \quad (6.1)$$

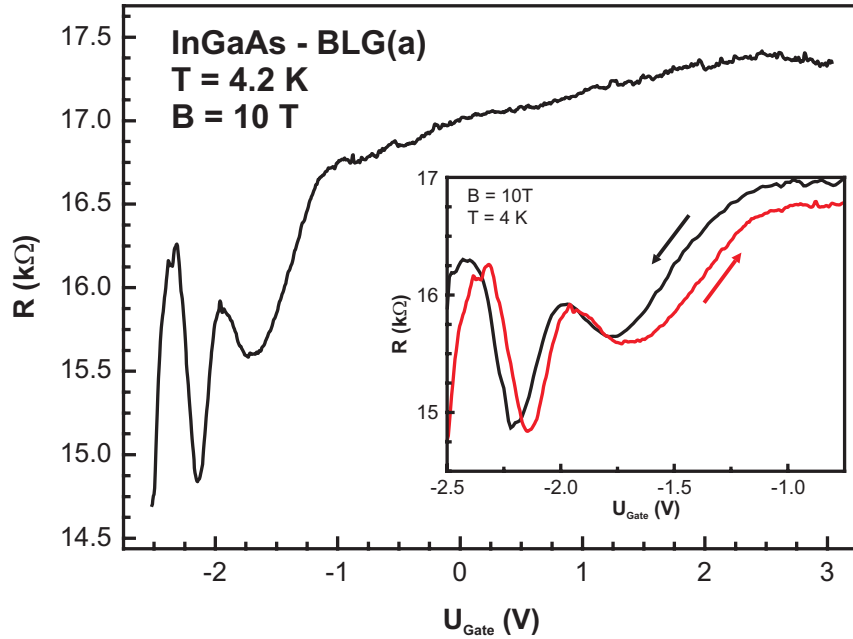
Where  $n$  denotes the charge carrier density,  $\epsilon_0$  and  $\epsilon_r$ , the permittivity of free space and the dielectric material, respectively,  $\alpha$  the charge injection parameter and  $e$  the unit charge. In the observed temperature range from 4.2 K to 25 K the electron-mobility constitute between  $3500 \text{ cm}^2/\text{Vs} \leq \mu_e \leq 3580 \text{ cm}^2/\text{Vs}$  and the hole-mobility is marginally lower between  $3456 \text{ cm}^2/\text{Vs} \leq \mu_p \leq 3580 \text{ cm}^2/\text{Vs}$ , respectively. The mobility is for both kind of charge carriers in the investigated region minor temperature dependent, albeit the mobilities are just as  $R_{max}$  linear with  $\ln(T)$ . The absolute values for the mobilities are in the range found in our group for graphene on  $\text{SiO}_2$  made from natural graphite and without a further annealing step [138]. The measured shift of the CNP to positive voltages at  $T = 4.2 \text{ K}$  has been detected for all investigated graphene mono-, bi- and few-layer samples on GaAs-based and InGaAs substrates, a temperature dependence of the CNP shift, however, was not detectable for more samples so far. Contrary, for graphene on  $\text{SiO}_2$  investigated at  $T = 4.2 \text{ K}$  a shift of the CNP is visible for both negative and positive gate voltages.

In Figure 6.3 b) the maximum resistance values are plotted against  $\ln(T)$  (black squares). A clear trend is observable that the resistance values decrease linearly with the logarithm of the temperature as indicated by the red line in Figure 6.3 b). To the best of our knowledge neither temperature dependent shift of the CNP nor a linearly decrease of  $R_{max}$  with  $\ln(T)$  is reported in literature for CNP measurements of graphene on amorphous  $\text{SiO}_2$  or on any other substrate. This may possibly be caused by the influence of the crystalline substrate materials and hence from interaction of the charge carriers in graphene with phonons, intrinsic field or dopants in the underlying semiconductor. A change of the intrinsic doping was theoretically predicted only for graphene on the nonpolar surface of (110)-GaAs not for the polar surface of (001)-GaAs [85].

## 6.2 Magnetotransport behavior

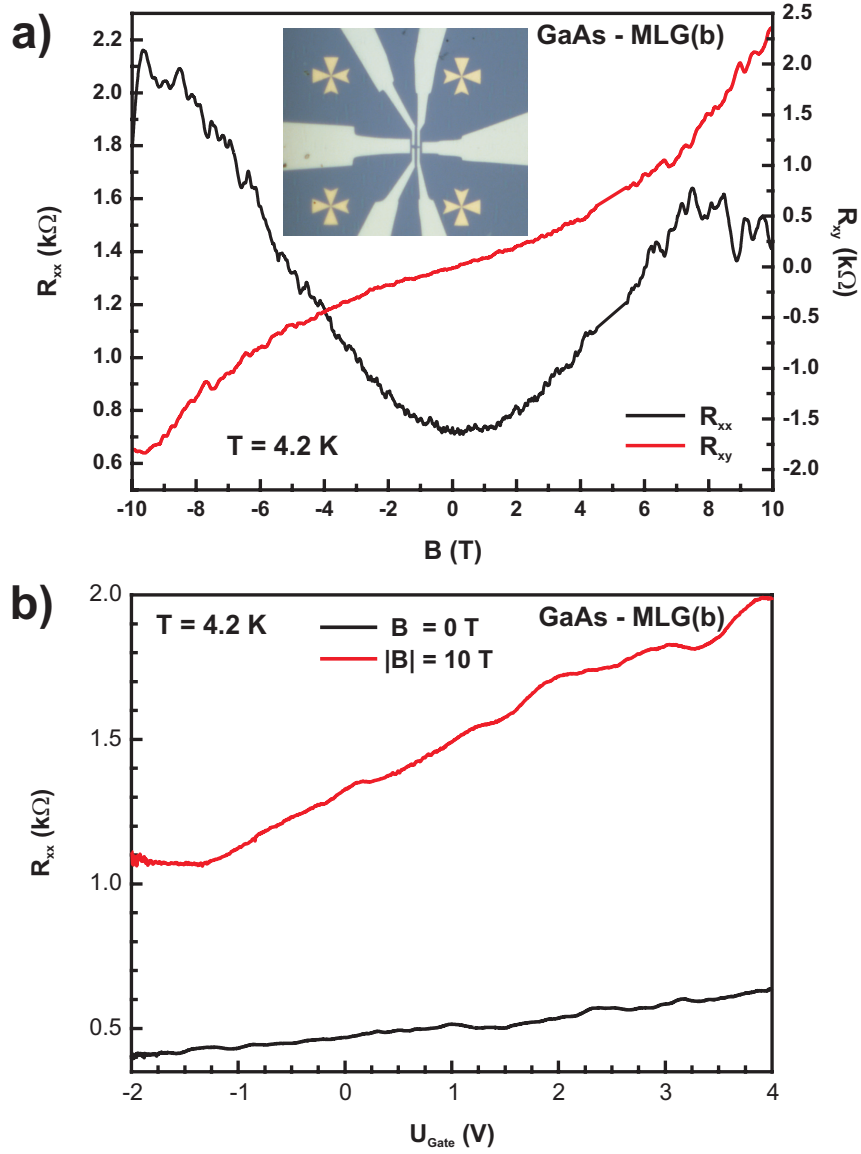
The magnetotransport properties of graphene on GaAs and InGaAs are demonstrated on examples of a mono- and bilayer graphene sample on GaAs and a bilayer sample on InGaAs. Both field sweeps of a perpendicularly applied magnetic field at constant gate voltage and gate voltage sweeps at a finite applied magnetic field have been carried out. Temperature dependent magnetotransport measurements, accurate analysis of the data and possible explanations will be presented in the following.

From measurements of the longitudinal  $R_{xx}$  and Hall resistance  $R_{xy}$ , information about quality, mobility and carrier density of the investigated sample can be achieved. In Figure 6.4 the two-terminal resistance  $R_{xx}$  as a function of the backgate voltage measured at  $T = 4.2 \text{ K}$  and with an applied magnetic field of  $B = 10 \text{ T}$  for the graphene bilayer (InGaAs-BLG(a)) on InGaAs is displayed. The number of layers in this case has been confirmed by Raman spectroscopy [112]. As demonstrated in inset of Figure 6.4, for both sweep directions starting from -1 V to -2.5 V (black trace) and back from -2.5 V to -1 V (red



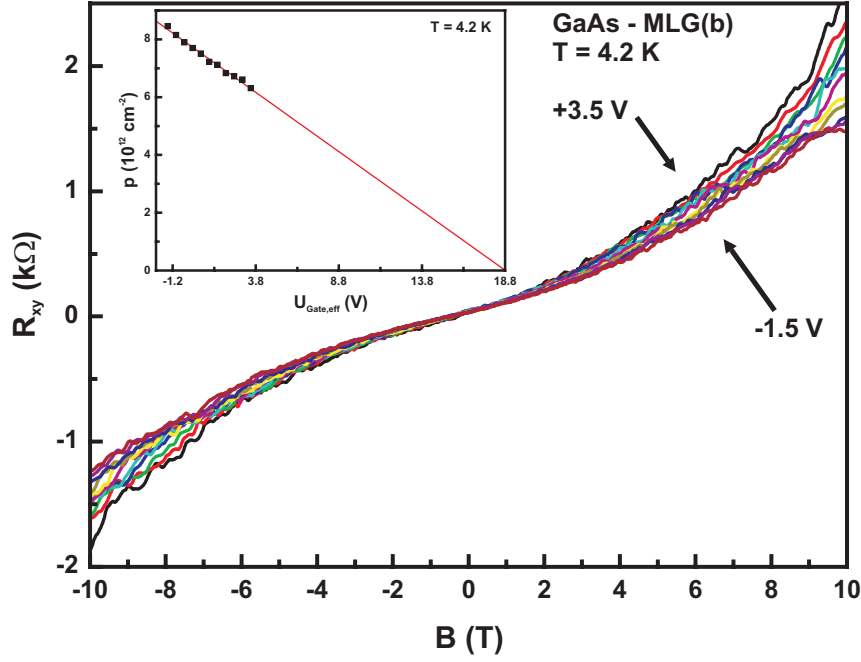
**Figure 6.4:** Gate dependent resistance for bilayer graphene on InGaAs substrate (InGaAs-BLG(a)). At  $B = 10$  T SdHs are observable. The inset shows up and down sweep of the gate voltage in the negative region. Besides a small offset the signals proof themselves.

trace) Shubnikov de-Haas (SdH) oscillations are clearly visible. This substantiates the two-dimensional nature of the charge carriers and the high quality with rather high charge carrier mobility of the two-dimensional graphitic crystal. The small offset between these two traces may be caused by changes of the electrical field at a certain voltage between down and up sweep due to (de-)charging of deep traps and misfit dislocations in the metamorphic grown buffer for strain relaxation [88], which is also part of the dielectric layer. Since the distinct SdH oscillations are monitored for low negative bias voltages in the hole transport region, the type of intrinsic charge carriers for this BLG on InGaAs seems again to be holes, as found for all other graphitic flakes on GaAs or InGaAs substrates. The reason for the resistance behavior around zero gate voltage and for positive gate voltages is still unclear. The signal becomes noisy and no further (distinct) oscillations are detectable as visible in Figure 6.4. One may speculate, that measurements in two terminal geometry are influenced by polarity of the charge carriers relative to the current path and polarity of the magnetic field [98], that the lower Landau levels (first and second) are broadened by disorder and can not be resolved or that the dielectric material or the gate contact is damaged. One or a combination of these possibilities could explain the observed behavior. After these sweeps, the gate-gate contacts became diode-like, even though they were almost ohmic before these measurements. Due to that, no further measurements on this BLG were feasible.



**Figure 6.5:** Magnetic field and gate voltage dependence of a graphene monolayer on GaAs (GaAs-MLG(b)) at  $T = 4.2$  K. a) Four-terminal longitudinal magnetoresistance  $R_{xx}$  (black) and Hall-resistance  $R_{xy}$  for  $U_{Gate} = 0$  V, an optical image of the device is inserted. b) Gate sweeps at  $B = 0$  T (black) and  $B = -10$  T. The resistance increases with increasing the voltage, but neither clear Shubnikov-de Haas oscillation nor clear quantum Hall plateaus are observable.

The magnetotransport properties with both, magnetic field a) and gate voltage sweep b) at  $T = +4.2$  K measured in a multi-terminal geometry on a MLG sample (GaAs-MLG(b)) on GaAs are shown in Figure 6.5. The intrinsic longitudinal resistance  $R_{xx}$ , without ap-



**Figure 6.6:** Gate voltage dependence of a graphene monolayer on GaAs (GaAs-MLG(b)) at  $T = 4.2$  K. a) Gate-voltage dependence of  $R_{xy}$  for applied voltages between 3.5 V and -1.5 V (Same sample as in Figure 6.5). Inset: Carrier density extracted from Hall measurements in a) as a function of the effective gate voltage.

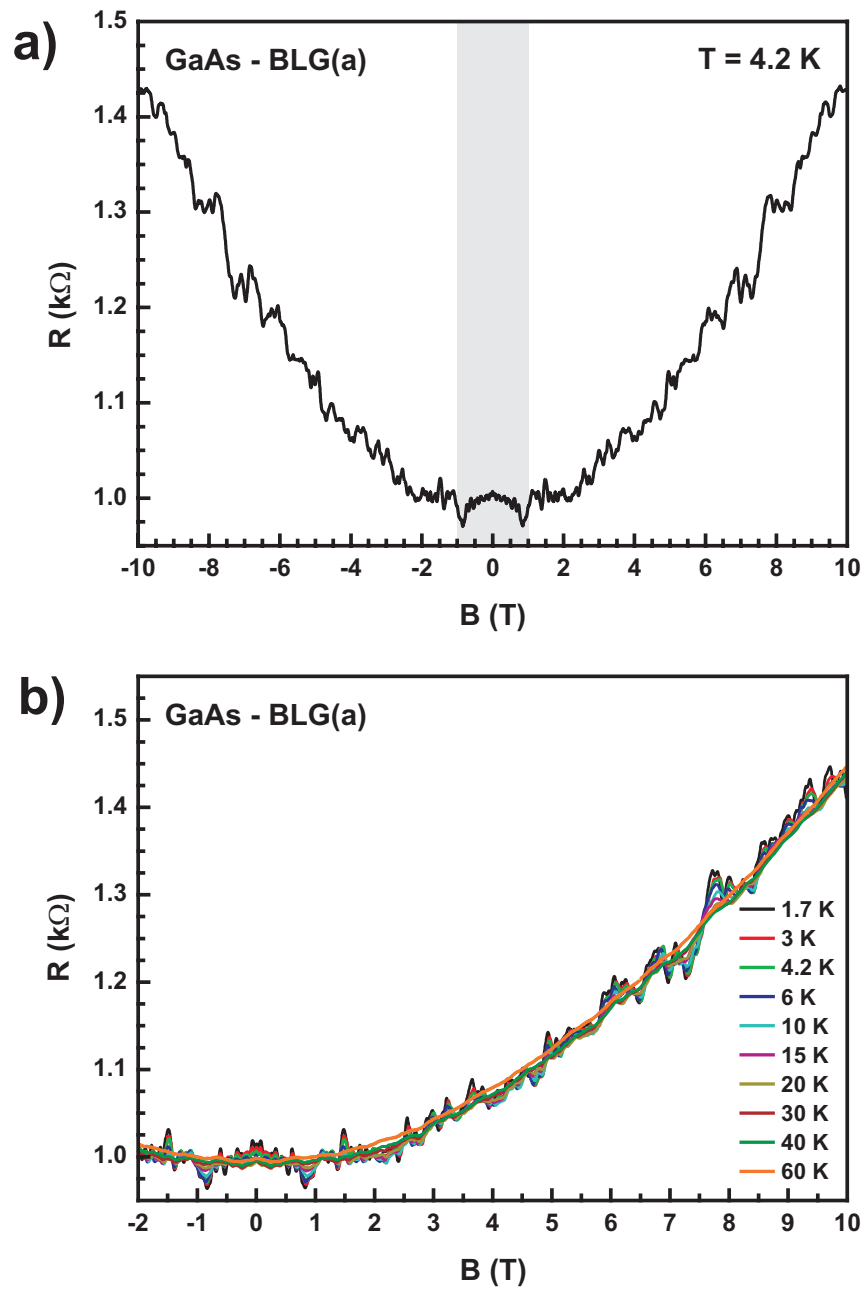
plied gate voltage measured as a function of a perpendicular applied magnetic field swept from -10 T to +10 T shows signatures of quantized transport (Figure 6.5). Small magnetoconductance oscillations interpreted as universal conductance fluctuations are visible superimposed to a parabolic background in the whole magnetic field range of  $B = \pm 10$  T. The Hall resistance  $R_{xy}$  shows a linear slope in the low-field region and rudimentary Hall-plateaus demonstrating transport in a two-dimensional charge carrier system. The positive Hall coefficient suggests transport in a hole system. From the slope of  $R_{xy}$  the intrinsic hole density was determined to  $p = 7.7 \cdot 10^{12} \text{ cm}^{-2}$ . In Figure 6.5 b) two gate sweeps of the longitudinal resistance  $R_{xx}$  are plotted. The black trace is measured without an applied magnetic field ( $B=0$  T), whereas the red line corresponds to the behavior with an applied magnetic field of  $B=-10$  T. The trace without field shows an increase of the resistance  $R_{xx}$  by increasing the gate voltage, further verifying holes as intrinsic charge carriers. The CNP point is expected to appear for much higher positive voltages, namely for  $U_{\text{Gate}} = 18.8$  V as will be demonstrated later. From the linear dependence of the conductivity taking into account the shape of the contact geometry and the charge injection parameter again the mobility can be determined. Due to the high intrinsic doping only the hole mobility for this monolayer sample (GaAs-MLG(b)) can be observed, which constitutes  $\mu = 1660 \text{ cm}^2/\text{Vs}$  and is almost a factor three lower compared to the bilayer sample GaAs-BLG(b). The data

acquired with an applied magnetic field of  $B = -10$  T also shows an increase in  $R_{xx}$ . Some changes in the slope, but no clear signatures for SdH oscillations are detectable by varying the carrier density over the gate voltage. Reasons for the absence of clear signatures for quantized transport can be found in the low charge carrier mobility and the high intrinsic charge carrier density together with the low breakthrough voltage that precludes larger changes of the two-dimensional charge carrier density.

In Figure 6.6 a), the Hall resistance  $R_{xy}$  for the same monolayer sample (GaAs-MLG(b)) is measured for different gate voltages from  $U_{Gate} = 3.5$  V to  $U_{Gate} = -1.5$  V. Variations in the Hall-slopes indicates gate-induced changes of the two-dimensional hole density, which can be determined from the Hall slope. The two-dimensional hole density  $p$  exhibits a linear dependency on the applied gate voltage  $U_{Gate}$  as demonstrated in the inset of Figure 6.6, where a shift of the CNP of about 18.8 V has been corrected. From the dependency of the carrier density on the gate voltage,  $n, p = \alpha \cdot U_{Gate,eff}$ , the charge injection parameter  $\alpha$  for the GaAs substrate was determined to be  $\alpha_{GaAs} = 4.1 \cdot 10^{11} \text{ cm}^{-2}/\text{V}$ . The measured value for the used GaAs/AlGaAs substrate is about four times higher than the theoretically estimated one. Nevertheless, both, theoretical and measured values are higher compared to the literature value for  $\text{SiO}_2$  with  $\alpha_{\text{SiO}_2} \approx 7.2 \cdot 10^{10} \text{ cm}^{-2}/\text{V}$  [22].

The magnetotransport measurements on the bilayer sample on GaAs (GaAs-BLG-(a)) shown in Figure 6.7 have been performed in two-terminal geometry with a perpendicular applied magnetic field up to  $B = \pm 10$  T without changing the carrier density by applying a backgate voltage. In the high-field region ( $|B| > 1.5$  T) signatures of quantized transport, namely SdH oscillations are detectable that are superimposed on a positive parabolic background. In the low field region quantum interference phenomena such as weak localization (WL) and universal conductance fluctuations (UCFs) were found. In the low field region these effects are superimposed by a negative parabolic background. Both regions are depicted for  $T = 4.2$  K in Figure 6.7 a). As depicted in Figure 6.7 b), SdH oscillations, WL signal, UCF and the negative parabolic background exhibit strong temperature dependent damping, whereas the positive parabolic background in the high field region is almost temperature independent. The temperature dependent damping of the SdH oscillations is demonstrated in Figure 6.8 a) after subtraction of the second order polynomial background at higher fields and plotted vs. the inverse magnetic field  $1/B$ . The Fast-Fourier Transformations (FFT) of the data shown in Figure 6.8 a) reveal two distinct maxima corresponding to densities  $p_2$  and  $p_3$  in the whole investigated temperature range ( $1.7 \text{ K} \leq T \leq 50 \text{ K}$ ) and a smaller maximum  $p_1$  (see Figure 6.8 b)). The two-dimensional carrier density seems to be  $p_3 = 1.29 \cdot 10^{12} \text{ cm}^{-2} = 2 \cdot p_2 = 4 \cdot p_1$ . The relation between  $p_1, p_2$  and  $p_3$  may be caused by spin- and valley degeneracy. The degeneracy of such a graphene or thin graphite layer is known to be  $g = 4$  [45]. From gate dependent measurements the type of charge carriers has been determined to be holes and from the density and the charge injection parameter  $\alpha$  the shift of CNP has been ascertained to 3.15 V. This means that the intrinsic hole density is rather low for this bilayer sample on GaAs (GaAs-BLG(a)) compared to most of all other investigated mono-, bi- and few-layer sample on

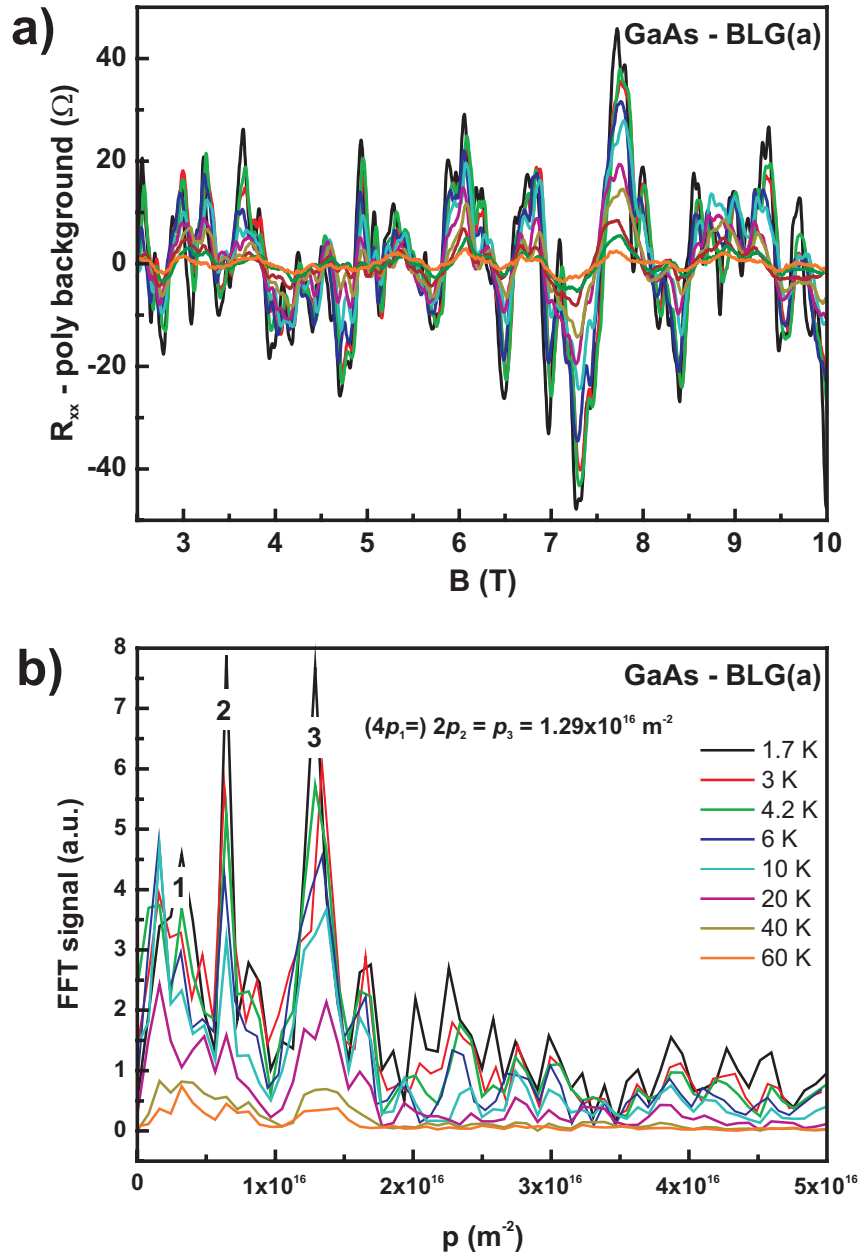




**Figure 6.7:** Temperature dependent two-terminal magnetoresistance of a bilayer graphene on GaAs (GaAs-BLG(a)). a) Magnetoresistance at 4.2K. The low-field region is marked. b) Temperature dependent magnetoresistance.

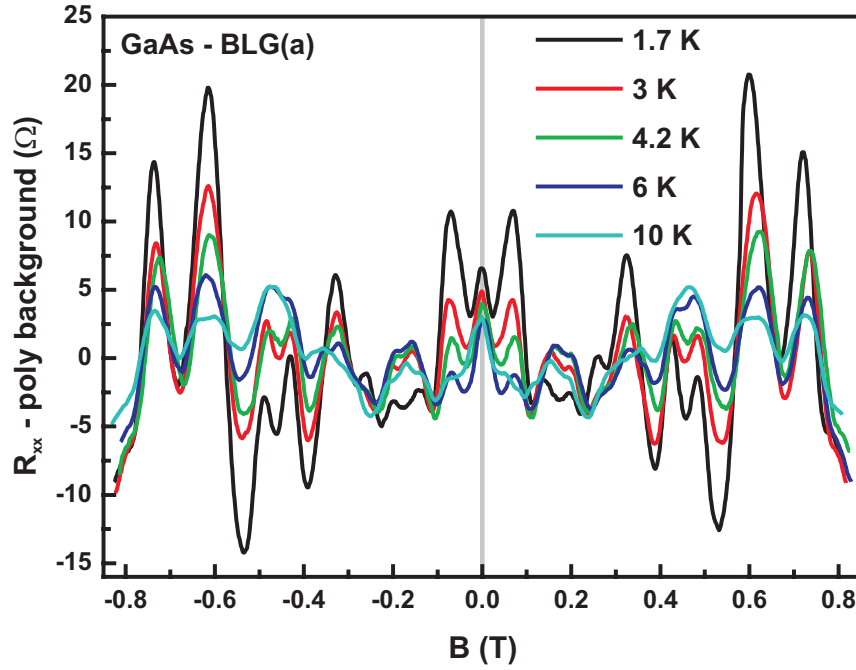
GaAs.

In Figure 6.9 the temperature dependent low field magnetoresistance (MR) traces are de-

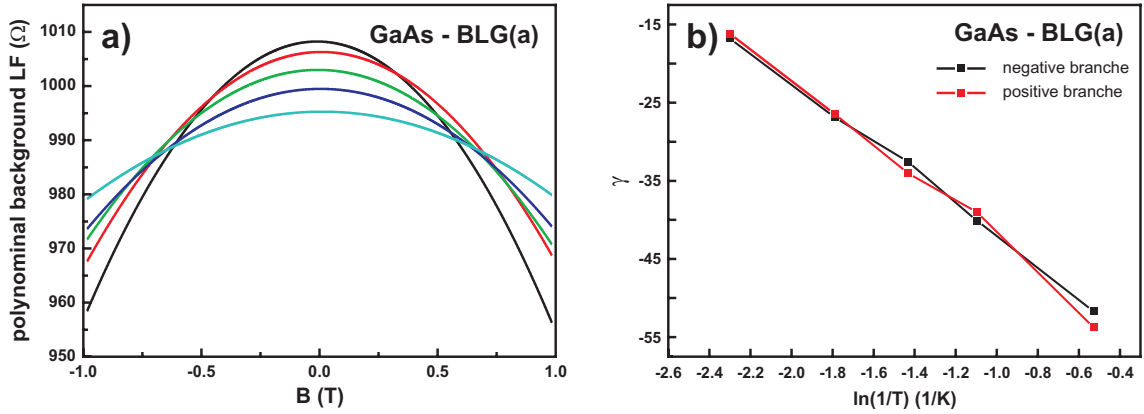


**Figure 6.8:** Analysis of the temperature dependent two-terminal magnetoresistance from Figure 6.7 a) high-field region ( $B \geq 2$  T) after subtraction of a second order polynomial. b) Fast-Fourier transformation of the reciprocal traces of a).

picted for temperatures between 1.7 K and 10 K after subtraction of a temperature dependent negatively curved parabolic background which is shown in Figure 6.10 a). Both, WL and UCFs are reproducible, symmetric regarding polarity of the  $B$ -field and strongly



**Figure 6.9:** Temperature dependent two-terminal magnetoresistance of the bilayer graphene on GaAs (GaAs-BLG(a)- same sample as in Figure 6.7 and Figure 6.8). The temperature dependent magnetoresistance for low magnetic fields ( $B \leq 2$  T) is plotted after subtraction of a second order polynomial background.



**Figure 6.10:** Analysis of the second order polynomial background of the electron-electron-interaction of Figure 6.9. a) Temperature dependent polynomial background in the low field region. b) Slope  $\gamma$  of the polynomial background as a function of  $B^2$  plotted vs  $\ln(1/T)$  corresponding to  $\tau_{ee}$ . Black traces correspond to the data taken for positive  $B$ -fields and red from negative fields.

temperature dependent. Surprisingly, WL signatures seems to be suppressed for lower

temperatures or superimposed by increased UCF-signal. As outlined at the end of this chapter, from this quantum correction to the classical Drude conductivity, the phase coherence length  $L_\Phi$  caused by inelastic scattering and the temperature dependence of  $L_\Phi$  will be determined as demonstrated in references [124, 139, 140]. The temperature dependent negatively curved parabolic background could also be induced by a quantum correction to the classical Drude conductivity due to impurity (electron-electron) interaction. Assuming transport in a diffusive channel in the metallic regime ( $E_F \tau_{ee}/\hbar \gg 1$ ), the impurity interaction time  $\tau_{ee}$  can be deduced from the parabolic background following the procedure demonstrated by Choi and coworkers [141]. The parabolic background can be written as

$$\Delta\rho_{xx}(B) \propto \rho \left( \frac{e\tau_{ee}}{m^*\sigma_0} \right)^2 \cdot B^2 \cdot \delta\sigma_{ee} \quad (6.2)$$

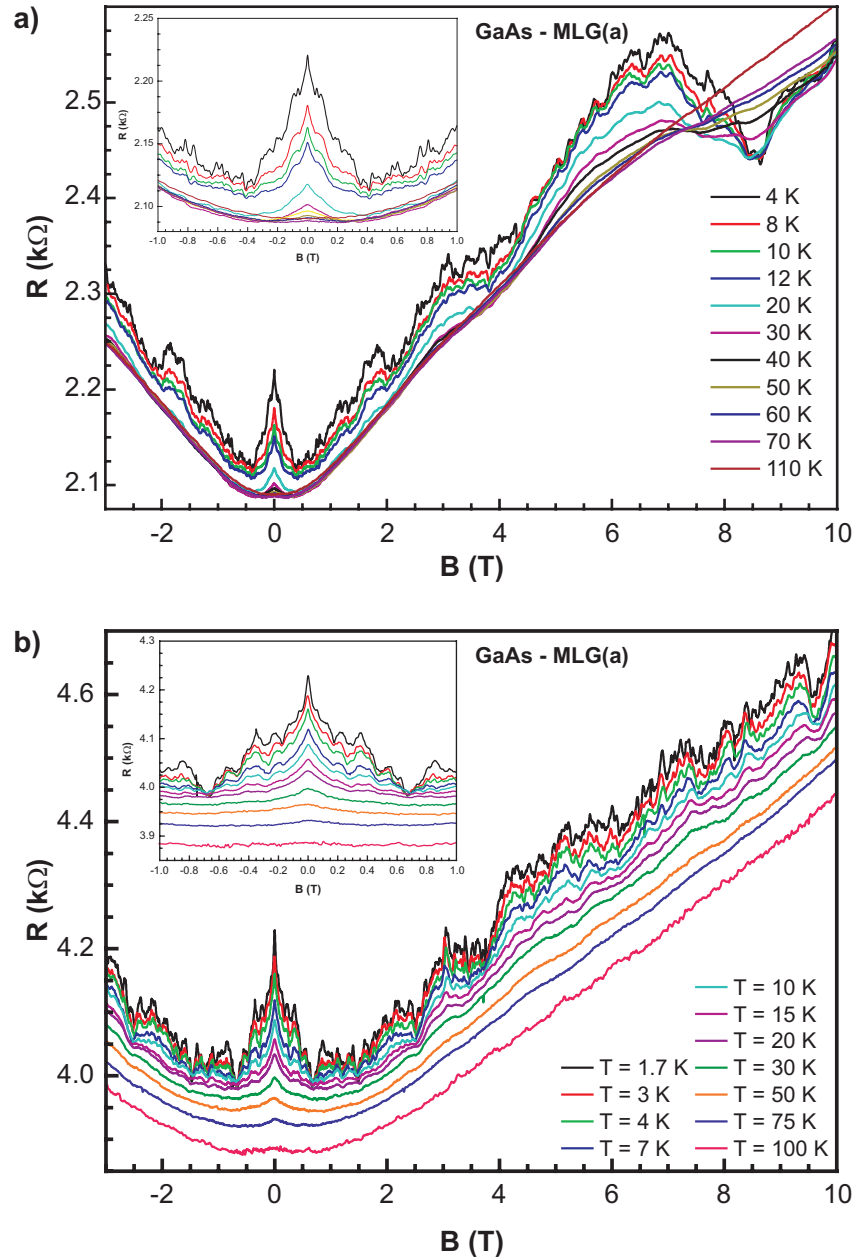
with  $m^*$  effective mass,  $\sigma_0$  classical Drude conductivity and  $\delta\sigma_{ee}$  correction to the Drude conductivity due to electron-electron interaction. For  $k_B T \tau_{ee}/\hbar < 1$  theory predicts for the two-dimensional case

$$\delta\sigma_{ee} = - \left( 4 - 3 \frac{2+F}{F} \ln \left( 1 + \frac{F}{2} \right) \right) \left( \frac{e^2}{2\pi^2\hbar} \right) \ln \left( \frac{\hbar}{k_B T \tau_{ee}} \right) \quad (6.3)$$

with  $F = \int \frac{d\Theta}{2\pi} (1 + \frac{2k_F}{\kappa} \sin(\frac{\Theta}{2}))^{-1}$ ,  $k_F$  the Fermi wave vector and  $\kappa$  the inverse screening length. The slopes  $\gamma$  of  $R(B)$  plotted as a function of  $B^2$  for different temperatures are collected in Figure 6.10 b). The slope  $\gamma$  is linearly dependent on  $\ln(1/T)$ . From this correlation  $\tau_{ee}$  can be extracted using equations (6.2) and (6.3). The resulting electron-electron interaction time is  $\tau_{ee} = (0.157 \cdot \frac{m^*}{m_0})$  ps. Assuming  $m^* = 0.1 m_0$ , the mass of charge carrier in BLG [142] or the mass of the heavy holes in FLG [1], one obtains  $\tau_{ee} = 15.7$  fs. This value seems to be reasonable compared to values found for two-dimensional charge carrier systems in conventional heterostructures [141].

### 6.3 Aging process of graphene

By dealing with transport properties of graphene, we had to address the problem that the environment changes the properties of these ultra-thin sheets. It is established that mobility and further transport properties are very sensitive to the surroundings and surfactants on the graphitic sheet [20]. Since the graphene sheets investigated in this thesis are not suspended and not cleaned by heat treatment, the mobilities of the flakes are low but comparable to flakes on  $\text{SiO}_2$  substrates. Thus, it is not astonishing that the transport properties of the graphene sheets changes significant between different cooling down cycles, where the sample is exposed to air. Of course, the samples are preserved in vacuum as long as possible and the time in air is reduced as much as possible. But as visible in



**Figure 6.11:** Reduction of the sample quality with time. Both panels show the temperature dependency of a two-terminal measurement on GaAs-MLG(a). a) shows a resistance that is half the resistance in b). A clear developing Shubnikov-de Haas oscillation is observable at  $\sim 9$  T. Additional signs for quantized transport are found for lower magnetic fields. b) has been measured  $\approx 200$  days after a). In both panels the inset shows the corresponding low field region where weak localization can be observed.

Figure 6.11, the transport signals are significantly altered in a second cooling down after 200 days with carefully storing in vacuum between the measurements. In Figure 6.11 temperature dependent magnetotransport measurements on a monolayer graphene sample on GaAs (GaAs-MLG(a)) are shown. Both measurements are carried out in two-terminal geometry using identical contacts. In the first measurement depicted in Figure 6.11 a) clear signal of Shubnikov-de Haas oscillations are visible up to  $T = 50$  K indicating pleasant quality of the crystal and high charge carrier mobility. In the low field region a strong positive magnetoresistance due to WL is observable up to  $T = 50$  K (see inset of Figure 6.11 a). Another phase coherent transport phenomenon, namely UCFs are visible in the whole magnetic field range up to  $T = 20$  K. Disregarding the WL corrected sheet resistivity, e.g. taken at  $|B| = 0.5$  T, increases only weak with decreasing temperature. All these features are clearly changed in the second cooling cycle as collected in Figure 6.11 b). The two-terminal resistance is almost doubled caused by degrading of the contact and/or sheet quality. The disappearance of the clear SdH oscillations points towards strongly reduced quality and simultaneously mobility of the sample. The WL maxima are broadened and disappear already at about  $T \approx 30$  K compared to  $T \approx 50$  K at the first measurements cycle. UCFs disappear at nearly the same temperature of about  $T = 20$  K, but seems to be more pronounced at the second cooling down also pointing towards increased scattering potential in the second run. Further, the resistance increase is stronger dependent on lowering the temperature. Regrettably, it was not determinable, whether the intrinsic type and density of carrier and position and shape of the CNP has been changed. All together, it is evidently that the sample has dramatically changed between the two measurement cycles. However, not only the aging process between two cooling downs, but also the aging during the measurements is demanding. It is not rarely that individual contacts or the dielectric layer are degrading during all kind of measurements without exposure to air. Often this disturbs comprehensive series of measurements. The reason can be questioned in the mechanical stress between metal contacts and graphene, microfissures in the graphene sheets that appears sometimes close to the contacts. We learned that larger overlap of the contact to graphene rectifies this problem by simultaneously loosening space for contacts and hence variation in the measurements geometry. This is the reason why smaller samples are often contacted only with two or three contacts.

Also the substrate contributed to the aging process. Due to the easy visibility of graphene on SiO<sub>2</sub>, only one optical microscopy image and one EBL step is needed to detect, classify the graphene flake and to prepare it for electrical measurements. On other substrates further microscopy studies are needed such as SEM and AFM to detect and classify the sheets. During SEM hydrocarbon is cracked and deposited on the substrate and during AFM measurements the sample is exposed to air for a long time. And of course this all takes some time during that the sample is aging. For this reason Micro-Raman spectroscopy or Imaging Ellipsometry could be possible detection methods to improve the quality of graphene on various substrate.

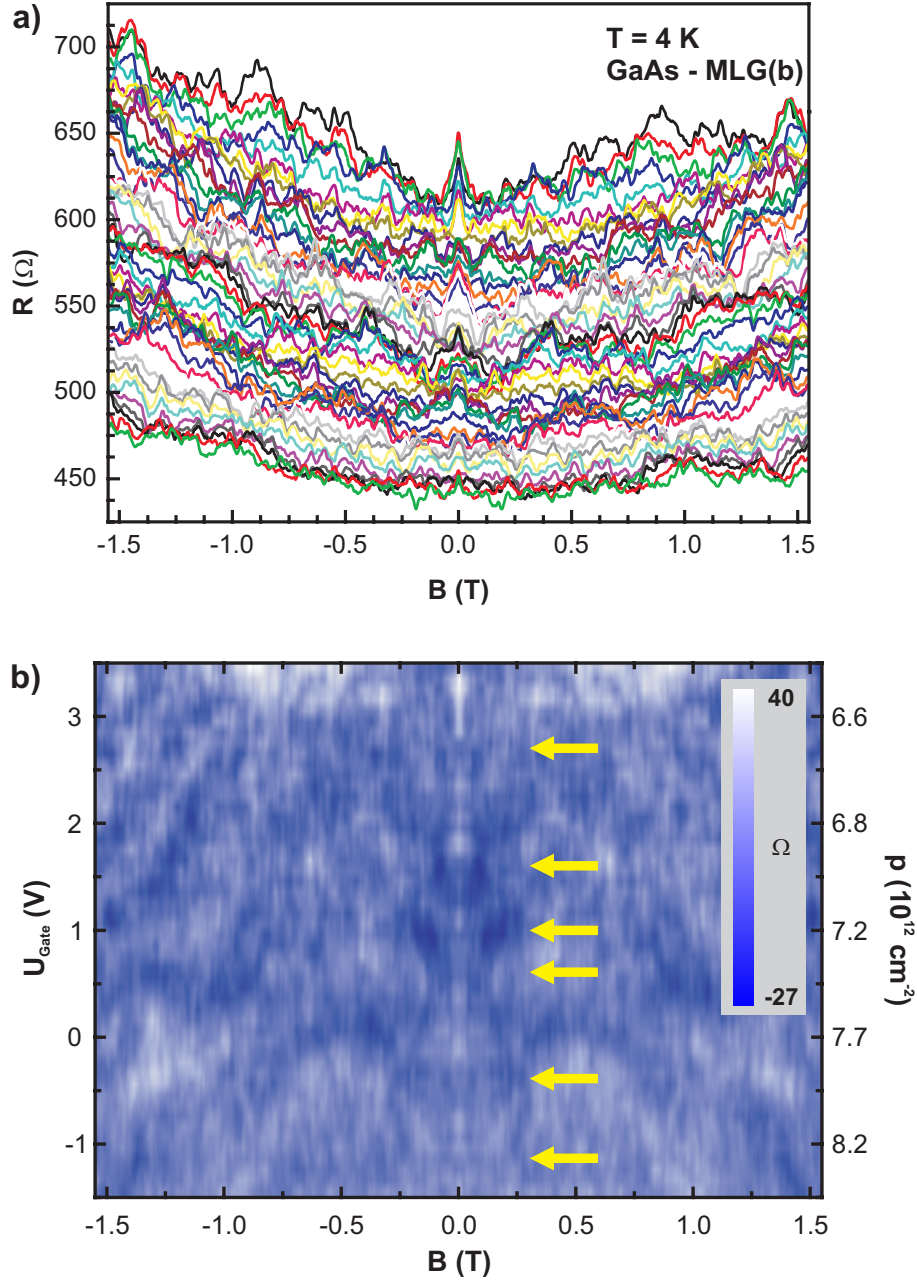
## 6.4 Phase coherent transport

In the low temperature magnetoresistance measurements two phase coherent transport phenomena were observable in all graphene samples, independent from the number of layers. The magnetoresistance effect around  $B = 0$  T is addressed to weak localization (WL) effect and occurs in samples with a phase coherence length larger than the elastic scattering length. Magnetoconductance oscillations, called universal conductance fluctuations (UCFs), arise in mesoscopic disordered samples, when the size of the conductor is in the order of the phase coherence length. The principles of both effects are described in chapter 2.

### 6.4.1 Weak localization

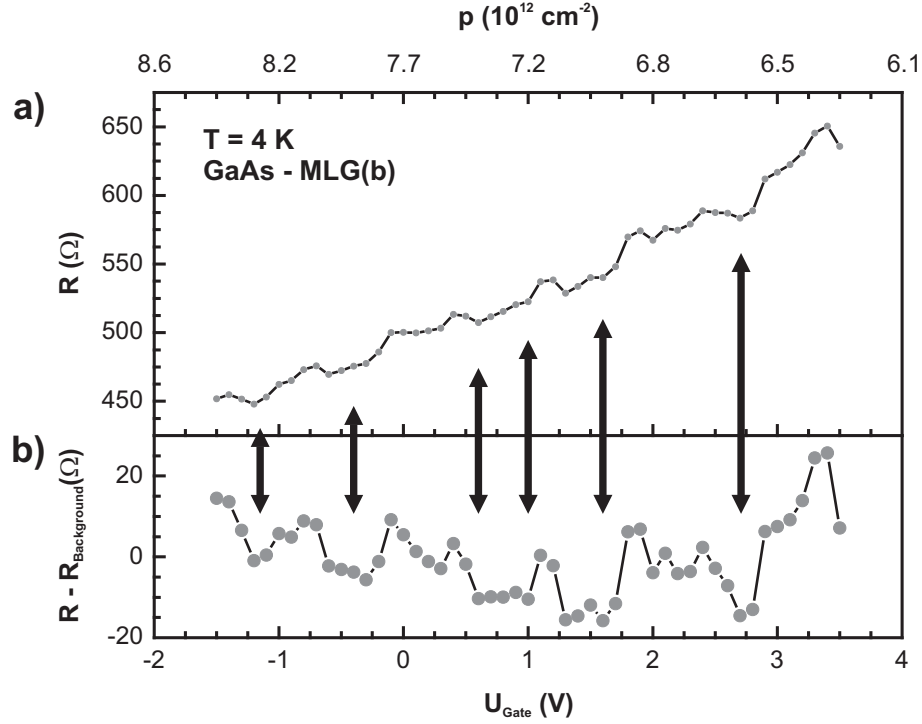
Weak localization arises from constructive interference between time reversed partial waves of the charge carriers in disordered samples. Due to the chirality of the charge carriers, quantum interference in graphene is different to conventional semiconductors [53]. Consequently the carriers in graphene have an additional Berry phase of  $\pi$ . As shown in Figure 6.12 a) for various gate voltages the quantum correction of the resistance is usually measured by applying a perpendicular magnetic fields  $B$ . WL in graphene depends not only on the inelastic scattering of electrons, characterized by the phase coherence length  $L_\Phi$ , but also on the elastic scattering caused by impurities and lattice defects. The inelastic scattering is represented by two characteristic lengths, the intravalley scattering length  $L_\star$  and the intervalley scattering length  $L_i$ . Large  $L_\star$  suppresses the interference within one valley due to chirality breaking defects and random magnetic fields due to ripples and dislocations, whereas large  $L_i$  restores the interference by mixing the two valleys with opposite chirality [53]. Intervalley scattering is caused by sharp defects, e.g. sample edges, whereby charge carriers can be scattered between valleys. Interestingly, in graphene both, weak localization and weak anti-localization was reported to appear in one sample depending on the ratio  $L_\Phi/L_\star$  and  $L_\Phi/L_i$  that can be tuned by changing carrier density and temperature [53].

The data in Figure 6.12 were measured in a four-terminal geometry at  $T = 4.2$  K on the monolayer sample GaAs-MLG(b), which exhibits a charge carrier mobility of  $\mu = 1660$  cm<sup>2</sup>/Vs as shown in section 6.2. The magnetoresistance traces were taken for different two-dimensional hole densities ranging from  $8.5 \cdot 10^{12}$  cm<sup>-2</sup> to  $6.3 \cdot 10^{12}$  cm<sup>-2</sup>. The hole density is varied by changing the backgate voltage from -1.5 V to 3.5 V. Please note that the traces are not vertically shifted for clarity. The offset is caused by the fact that decreasing the carrier density increases simultaneously the sheet resistivity. Remember, the high-field magnetotransport behavior of this monolayer sample was already shown in Figure 6.5, where also an optical micrograph of the device is inserted. For almost all curves, a positive magnetoresistance due to weak localization appears around  $B = 0$  T. Additionally, UCFs are visible for the whole swept magnetic field range. For better com-



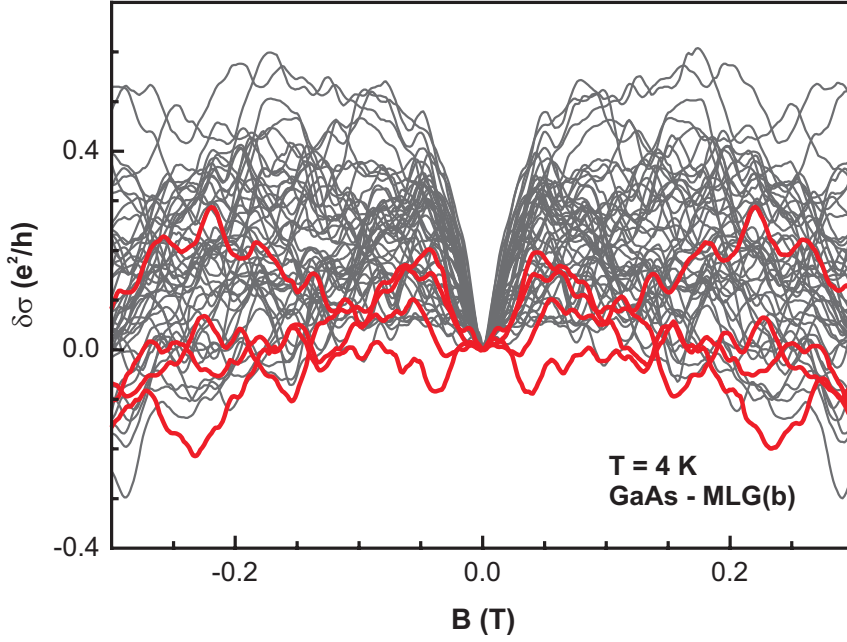
**Figure 6.12:** Weak localization measurements for different gate-voltages of a monolayer sample on GaAs (GaAs-MLG(b)). a) Gate-voltage dependence of the low-field region of  $R_{xx}$  for applied voltages between 3.5 V and -1.5 V. b) Data from a) in a false color plot of the low-field region of  $R_{xx}$  after subtraction of a second order polynomial background. The WL signal is aperiodically suppressed with the hole density. The suppressed regions are marked with arrows.





**Figure 6.13:** Vertical traces through the plots in Figure 6.12 along  $B=0$  T. a) The data without any correction. b) The data of a) corrected by a linear regression (corresponding to the  $B=0$  T profile of Figure 6.12 b)). The regions, where the WL signal is suppressed are marked with arrows.

parison of the WL signal, the curves are displayed in Figure 6.12 b) in a false color plot, where the second order polynomial background is subtracted. Bright areas correspond to high resistance values and dark blue ones to low resistance values. Surprisingly, the WL signal aperiodically disappears for certain carrier densities. The regions, where the WL is suppressed are marked with arrows in Figure 6.12 b). Linecuts through this plots along  $B = 0$  T are shown in Figure 6.13 without a) and after b) correction with a linear regression taking into account the carrier density dependency of the sheet resistivity. In both graphs the suppression of the WL signal is clearly observed. From simple analysis it was not possible to extract a periodicity in the curves. The regions with vanishing WL signals, and simultaneously regions with very distinct WL signals are spaced in gate voltage between  $\Delta U = 0.9$  V and  $\Delta U = 1.1$  V corresponding to changes in the two dimensional charge carrier density of between  $\Delta p = 0.37 \cdot 10^{12} \text{ cm}^{-2}$  and  $\Delta p = 0.47 \cdot 10^{12} \text{ cm}^{-2}$ . This is not a clear periodicity, but the change in the hole density needed to come from one to the next suppressed region are similar. The visibility of the suppression of the WL signals that could also be interpreted as a starting transition from WL to WAL behavior is improved by plotting the normalized magnetoconductance for all measured hole densities as revealed in Figure 6.14. The curves for vanishing WL effect are red colored and correspond to the

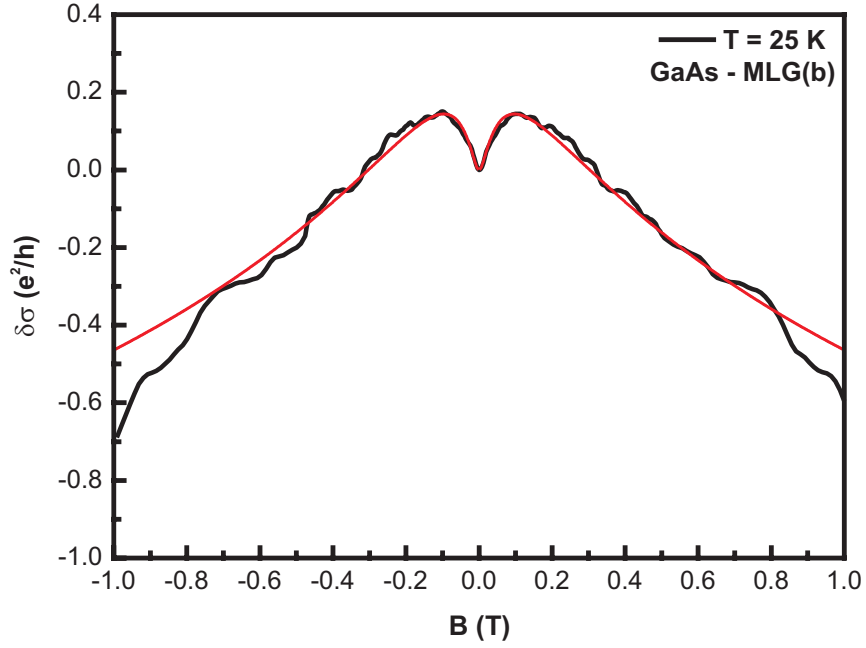


**Figure 6.14:** Normalized magnetoconductance traces for different backgate voltages measured on sample GaAs-MLG(b) (extracted from Figure 6.12). The red traces correspond to gate voltages, where the WL signal vanishes.

density (backgate voltage) values marked by arrows in Figures 6.12 and 6.13. We found such an aperiodic suppression of the WL signal for graphene on GaAs independent of the number of layers.

Suppression of WL or transition from WL to weak anti-localization (WAL) was reported for graphene on  $\text{SiO}_2$  dependent on the carrier density or the temperature [53, 55, 139], but to best of our knowledge no recurrent suppression by continuously tuning the carrier density is reported in literature so far. Only in reference [124] a similar plot was shown for graphene on  $\text{SiO}_2$ , however the authors did not discuss this issue.

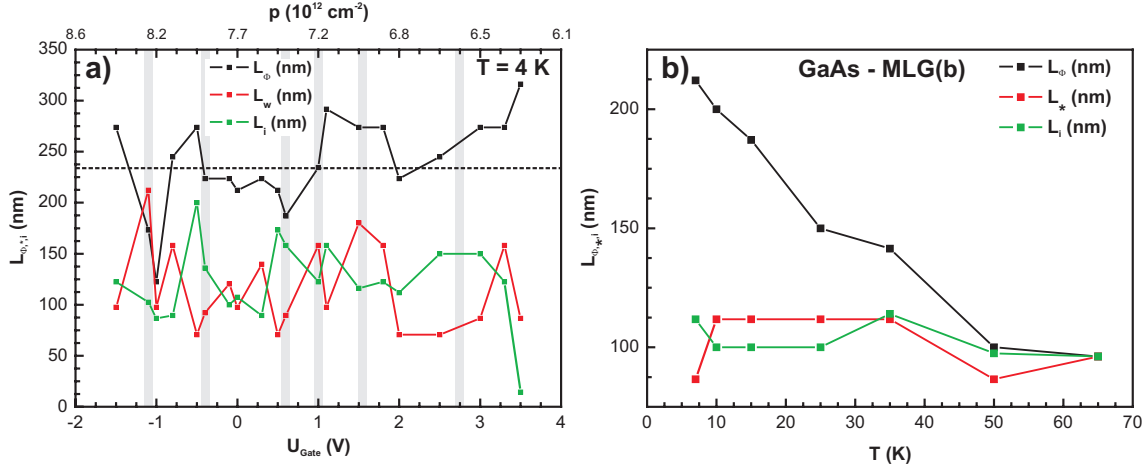
Most investigations of WL and WAL effects of graphene on  $\text{SiO}_2$  are done by averaging over a certain range of carrier density to reduce the UCFs and hence pronounce the WL signal. In this way, the curves can also better fitted by equation (2.14) [53, 54]. But by averaging only over a voltage range of  $\Delta U = 1$  V [53], what seems minor for  $\text{SiO}_2$ , where gate voltages of about  $U_{\text{Gate}} = \pm 100$  V can be applied, the uncertainty in the carrier density constitutes  $\Delta p \approx 7.4 \cdot 10^{10} \text{ cm}^{-2}$ . Whereas the separation of the suppressed regions in our experiments are found to be three to five time larger. One might speculate, that the effect of recurrent vanishing WL signal by tuning the carrier density could also be visible for graphene on  $\text{SiO}_2$ . Moreover, the WL signal and hence its (possible) suppression is more pronounced for graphene on GaAs compared to graphene on  $\text{SiO}_2$ . The suppression of WL may be induced by mesoscopic corrugations of the graphene sheets or the underlying



**Figure 6.15:** Measured magnetoconductance at  $T = 25$  K and  $U_{Gate} = 0$  for sample GaAs-MLG(b) (black) and fitted magnetoconductance (red).

substrate or by interaction with the substrate. The origin of this effect is still unclear and also first discussions with theory have not yet given any result.

From careful analysis of magnetoconductance curves as depicted in 6.14, the phase coherence length  $L_\Phi$  and the electric scattering lengths, intervalley scattering length  $L_i$  and intravalley scattering length  $L_\star$  can be determined regarding to equation (2.14). In Figure 6.15 the magnetoconductance curves (black) for the monolayer GaAs-MLG(b) taken for  $U_{Gate} = 0$  V at  $T = 25$  K is fitted (red) using the equation mentioned above. Obviously, the fit matches the measured data very well in the magnetic field range of  $B = \pm 0.8$  T. The WL signal was measured as function of different carrier densities changed by tuning the backgate voltage and in dependence of the temperatures between  $T = 4.2$  K and  $T = 65$  K. Since this relative high temperatures the quantum interference effect still survives. But it is generally known that the WL effect in graphene is visible up to much higher temperatures ( $T = 200$  K) [53] compared to conventional semiconductors and metals. In Figure 6.16, the three characteristic scattering length  $L_\Phi$  (black),  $L_\star$  (red) and  $L_i$  (green) achieved from fits of the magnetoconductance are collected. The dependence from the carrier density (backgate voltage) is displayed in Figure 6.16 a) and from the temperature in b). The solid black line denotes the value for  $L_\Phi$  determined from the averaged magnetoconductance curve over all measured backgate voltages  $-1.5 \text{ V} \leq U_{Gate} \leq 3.5 \text{ V}$  at  $T = 4.2$  K and constitutes to  $L_\Phi = 223$  nm. This value lies in between all resulting values found for  $L_\Phi$  lying

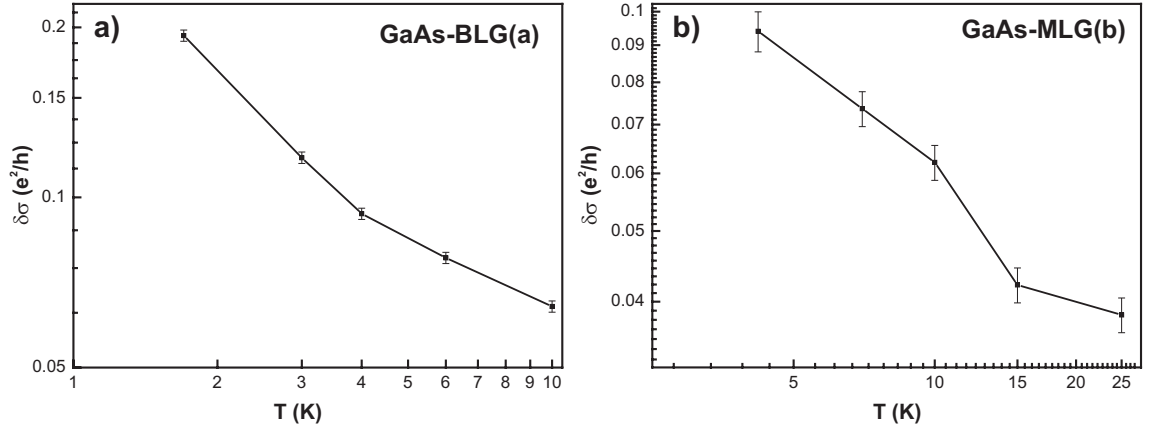


**Figure 6.16:** Phase coherence length  $L_\Phi$  (black) intravalley scattering length  $L_*$  (red), and intervalley scattering length  $L_i$  (green) a) at  $T = 4.2$  K in dependence of the carrier density (gate voltage) and b) in dependence of the temperature at  $U_{\text{Gate}} = 0$ .

between  $122 \text{ nm} \leq L_\Phi \leq 317 \text{ nm}$ . The grey shaded lines denotes the two-dimensional hole density regions where the suppression of the WL signals has been found. The same regions are marked with arrows in 6.12 and 6.13. Here, not an unambiguous relation can be entitled, however a clear direction seems to emerge. For the suppressed regions the phase coherence length  $L_\Phi$  is definitely lowered relative to neighboring regions. Moreover,  $L_\Phi$  seems slightly to increase in average with decreasing carrier density, but this trend has to be confirmed. The values for intravalley scattering length  $L_*$  (red) and the intervalley scattering length  $L_i$  (green) are both struggling between  $70 \text{ nm} \leq L_{*,i} \leq 212 \text{ nm}$ . The differences in the scattering lengths between neighboring hole density regions are very large. The trend regarding the hole density for  $L_*$  and  $L_i$  seems to be the opposite to  $L_\Phi$ . Decreasing the hole density slightly decreases both elastic scattering lengths in average. Also  $L_*$  and  $L_i$  are generally lower in the grey mark regions.

The temperature dependency of the three coherence lengths are given in Figure 6.16 b). The values for  $L_*$  and  $L_i$  constitute both to about  $L_{*,i} = 110 \text{ nm} \pm 10 \text{ nm}$  and are independent from the temperature between  $T = 4.2 \text{ K}$  and  $T = 35 \text{ K}$  and decrease minor with increasing temperature for  $T > 35 \text{ K}$ . In contrast to that, the phasecoherence length  $L_\Phi$  decreased linearly with increasing temperature from  $212 \text{ nm}$  at  $T = 7 \text{ K}$  to  $96 \text{ nm}$  at  $T = 65 \text{ K}$ . This behavior was expected from literature [45, 98], and references therein.

Generally, the relation  $L_\Phi > L_{*,i}$  obtained for graphene on  $\text{SiO}_2$  [53, 98] is also valid for graphene on GaAs. The determined values for the characteristic length for graphene on GaAs, especially values and temperature dependency of the phase coherence length  $L_\Phi$  caused by inelastic scattering are in good comparison of the values reported in literature [53, 54], and references therein. Finally, we had to refer about the uncertainty and the error done by fitting the magnetoconductance data to equation (2.14). Due to three free



**Figure 6.17:** Temperature dependent conductance fluctuations amplitude extracted from the low field region for a) the bilayer sample GaAs-BLG(a) and b) monolayer sample GaAs-MLG(a).

parameters, the fit routine was not able to adjust all values automatically. Therefore, the fit had to be optimized by hand, what was a little challenging, because all parameters affect each other.

### 6.4.2 Universal conductance fluctuations

Using the example of the monolayer sample on GaAs-MLG(b) and the bilayer sample GaAs-BLG(a) the temperature dependent investigation of the amplitude of the magneto-conductance oscillations induced by UCFs are investigated. The related UCFs are visible in the magnetotransport measurements shown in Figures 6.12 and 6.9 for GaAs-MLG(b) and GaAs-BLG(a), respectively. In both figures it is clearly visible that the fluctuations are very reproducible, damped by increasing the temperature and symmetric in the magnetic field. To extract the amplitude  $\delta\sigma$  of the UCF a second order polynomial background was subtracted from the measured data. In Figure 6.17 the corresponding amplitudes  $\delta\sigma$  are plotted versus the temperature in a double-logarithmic plot. Sample GaAs-BLG(a) was investigated between  $T = 1.7$  K and  $T = 10$  K and sample GaAs-MLG(b) between  $T = 4.2$  K and  $T = 25$  K. As expected from literature, the amplitude  $\delta\sigma$  of the UCFs follows a power law in  $T$ . In the tested temperature range the conductance fluctuation amplitude does not saturate. UCFs were clearly visible in all investigated graphene samples independently from the number of layer for temperatures up to about  $T \approx 30$  K.

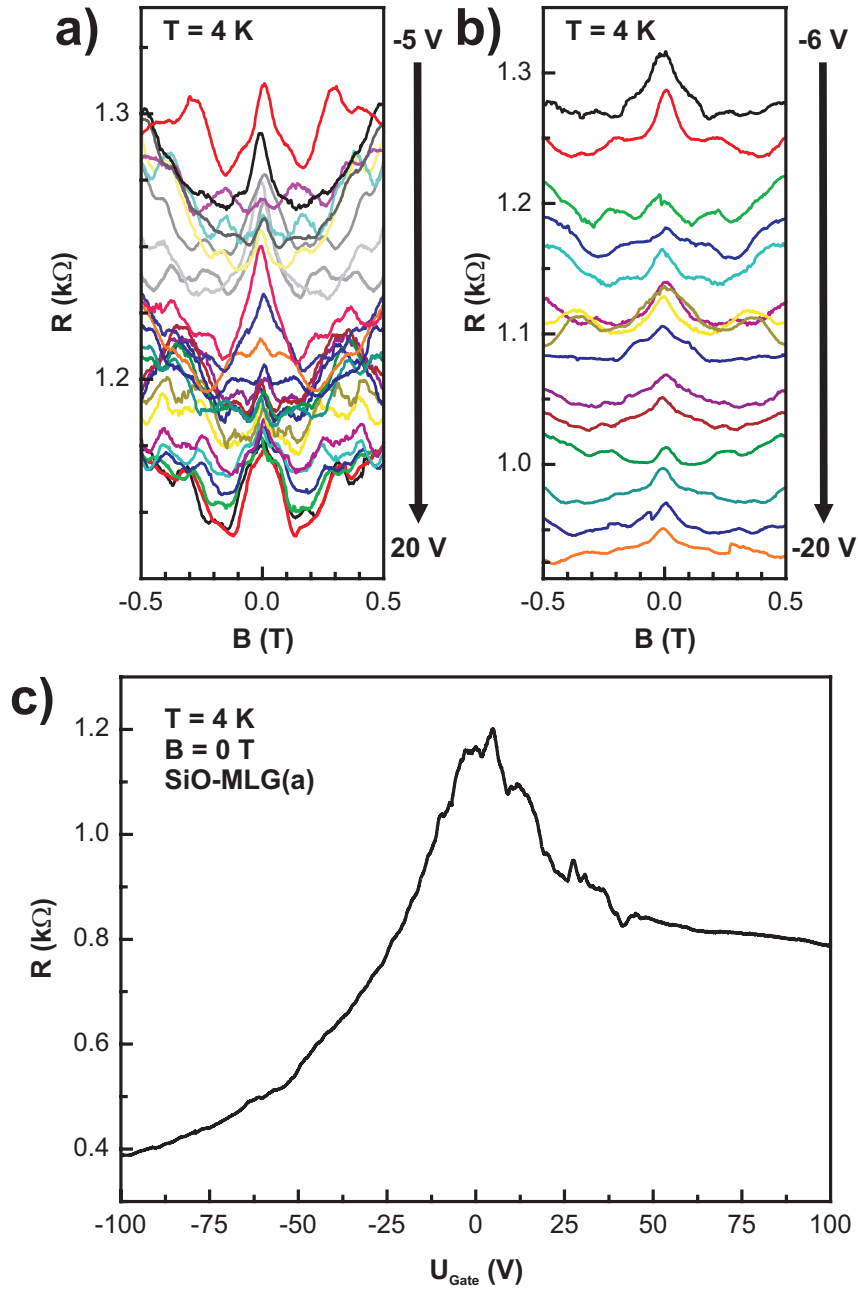
### 6.4.3 Comparison with graphene on $\text{SiO}_2$

For comparison, resistance  $R$  versus gate voltage  $U_{\text{Gate}}$  and WL measurements for different backgate voltages are depicted in Figure 6.18 on a trilayer sample on  $\text{SiO}_2$ . The

measurements were carried out at  $T = 4.2$  K. The resistivity at  $B = 0$  T and  $T = 4.2$  K was observed for backgate voltages of  $U_{Gate} = \pm 100$  V corresponding to charge carrier densities variation for holes and electrons up to about  $p, n = 7.4 \cdot 10^{12} \text{ cm}^{-2}$ . The CNP is broadened similar to the findings for a graphene trilayer on  $\text{SiO}_2$  in reference [36] and can be explained by bandoverlap of valence and conduction band for low energies. The CNP appears approximately at  $U_{Gate} \approx 0$  V and the curve is not symmetric for the hole and electron region as shown in Figure 6.18 c). Also WL signal appears for this trilayer sample on  $\text{SiO}_2$ . The WL in both, hole and electron region is observed for several gate voltages up to  $U_{Gate} = \pm 20$  V corresponding to two-dimensional hole and electron densities up to  $p/n \approx 1.5 \cdot 10^{12} \text{ cm}^{-2}$  at  $T = 4.2$  K. The magnetoresistance curves for the hole and electron regions are plotted in Figure 6.18 a) and b), respectively. The WL effect seems to be more pronounced in the hole region. Interestingly, the amplitude of the WL signal in the hole region seems not to behave monotonic with increasing hole density, whereas in the electron region the amplitude of the WL decreases with increasing the two-dimensional electron density. However, no evidence of suppression of the WL effect or a transition from WL to WAL was found for this sample. The reason for the differences between holes and electrons are not clear, but a hint for different scattering mechanism is given by the asymmetry of the resistivity around the CNP. The differences in the WL behavior between graphene on GaAs and  $\text{SiO}_2$  are distinct, but the origin behind the influence of the substrate on the WL behavior is absolutely not clear, yet.

## 6.5 Discussion

In conclusion, we have shown, that graphene on crystalline epitaxial substrates can be prepared for magnetotransport experiments. Temperature and gate dependent sheet resistivity behaves as expected. Due to the low break-through voltage of the dielectric GaAs and InGaAs layers a clear signature of a CNP was detectable only for one sample. However the origin of the shift of the CNP towards holes on these semiconducting substrates is not yet clear. In magnetotransport measurements signatures of quantized transport phenomena, SdH-oscillations in  $R_{xx}$  and Hall-plateaus in  $R_{xy}$  have been observed. The carrier density was detectable the  $(1/B)$ -periodicity of the SdH-oscillations and from the classical Hall slope. Therefrom, the charge injection parameter  $\alpha$  was determined for the GaAs substrate to  $\alpha = 4.2 \cdot 10^{10} \text{ cm}^{-2}/\text{V}$ . Charge carrier mobilities between  $\mu = 1660 \text{ cm}^{-2}/\text{Vs}$  and  $\mu = 3600 \text{ cm}^{-2}/\text{Vs}$  were observable. The values are in good agreement with the values reached in our group also for graphene on  $\text{SiO}_2$  without an additional in-situ cleaning step. Interestingly, from the gate dependence of the resistance it is obvious that the intrinsic charge carriers for graphene of GaAs and InGaAs are always holes, in contrast to graphene on  $\text{SiO}_2$  where both electrons and holes are observable. For a BLG on GaAs with a lower intrinsic carrier density a negative parabolic background was found superimposed on the MR traces in the low field region. From the temperature dependence of the



**Figure 6.18:** Magnetotransport measurements of a trilayer graphene flake on SiO<sub>2</sub> substrate. WL traces for electrons a) and holes b) are plotted. c) Sheet resistance in dependence of the applied gate voltage.

bending, the electron-electron interaction time  $\tau_{ee}$  has been extracted. For all graphene samples UCFs were found in longitudinal and Hall measurements in the whole magnetic

field region. WL was found in the low-field region which got suppressed for specific applied gate-voltage values. This behavior was not found for graphene on  $\text{SiO}_2$ . The phase coherence length  $L_\Phi$ , the intravalley scattering length  $L_\star$  and the intervalley scattering length  $L_i$  was extracted from the WL traces. Whereas  $L_\star$  and  $L_i$  are more or less temperature independent,  $L_\Phi$  decreases linearly with increasing temperature as expected from literature and similar to the findings of graphene on  $\text{SiO}_2$  [45, 98].  $L_\Phi$ ,  $L_\star$  and  $L_i$  seems to be reduced at the charge carrier region, where the suppression of the WL signal takes place. The origin behind these effects is unclear up to now. Furthermore, we have found the amplitude of the UCF  $\delta\sigma$  to follow a power law as expected [45].

Further comparative studies of the phase coherence length  $L_\Phi$  determined independently from UCFs and WL as a function of temperature and gate voltage (carrier density) could shed some light on the origin of the aperiodic suppression of the WL signal in graphene. For a more detailed interpretation of the rich results found in magnetotransport a independent determination of the layer number of the graphene sheets by Raman microscopy seems to be indispensable.



# Chapter 7

## Conclusion

This thesis deals with the influence of the substrate materials primary on the mechanical, electrical and magnetotransport properties of graphene. Therefore we used molecular beam epitaxial grown GaAs-based crystalline substrates and compare the results with graphene on the commonly used silicon substrates with 300 nm silicon dioxide on top. One advantage of these MBE-grown substrates is that the optical and electrical properties as well as the surface morphology and doping can precisely be tailored. Successful preparation and detection of graphene on such crystalline non Si/SiO<sub>2</sub> substrates would allow investigating both, the influence of the interaction between individual charged or magnetic specimen, phonons or various surface morphologies on graphene and the probing of graphene with other techniques, e.g. with surface acoustic waves, wherefore crystalline substrates are needed. By the way, GaAs is a well established semiconductor in industry and research. It is often used for high frequency-devices e.g. for terahertz application and therefore to combine this material with graphene, from which transistors with ultra fast switching rates have been realized [12, 13], seems to be promising.

In the framework of this thesis, the deposition, detection of graphene and the preparation of transistor like devices for electrical characterization was successfully transferred to GaAs based substrate materials. Because of the absence of a distinguishable contrast between graphene and semiconducting substrates compared to the Si/SiO<sub>2</sub> with a certain thickness of the oxidized layer, the detection and the determination of the number of layer was very challenging. With a combination of a scanning electron microscope equipped with an in-lens detector and an atomic force microscope we were successful and able to characterize the graphitic flakes. However, this process is very time-consuming and only the lateral dimension and the absolute height were determinable. Due to some surfactants between surface and graphene or on top of graphene the number of layer was only observable with an uncertainty of about one. Micro-Raman spectroscopy was applied to verify the layer number, however seems only work for InGaAs substrates not for GaAs/AlGaAs ones. This may be caused by covering the weaker Raman signal by the strong photolumi-

nescence signal of the substrate. For the future this problem can be overcome by exciting the graphitic flake with light of another energy or by tuning the band structure and therefore shifting the PL signal relative to Laser and Raman signal. For further experiments Micro-Raman spectroscopy is expected to become a very powerful tool to classify the flakes. In the context of the search for appropriate detection method, we discovered imaging ellipsometry together with the *Accurion* company as a nice tool to make graphene visible on any substrate material and to determine layer number.

Fortunately, the very intense search for possible methods to detect the atomic thin graphitic layers on arbitrary substrate materials leads to very valuable "spin-off products" resulting in one published manuscript [109] and one manuscript in preparation, actually.

Graphene can be prepared on different kind of substrates, namely (001)-GaAs, magnetic Mn p-doped GaAs and InGaAs. We found that the various electromagnetic substrate configurations of our substrates ranging from amorphous SiO<sub>2</sub> over polar (001) GaAs to p-doped GaMnAs do not affect the formation or stability of graphene. Investigations of the morphology by AFM demonstrates graphene to follow a continuous substrate texture from  $\sim 8$  nm to more than 1  $\mu$ m. To prepare individual alignment marks or electrical contacts to graphene an electron beam lithography step is needed. AFM images and their power spectral density analysis show that even with careful lift-off, this step leaves unwanted PMMA residues on the surface.

From extensive imaging ellipsometry studies, where a graphene monolayer on SiO<sub>2</sub> was measured angle and wavelength dependent, the optical dispersion relation was modeled with a comprehensive algorithm developed by *Accurion* company. This algorithm is based on the Drude model [143]. Both, the values for extinction and refraction indices for incident wavelength from 350 nm to 1000 nm increase with increasing wavelength. This is in contrast to the behavior for graphite, whose optical dispersion is rather small [144], what was also believed to be for graphene for long time [23,97]. Comparison the wavelength dependency from our data with picometrology results taken for three discrete wavelengths [113] are qualitatively in good agreement. The refractive index  $n$  shows similar wavelength dependence, whereas the extinction  $k$  obtained with IE exhibits a smaller wavelength dependency compared to the picometrology data.

Finally, magnetotransport measurements have been carried out on a couple of graphene mono-, bi- and few-layer graphene on GaAs, some on InGaAs and for comparison on SiO<sub>2</sub>. Hereby the charge neutrality point in dependence of the temperature was observable. Magnetotransport measurements at higher fields reveal signatures of quantized transport phenomena. From the hole slope and the  $1/B$  periodicity of the SdH oscillation the charge carrier density can be deduced. Interestingly we found that at low temperatures the type of intrinsic doping was p-type for all graphene samples on GaAs and InGaAs substrates. The charge carrier mobility in our sample was not very high, but comparable to those in identically prepared samples on SiO<sub>2</sub>. The mobility constitutes between  $\mu = 1660$  cm<sup>2</sup>/Vs

and  $\mu = 3600 \text{ cm}^2/\text{Vs}$ . Despite the charge injection parameter  $\alpha$  is higher for the GaAs based substrate compared to  $\text{SiO}_2$ , the breakthrough voltage was found to be only a few volt. Regrettably, this avoids the tunability of the charge carrier density over a larger area. In the whole magnetic field range and up to about  $T = 30 \text{ K}$  highly reproducible universal conductance fluctuations were detectable. From the weak localization found at low magnetic fields and up to more than  $T = 65 \text{ K}$ , the phase coherence length  $L_\Phi$  due to inelastic scattering, the elastic intravalley scattering length  $L_\star$  and the elastic intervalley scattering length  $L_i$  were calculated. All lengths reveal values comparable to those reported in literature and the maximal found coherence length was  $L_\Phi = 317 \text{ nm}$ . The temperature dependency of the lengths was as expected from measurements on  $\text{SiO}_2$ , whereas the dependency of the carrier density was unexpected. We found an aperiodical suppression of the WL signal by tuning the carrier density accompanied by lowering of all characteristic length. This feature was not found for graphene on  $\text{SiO}_2$  and the origin is still unclear.

To sum up, preparation and investigations including electrical measurements of graphene on precisely tailored crystalline III-As substrates is possible and enables hybrids of two exciting and meanwhile well known materials systems and the application of well established methods such as surface acoustic waves or rolling up of strained InGaAs/GaAs-hybrids into long microtubes. Besides the minimum conductivity and quantized transport phenomena, namely Shubnikov-de Haas oscillations and quantum Hall oscillation, intriguing and recent phase coherent transport phenomena were observable in magnetotransport experiments. The impact of the substrate material, especially of phonons, charged or magnetic impurities inside the substrate in close vicinity to graphene on the (surprising) weak localization effects are not yet clear. Continuative investigations will highlight the origin of these findings. Moreover, symmetry-breaking e.g. induced by sheet undulations due to surface corrugation of the substrate can induce spin-orbit coupling effects making graphene more interesting for spin-related effects.

Further improvement of high-quality graphene in large wafer sizes and the successful transfer to an arbitrarily substrate, invigorate the role of graphene in current and forthcoming research as well as possible applications. It is going to be exciting what path these materials of the superlatives, capable for food, microelectronics, micromechanics and optics will take.

# Appendix A

## Abbreviations

<b>AFM</b>	atomic force microscope	<b>PE</b>	primary electrons
<b>AOI</b>	angle of incidence	<b>PMMA</b>	polymethylmethacrylate
<b>BL</b>	bilayer	<b>PZT</b>	$Pb(Zr_{0.2}Ti_{0.8})O_3$
<b>BLG</b>	bilayer graphene	<b>QHE</b>	quantum Hall effect
<b>CNP</b>	charge neutrality point	<b>RIE</b>	reactive ion etching
<b>CVD</b>	chemical vapor deposition	<b>RMS</b>	root mean square
<b>EBL</b>	electron beam lithography	<b>ROI</b>	regions of interests
<b>FFT</b>	fast-Fourier transformation	<b>SdH</b>	Shubnikov-de Haas
<b>FLG</b>	few-layer graphene	<b>SE</b>	secondary electrons
<b>HOPG</b>	highly oriented pyrolytic graphite	<b>SEM</b>	scanning electron microscope
<b>IE</b>	imaging ellipsometry	<b>SOI</b>	spin-orbit interaction
<b>LHC</b>	Large Hadron Collider	<b>STM</b>	scanning tunneling microscope
<b>LL</b>	Landau level	<b>TEM</b>	transmission electron microscopy
<b>MBE</b>	molecular beam epitaxy	<b>UCF</b>	universal conductance fluctuations
<b>ML</b>	monolayer	<b>VTI</b>	variable temperature insert
<b>MLG</b>	monolayer graphene	<b>WL</b>	weak localization
<b>MR</b>	magnetoresistance	<b>XRD</b>	X-ray diffraction

# Appendix B

## Recipes

### Wafer protection

#### Coverage with ARP Resist

- 1<sup>st</sup> step: 800 rpm / 9 acc / 30 sec
- 2<sup>nd</sup> step: 500 rpm / 9 acc / 30 sec
- 5 min 90 °C hot-plate
- Keep in vacuum

### Gate processing

#### Optical Lithography

- 1<sup>st</sup> step: 2000 rpm
- 2<sup>nd</sup> step: 4000 rpm
- 7 minutes 90 °C hot-plate
- Exposure with optical microscope 1 minute with maximum intensity
- ~ 1 min in NaOH development

### Etching the dielectric layer

RIE etching for SiO<sub>2</sub> substrate:

- $\Phi[CHF_3] = 80$  sccm,  $\Phi[Ar] = 100$  sccm

- $p = 50$  mTorr
- $P = 300$  W
- $t = 8$  minutes

Wet chemical etching of the semiconducting substrates:

- $\text{H}_2\text{O} : \text{H}_2\text{O}_2 : \text{acetic acid} = 5 : 1 : 5$
- GaAs wafer: 6 min  $\Rightarrow$  1.6  $\mu\text{m}$
- InGaAs wafer: 9 min  $\Rightarrow$  2.4  $\mu\text{m}$

### Annealing of the gate contacts

- For  $\text{n}^+\text{Si}/\text{SiO}_2$  wafer:
  - Sputter cleaning in Univex with Argon (2 kV, 20 mA) for 30 seconds
  - Evaporate 5 nm Ti / 150 nm Au
  - Annealing for 20 minutes at  $450^\circ$  with forming gas pressure of  $\approx 300$  mbar
- For GaAs/InGaAs wafer:
  - Sputter cleaning in Univex with Argon (2 kV, 20 mA) for 30 seconds
  - Evaporate 25 nm Pd / 50 nm Ge
  - Annealing for 60 minutes at  $250^\circ$  with forming gas pressure of  $\approx 300$  mbar

## Electron beam lithography

### Parameters PMMA spin coating

- Step 1: 3000 rpm / 0 acc / 5 sec
- Step 2: 8000 rpm / 9 acc / 30 sec
- 3 drops after spinning start, 3 during acceleration to second step
- 5 min on  $150^\circ\text{C}$  hot-plate

## Resists and EBL parameters

Alignment marks:

- PMMA 200k, 3.5%
- Acceleration voltage: 25 kV
- Doses: SiO<sub>2</sub>:  $\sim 205\mu\text{C}$  | GaAs:  $\sim 205 - 215\mu\text{C}$  | InGaAs:  $\sim 200\mu\text{C}$
- Development: 1 minute MIBK/isopropanol (1/3), stopping 1 minute in isopropanol

Contacts to graphene/FLG layers with a double layer resist system:

- 1<sup>st</sup> layer: PMMA 200k, 7%
- 5 min on 150 °C hot-plate
- 5 minute cooling and hardening the 1<sup>st</sup> layer
- 2<sup>nd</sup> layer: PMMA 950k, 2%
- 5 min on 150 °C hot-plate
- 5 minute cooling and hardening the 2<sup>nd</sup> layer
- Acceleration voltage: 30 kV
- Doses: GaAs & InGaAs:  $\sim 285\mu\text{C}$
- Development: 20 seconds MIBK/isopropanol (1/3), stopping 40 seconds in isopropanol

## Metal evaporation - Univex:

Alignment marks:

- 30 sec Ar sputtering with 2 kV and  $\sim 20\text{mA}$
- Deposit 5 nm Ti
- Deposit 35 nm Au
- Lift-off: at least 15 minute in 60 °C warm acetone

Contacts to graphene/FLG layers:

- Evacuate Univex over night
- Deposit 40 nm Pd or 40 nm Au or Ti/Au (5 nm/40 nm) or Cr/Au (5 nm/40 nm)
- Lift-off: at least 1 hour in 60 °C warm acetone

**Removing and cleaning of samples after graphene deposition**

This step is optional and was only used if the sample surface contained a lot of graphite.

- Warm acetone bath (60 °C ) for  $\sim$  5 minutes
- clean with squirt of acetone
- one minute cleaning with isopropanol
- drying with nitrogen gas



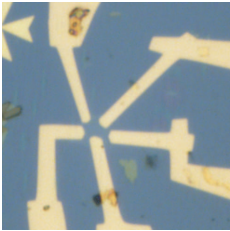


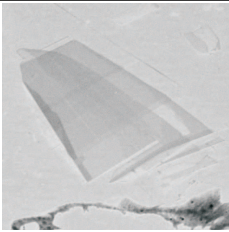

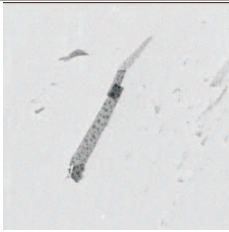
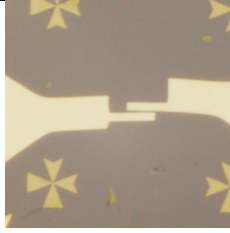
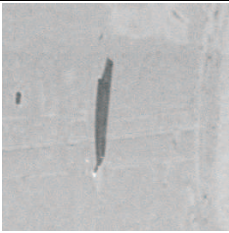

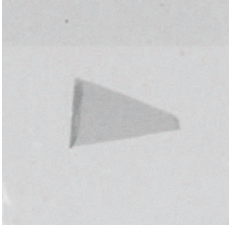
## Appendix C

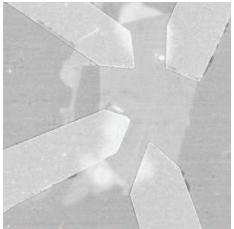
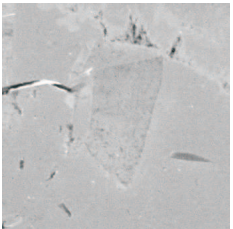
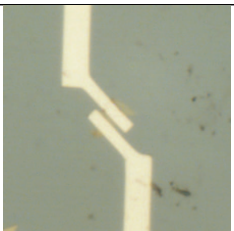
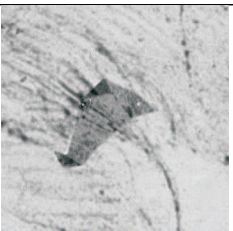
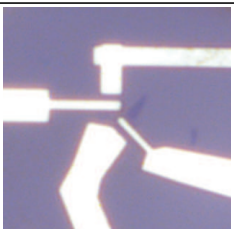

### Lists of wafers, samples and measurement equipment

#### List of available wafers

Type	Wafer	Layer sequence
GaAs	C070608A	200 nm GaAs Superlattice: 25 x 7 nm $\text{Al}_{0.75}\text{Ga}_{0.25}\text{As}$ & 3 nm GaAs 50 nm GaAs 10 nm $\text{Al}_{0.75}\text{Ga}_{0.25}\text{As}$ 55 nm GaAs 15 nm $\text{Al}_{0.75}\text{Ga}_{0.25}\text{As}$ 20 nm GaAs
InGaAs	C070709B	Superlattice: 10 x 7.5 nm $\text{Al}_{0.75}\text{Ga}_{0.25}\text{As}$ & 0.7 nm GaAs 32.6 nm GaAs InAlAs buffer: 27 x 50 nm; increase In content by 5% per step 38 nm $\text{In}_{0.75}\text{Al}_{0.25}\text{As}$ 10 nm $\text{In}_{0.75}\text{Ga}_{0.25}\text{As}$
$\text{SiO}_2$		<100> Si-wafer, $\text{n}^+$ doped 300 nm $\text{SiO}_2$
GaMnAs	C070502A	5 nm $\text{Al}_{0.78}\text{Ga}_{0.22}\text{As}$ 30 nm GaMnAs

**List of presented samples**

sample	contact layout	flake image
GaAs-BLG(b)		
GaAs-FLG(a)		
GaAs-MLG(a)		
GaAs-BLG(a)		
GaAs-MLG(b)		

InGaAs-BLG(a)		
InGaAs-FLG(a)		
SiO <sub>2</sub> -MLG(a) (Trilayer)		

## For magnetotransport measurements used equipment

DC characterization	<i>HP</i> Semiconductor Parameter Analyzer 4155A
Lock-In amplifiers	<i>SIGNAL RECOVERY</i> model 7265
DC Voltage source	<i>Yokogawa</i> DC source 7651
DC Voltage source	<i>KEITHLEY</i> 2400 source meter unit

# Bibliography

- [1] K. S. Novoselov, A. K. Geim, S. V. Morozov, D. Jiang, Y. Zhang, S. V. Dubonos, I. V. Grigorieva, A. A. Firsov: Electric Field Effect in Atomically Thin Carbon Films, *Science* **306**(5696), 666–669 (2004).
- [2] A. K. Geim, K. S. Novoselov: The rise of graphene, *Nature Materials* **6**(3), 183–191 March 2007.
- [3] K. S. Novoselov, A. K. Geim, S. V. Morozov, D. Jiang, M. I. Katsnelson, I. V. Grigorieva, S. V. Dubonos, A. A. Firsov: Two-dimensional gas of massless Dirac fermions in graphene, *Nature* **438**(7065), 197–200 (2005).
- [4] Y. Zhang, Y. Tan, H.L. Stormer, P. Kim: Experimental observation of the quantum Hall effect and Berry's phase in graphene, *Nature* **438**(7065), 201–204 November 2005.
- [5] A. C. Ferrari, J. C. Meyer, V. Scardaci, C. Casiraghi, M. Lazzeri, F. Mauri, S. Piscanec, D. Jiang, K. S. Novoselov, S. Roth, A. K. Geim: Raman Spectrum of Graphene and Graphene Layers, *Phys. Rev. Lett.* **97**(18), 187401 Oct 2006.
- [6] A. K. Geim, P. Kim: Carbon Wonderland, *Scientific American* **298**(4), 68–75 (2008).
- [7] Large Hadron Collider, Online published: <http://lhc.web.cern.ch/lhc/>, January 2010.
- [8] M. I. Katsnelson, K. S. Novoselov, A. K. Geim: Chiral tunnelling and the Klein paradox in graphene, *Nature Physics* **2**(9), 620–625 (2006).
- [9] A. F. Young, Philip Kim: Quantum interference and Klein tunnelling in graphene heterojunctions, *Nature Physics* **5**(3), 222–226 (2009).
- [10] M. I. Katsnelson: Graphene: carbon in two dimensions, *Materials Today* **10**(1-2), 20 – 27 (2007).

- [11] S. V. Morozov, K. S. Novoselov, F. Schedin, D. Jiang, A. A. Firsov, A. K. Geim: Two-dimensional electron and hole gases at the surface of graphite, *Phys. Rev. B* **72**(20), 201401 Nov 2005.
- [12] Y. Lin, K. A. Jenkins, A. Valdes-Garcia, J. P. Small, D. B. Farmer, P. Avouris: Operation of Graphene Transistors at Gigahertz Frequencies, *Nano Letters* **9**(1), 422–426 December 2009.
- [13] Y.-M. Lin, C. Dimitrakopoulos, K. A. Jenkins, D. B. Farmer, H.-Y. Chiu, A. Grill, Ph. Avouris: 100-GHz Transistors from Wafer-Scale Epitaxial Graphene, *Science* **327**(5966), 662– (2010).
- [14] A. K. Geim: Graphene: Status and Prospects, *Science* **324**(5934), 1530–1534 (2009).
- [15] G. E. Moore: Cramming more components onto integrated circuits, *Electronics* **38**(8) April 1965.
- [16] Y. M. Zuev, W. Chang, P. Kim: Thermoelectric and Magnetothermoelectric Transport Measurements of Graphene, *Phys. Rev. Lett.* **102**(9), 096807 Mar 2009.
- [17] P. R. Wallace: The Band Theory of Graphite, *Phys. Rev.* **71**(9), 622–634 May 1947.
- [18] E. H. Hwang, S. Das Sarma: Acoustic phonon scattering limited carrier mobility in two-dimensional extrinsic graphene, *Phys. Rev. B* **77**(11), 115449 Mar 2008.
- [19] S. V. Morozov, K. S. Novoselov, M. I. Katsnelson, F. Schedin, D. C. Elias, J. A. Jaszczak, A. K. Geim: Giant Intrinsic Carrier Mobilities in Graphene and Its Bilayer, *Phys. Rev. Lett.* **100**(1), 016602 Jan 2008.
- [20] K. I. Bolotin, K. J. Sikes, Z. Jiang, M. Klima, G. Fudenberg, J. Hone, P. Kim, H. L. Stormer: Ultrahigh electron mobility in suspended graphene, *Solid State Communications* **146**(9-10), 351 – 355 (2008).
- [21] X. Du, I. Skachko, A. Barker, E. Y. Andrei: Approaching ballistic transport in suspended graphene, *Nature Nanotechnology* **3**(8), 491–495 (2008).
- [22] X. Hong, A. Posadas, K. Zou, C. H. Ahn, J. Zhu: High-Mobility Few-Layer Graphene Field Effect Transistors Fabricated on Epitaxial Ferroelectric Gate Oxides, *Phys. Rev. Lett.* **102**(13), 136808 Apr 2009.
- [23] P. Blake, E. W. Hill, A. H. Castro Neto, K. S. Novoselov, D. Jiang, R. Yang, T. J. Booth, A. K. Geim: Making graphene visible, *Applied Physics Letters* **91**(6), 063124 (2007).

- [24] J.-H. Chen, C. Jang, S. Adam, M. S. Fuhrer, E. D. Williams, M. Ishigami: Charged-impurity scattering in graphene, *Nature Physics* **4**(5), 377–381 (2008).
- [25] J. Sabio, C. Seoáñez, S. Fratini, F. Guinea, A. H. Castro Neto, F. Sols: Electrostatic interactions between graphene layers and their environment, *Phys. Rev. B* **77**(19), 195409 May 2008.
- [26] Z. I. Alferov: Nobel Lecture: The double heterostructure concept and its applications in physics, electronics, and technology, *Rev. Mod. Phys.* **73**(3), 767–782 Oct 2001.
- [27] I. Calizo, W. Bao, W. Miao, C. N. Lau, A. A. Balandin: The effect of substrates on the Raman spectrum of graphene: Graphene- on-sapphire and graphene-on-glass, *Applied Physics Letters* **91**(20), 201904 (2007).
- [28] M. Friedemann, K. Pierz, R. Stosch, F. J. Ahlers: Graphene on gallium arsenide: Engineering the visibility, *Applied Physics Letters* **95**(10), 102103 (2009).
- [29] P. Vogl: Lecture notes "Theoretical Solid State Physics - Summer term 2004", Physik Department - TU München, April 2004.
- [30] Eight Allotropes of Carbon, Online published: [http://de.wikipedia.org/w/index.php?title=Datei:Eight\\_Allotropes\\_of\\_Carbon.png&filetimestamp=20080511205146](http://de.wikipedia.org/w/index.php?title=Datei:Eight_Allotropes_of_Carbon.png&filetimestamp=20080511205146), January 2010.
- [31] R. Saito, G. Dresselhaus, M.S. Dresselhaus: *Physical Properties of Carbon Nanotubes*, Imperial College Press, 1999.
- [32] A. H. Castro Neto, F. Guinea, N. M. R. Peres, K. S. Novoselov, A. K. Geim: The electronic properties of graphene, *Rev. Mod. Phys.* **81**(1), 109–162 Jan 2009.
- [33] J. W. McClure: Diamagnetism of Graphite, *Phys. Rev.* **104**(3), 666–671 Nov 1956.
- [34] J. C. Slonczewski, P. R. Weiss: Band Structure of Graphite, *Phys. Rev.* **109**(2), 272–279 Jan 1958.
- [35] C. L. Lu, C. P. Chang, Y. C. Huang, R. B. Chen, M. L. Lin: Influence of an electric field on the optical properties of few-layer graphene with AB stacking, *Phys. Rev. B* **73**(14), 144427 Apr 2006.
- [36] M. F. Craciun, S. Russo, M. Yamamoto, J. B. Oostinga, A. F. Morpurgo, S. Tarucha: Trilayer graphene is a semimetal with a gate-tunable band overlap, *Nature Nanotechnology* **4**(6), 383–388 June 2009.
- [37] F. Guinea, A. H. Castro Neto, N. M. R. Peres: Electronic states and Landau levels in graphene stacks, *Phys. Rev. B* **73**(24), 245426 Jun 2006.

- [38] Sylvain Latil, Luc Henrard: Charge Carriers in Few-Layer Graphene Films, *Phys. Rev. Lett.* **97**(3), 036803 Jul 2006.
- [39] B. Partoens, F. M. Peeters: From graphene to graphite: Electronic structure around the  $K$  point, *Phys. Rev. B* **74**(7), 075404 Aug 2006.
- [40] M. Aoki, H. Amawashia: Dependence of band structures on stacking and field in layered graphene, *Solid State Communications* **142**(3), 123–127 April 2007.
- [41] M. I. Katsnelson: Zitterbewegung, chirality, and minimal conductivity in graphene, *Eur. Phys. J. B* **51**(2), 157–160 May 2006.
- [42] J. Tworzydło, B. Trauzettel, M. Titov, A. Rycerz, C. W. J. Beenakker: Sub-Poissonian Shot Noise in Graphene, *Phys. Rev. Lett.* **96**(24), 246802 Jun 2006.
- [43] K. S. Novoselov, E. McCann, S. V. Morozov, V. I. Fal'ko, M. I. Katsnelson, U. Zeitler, D. Jiang, F. Schedin, A. K. Geim: Unconventional quantum Hall effect and Berry's phase of  $2\pi$  in bilayer graphene, *Nature Physics* **2**(3), 177–180 (2006).
- [44] K. v. Klitzing, G. Dorda, M. Pepper: New Method for High-Accuracy Determination of the Fine-Structure Constant Based on Quantized Hall Resistance, *Phys. Rev. Lett.* **45**(6), 494–497 Aug 1980.
- [45] D. Graf: Electrons in reduced dimensions - from finite lateral superlattices in AlGaAs heterostructures to few-layer graphene, Dissertation, Eidgenössische Technische Hochschule ETH Zürich, 2007.
- [46] D. Weiss, W. Wegscheider: Lecture notes "Halbleiterphysik", 2006.
- [47] K. S. Novoselov, Z. Jiang, Y. Zhang, S. V. Morozov, H. L. Stormer, U. Zeitler, J. C. Maan, G. S. Boebinger, P. Kim, A. K. Geim: Room-Temperature Quantum Hall Effect in Graphene, *Science* **315**(5817), 1379– (2007).
- [48] S. Datta: *Electronic Transport in Mesoscopic Systems* (Cambridge Studies in Semiconductor Physics and Microelectronic Engineering), Cambridge University Press, 1995.
- [49] H. Ehrenreich, D. Turnbull, editors: *SOLID STATE PHYSICS - Advances in Research and Applications*, Academic Press, 1991.
- [50] K. Wagner: Transportuntersuchungen von Quanteninterferenzeffekten in ferromagnetischen (Ga,Mn)As Nanostrukturen, Dissertation, Universität Regensburg Universitätsstraße, 93042 Regensburg, 2007.

- [51] D. Neumaier: Schwache Lokalisierung und andere Interferenzeffekte in Ferromagneten, Dissertation, Universität Regensburg Universitätsstraße, 93042 Regensburg, 2008.
- [52] B. L. Altshuler, D. Khmel'nitzkii, A. I. Larkin, P. A. Lee: Magnetoresistance and Hall effect in a disordered two-dimensional electron gas, *Phys. Rev. B* **22**(11), 5142–5153 Dec 1980.
- [53] F. V. Tikhonenko, D. W. Horsell, R. V. Gorbachev, A. K. Savchenko: Weak Localization in Graphene Flakes, *Phys. Rev. Lett.* **100**(5), 056802 Feb 2008.
- [54] R. V. Gorbachev, F. V. Tikhonenko, A. S. Mayorov, D. W. Horsell, A. K. Savchenko: Weak Localization in Bilayer Graphene, *Phys. Rev. Lett.* **98**(17), 176805 Apr 2007.
- [55] E. McCann, K. Kechedzhi, Vladimir I. Fal'ko, H. Suzuura, T. Ando, B. L. Altshuler: Weak-Localization Magnetoresistance and Valley Symmetry in Graphene, *Phys. Rev. Lett.* **97**(14), 146805 Oct 2006.
- [56] K. Kechedzhi, Vladimir I. Fal'ko, E. McCann, B. L. Altshuler: Influence of Trigonal Warping on Interference Effects in Bilayer Graphene, *Phys. Rev. Lett.* **98**(17), 176806 Apr 2007.
- [57] F. V. Tikhonenko, A. A. Kozikov, A. K. Savchenko, R. V. Gorbachev: Transition between Electron Localization and Antilocalization in Graphene, *Phys. Rev. Lett.* **103**(22), 226801 Nov 2009.
- [58] Carl Zeiss SMT, SUPRA Series with GEMINI Column, Handout at Zeiss Gemini User meeting, May 2004.
- [59] U. Stöberl: Präparation und Charakterisierung von Graphen-Schichten auf Siliziumdioxid, Diploma thesis, Universität Regensburg, 2007.
- [60] G. Binnig, C. F. Quate, Ch. Gerber: Atomic Force Microscope, *Phys. Rev. Lett.* **56**(9), 930–933 Mar 1986.
- [61] G. Binnig, H. Rohrer, Ch. Gerber, E. Weibel: Surface Studies by Scanning Tunneling Microscopy, *Phys. Rev. Lett.* **49**(1), 57–61 Jul 1982.
- [62] F. J. Giessibl: Advances in atomic force microscopy, *Rev. Mod. Phys.* **75**(3), 949–983 Jul 2003.
- [63] B. Cappella, G. Dietler: Force-distance curves by atomic force microscopy, *Surface Science Reports* **34**(1-3), 1–104 November 1999.



- [64] R. García, R. Pérez: Dynamic atomic force microscopy methods, *Surface Science Reports* **47**(6-8), 197–301 September 2002.
- [65] R. Pulwey: Magnetkraftmikroskopie an polykristallinen und epitaktischen Nanomagneten, Dissertation, Universität Regensburg Universitätsstraße, 93042 Regensburg, 2007.
- [66] P. Drude: *Lehrbuch der Optik*, 2. Aufl., 1900.
- [67] Optical Society Of America: *Handbook of Optics*, Vol. 2: Devices, Measurements, and Properties, Second Edition, 2 Aufl., McGraw-Hill Professional, September 1994.
- [68] Compendium - Principles of Nulling and Imaging Ellipsometry, Information for download <http://www accurion.de>, December 2009.
- [69] P. S. Hauge: Recent developments in instrumentation in ellipsometry, *Surface Science* **96**(1-3), 108 – 140 (1980).
- [70] I. Jung, M. Vaupel, M. Pelton, R. Piner, D. A. Dikin, S. Stankovich, J. An, R. S. Ruoff: Characterization of Thermally Reduced Graphene Oxide by Imaging Ellipsometry, *J. Phys. Chem. C* **112**(23), 8499–8506 May 2008.
- [71] J. Bauer: Transporteigenschaften Zweidimensionaler Lochsysteme, Diploma thesis, Universität Regensburg, 2006.
- [72] T. Feil: Magnetotransportuntersuchungen an zweidimensionalen Systemen im ballistischen Regime, Dissertation, Universität Regensburg Universitätsstraße, 93042 Regensburg, 2008.
- [73] L. D. Landau: Zur Theorie der Phasenumwandlungen II, *Phys. Z. Sowjetunion* (11), 26–35 (1937).
- [74] R. E. Peierls: Quelques proprietes typiques des corps solides, *Ann. I. H. Poincare* (5), 177–222 (1935).
- [75] M. J. Allen, V. C. Tung, R. B. Kaner: Honeycomb Carbon: A Review of Graphene, *Chemical Reviews* (2009).
- [76] C. Berger, Z. Song, T. Li, X. Li, A.Y. Ogbazghi, R. Feng, Z. Dai, A.N. Marchenkov, E.H. Conrad, P.N. First, W.A. de Heer: Ultrathin Epitaxial Graphite: 2D Electron Gas Properties and a Route towards Graphene-based Nanoelectronics, *J. Phys. Chem. B* **108**(52), 19912–19916 December 2004.

- [77] Th. Seyller, K.V. Emtsev, K. Gao, F. Speck, L. Ley, A. Tadich, L. Broekman, J.D. Riley, R.C.G. Leckey, O. Rader, A. Varykhalov, A.M. Shikin: Structural and electronic properties of graphite layers grown on SiC(0 0 0 1), *Surface Science* **600**(18), 3906 – 3911 (2006), Berlin, Germany: 4-9 September 2005, Proceedings of the 23th European Conference on Surface Science.
- [78] K. V. Emtsev, A. Bostwick, K. Horn, J. Jobst, G. L. Kellogg, L. Ley, J. L. Mcchesney, T. Ohta, S. A. Reshanov, J. Rohrl, E. Rotenberg, A. K. Schmid, D. Waldmann, H. B. Weber, T. Seyller: Towards wafer-size graphene layers by atmospheric pressure graphitization of silicon carbide, *Nature Materials* **8**(3), 203–207 March 2009.
- [79] A. Oshima, A. Nagashima: Ultra-thin epitaxial films of graphite and hexagonal boron nitride on solid surfaces, *Journal of Physics: Condensed Matter* **9**(1), 1–20 (1997).
- [80] X. Li, W. Cai, J. An, S. Kim, J. Nah, D. Yang, R. Piner, A. Velamakanni, I. Jung, E. Tutuc, S. K. Banerjee, L. Colombo, R. S. Ruoff: Large-Area Synthesis of High-Quality and Uniform Graphene Films on Copper Foils, *Science* **324**(5932), 1312–1314 (2009).
- [81] A. Reina, X. Jia, J. Ho, D. Nezich, H. Son, V. Bulovic, M. S. Dresselhaus, J. Kong: Large Area, Few-Layer Graphene Films on Arbitrary Substrates by Chemical Vapor Deposition, *Nano Letters* **9**(1), 30–35 (2009).
- [82] K. S. Kim, Y. Zhao, H. Jang, S. Y. Lee, J. M. Kim, K. S. Kim, J.-H. Ahn, P. Kim, J.-Y. Choi, B. H. Hong: Large-scale pattern growth of graphene films for stretchable transparent electrodes, *Nature* **457**(7230), 706–710 (2009).
- [83] S. Bae, H. K. Kim, X. Xu, J. Balakrishnan, T. Lei, Y. I. Song, Y. J. Kim, B. Ozyilmaz, J.-H. Ahn, B. H. Hong, S. Iijima: 30-Inch Roll-Based Production of High-Quality Graphene Films for Flexible Transparent Electrodes, *ArXiv cond-mat* (0912.5485) December 2009.
- [84] G. Giovannetti, P. A. Khomyakov, G. Brocks, P. J. Kelly, J. van den Brink: Substrate-induced band gap in graphene on hexagonal boron nitride: Ab initio density functional calculations, *Phys. Rev. B* **76**(7), 073103 Aug 2007.
- [85] T. A. G. Eberlein, R. Jones, J. P. Goss, P. R. Briddon: Doping of graphene: Density functional calculations of charge transfer between GaAs and carbon nanostructures, *Phys. Rev. B* **78**(4), 045403 Jul 2008.
- [86] Y. Mao, J. Zhong: Structural, electronic and magnetic properties of manganese doping in the upper layer of bilayer graphene, *Nanotechnology* **19**(20), 205708 (8pp) (2008).

- [87] I. Calizo, D. Teweldebrhan, W. Bao, F. Miao, C. N. Lau, A. A. Balandin: Spectroscopic raman nanometrology of graphene and graphene multilayers on arbitrary substrates, *Journal of Physics: Conference Series* **109**, 012008 (4pp) (2008).
- [88] U. Wurstbauer: Herstellung und Charakterisierung von Mangan dotierten III-V Halbleiterheterostrukturen, Dissertation, Universität Regensburg Universitätsstraße, 93042 Regensburg, 2008.
- [89] A. K. Geim, A. H. MacDonald: Graphene: Exploring Carbon Flatland, *Physics Today* **60**(8), 35–41 (2007).
- [90] L.J. van der Pauw: A Method of Measuring Specific Resistivity and Hall Effect of Discs of Arbitrary Shape, *Philips Res. Rep.* **13**(1) (1958).
- [91] D. Schuh: Mikro-Hall-Magnetometrie, Dissertation, Universität Regensburg, 2000, ISBN 978-3-89722-560-2.
- [92] J. Biberger: Transportphänomene in mesoskopischen 2DEG-Strukturen unter dem Einfluss inhomogener Streufelder von Nanomagnetten, Dissertation, Universität Regensburg Universitätsstraße, 93042 Regensburg, 2007.
- [93] Z. H. Ni, H. M. Wang, J. Kasim, H. M. Fan, T. Yu, Y. H. Wu, Y. P. Feng, Z. X. Shen: Graphene Thickness Determination Using Reflection and Contrast Spectroscopy, *Nano Letters* **7**(9), 2758–2763 (2007).
- [94] X. Wang, M. Zhao, D. D. Nolte: Optical contrast and clarity of graphene on an arbitrary substrate, *Applied Physics Letters* **95**(8), 081102 (2009).
- [95] D. S. L. Abergel, A. Russell, V. I. Fal'ko: Visibility of graphene flakes on a dielectric substrate, *Applied Physics Letters* **91**(6), 063125 (2007).
- [96] G. Teo, H. Wang, Y. Wu, Z. Guo, J. Zhang, Z. Ni, Z. Shen: Visibility study of graphene multilayer structures, *Journal of Applied Physics* **103**(12), 124302 (2008).
- [97] M. Bruna, S. Borini: Optical constants of graphene layers in the visible range, *Applied Physics Letters* **94**(3), 031901 (2009).
- [98] J. Eroms, D. Weiss: Weak localization and transport gap in graphene antidot lattices, *New Journal of Physics* **11**(9), 095021 (9pp) (2009).
- [99] D. Teweldebrhan, A. A. Balandin: Modification of graphene properties due to electron-beam irradiation, *Applied Physics Letters* **94**(1), 013101 (2009).
- [100] P. Kim, personal communication, December 2009.

- [101] A. Einwanger: Investigations on Ferromagnetic (Ga,Mn)As Contacts, Diploma thesis, Universität Regensburg, 2006.
- [102] P. Debije, P. Scherrer: Interferenz an regellos orientierten Teilchen im Röntgenlicht I, *Physikalische Zeitschrift* **17**, 277–283 (1916).
- [103] J. D. Bernal: The Structure of Graphite, *Proceedings of the Royal Society of London. Series A* **106**(740), 749–773 (1924).
- [104] O. Hassel, H. Mark: Über die Kristallstruktur des Graphits, *Zeitschrift für Physik A Hadrons and Nuclei* **25**(1), 317–337 (1924).
- [105] T. Tsukamoto, T. Ogino: Morphology of Graphene on Step-Controlled Sapphire Surfaces, *Applied Physics Express* **2**(7), 075502 (2009).
- [106] C. H. Lui, L. Liu, K. F. Mak, G. W. Flynn, T. F. Heinz: Ultraflat graphene, *Nature* **462**(7271), 339–341 (2009).
- [107] P. Nemes-Incze, Z. Osváth, K. Kamarás, L. P. Biró: Anomalies in thickness measurements of graphene and few layer graphite crystals by tapping mode atomic force microscopy, *Carbon* **45**(11), 1435–1442 September 2008.
- [108] M. Ishigami, J. H. Chen, W. G. Cullen, M. S. Fuhrer, E. D. Williams: Atomic Structure of Graphene on SiO<sub>2</sub>, *Nano Letters* **7**(6), 1643–1648 (2007).
- [109] U. Stöberl, U. Wurstbauer, W. Wegscheider, D. Weiss, J. Eroms: Morphology and flexibility of graphene and few-layer graphene on various substrates, *Applied Physics Letters* **93**(5), 051906 (2008).
- [110] Y. Y. Wang, Z. H. Ni, T. Yu, Z. X. Shen, H. M. Wang, Y. H. Wu, W. Chen, A. T. Shen Wee: Raman Studies of Monolayer Graphene: The Substrate Effect, *The Journal of Physical Chemistry C* **112**(29), 10637–10640 (2008).
- [111] D. Graf, F. Molitor, K. Ensslin, C. Stampfer, A. Jungen, C. Hierold, L. Wirtz: Spatially Resolved Raman Spectroscopy of Single- and Few-Layer Graphene, *Nano Letters* **7**(2), 238–242 (2007).
- [112] M. Hiermer, personal communication, September 2009.
- [113] X. Wang, Y. P. Chen, D. D. Nolte: Strong anomalous optical dispersion of graphene: complex refractive index measured by Picometrology, *Opt. Express* **16**(26), 22105–22112 (2008).
- [114] J. S. Bunch, A. M. van der Zande, S. S. Verbridge, I. W. Frank, D. M. Tanenbaum, J. M. Parpia, H. G. Craighead, P. L. McEuen: Electromechanical Resonators from Graphene Sheets, *Science* **315**(5811), 490–493 (2007).

- [115] I. W. Frank, D. M. Tanenbaum, A. M. van der Zande, P. L. McEuen: Mechanical properties of suspended graphene sheets, *J. Vac. Sci. Technol. B* **25**(6), 2558–2561 (2007).
- [116] D. Garcia-Sanchez, A. M. van der Zande, A. San Paulo, B. Lassagne, P. L. McEuen, A. Bachtold: Imaging Mechanical Vibrations in Suspended Graphene Sheets, *Nano Letters* **8**(5), 1399–1403 (2008).
- [117] C. Lee, X. Wei, J. W. Kysar, J. Hone: Measurement of the Elastic Properties and Intrinsic Strength of Monolayer Graphene, *Science* **321**(5887), 385–388 (2008).
- [118] J. C. Meyer, A. K. Geim, M. I. Katsnelson, K. S. Novoselov, T. J. Booth, S. Roth: The structure of suspended graphene sheets, *Nature* **446**(7131), 60–63 March 2007.
- [119] J. C. Meyer, A. K. Geim, M. I. Katsnelson, K. S. Novoselov, D. Obergfell, S. Roth, C. Girit, A. Zettl: On the roughness of single- and bi-layer graphene membranes, *Solid State Communications* **143**(1-2), 101 – 109 (2007).
- [120] F. Schedin, A. K. Geim, S. V. Morozov, E. W. Hill, P. Blake, M. I. Katsnelson, K. S. Novoselov: Detection of individual gas molecules adsorbed on graphene, *Nature Materials* **6**(9), 652–655 (2007).
- [121] Daniel Huertas-Hernando, F. Guinea, Arne Brataas: Spin-orbit coupling in curved graphene, fullerenes, nanotubes, and nanotube caps, *Phys. Rev. B* **74**(15), 155426 Oct 2006.
- [122] D. Huertas-Hernando, F. Guinea, A. Brataas: Spin relaxation times in disordered graphene, *The European Physical Journal - Special Topics* **148**(1), 177–181 (2007).
- [123] T. Kato, S. Onari, J. Inoue: Spin Hall effect in a curved graphene with spin-orbit interaction, *Physica E: Low-dimensional Systems and Nanostructures* page DOI:10.1016/j.physe.2009.11.132 (2009).
- [124] M. B. Lundeberg, J. A. Folk: Spin-resolved quantum interference in graphene, *Nature Physics* **5**(12), 894–897 (2009).
- [125] J. Moser, A. Verdaguer, D. Jiménez, A. Barreiro, A. Bachtold: The environment of graphene probed by electrostatic force microscopy, *Applied Physics Letters* **92**(12), 123507 (2008).
- [126] N. D. Mermin: Crystalline Order in Two Dimensions, *Phys. Rev.* **176**(1), 250–254 Dec 1968.

- [127] K. S. Novoselov, D. Jiang, F. Schedin, T.J. Booth, V.V. Khotkevicha, S.V. Morozov, A.K. Geim: Two-dimensional atomic crystals, *PNAS* **102**(30), 10451–10453 July 2005.
- [128] Y. Zhang, V. W. Brar, F. Wang, C. Girit, Y. Yayon, M. Panlasigui, A. Zettl, M. F. Crommie: Giant phonon-induced conductance in scanning tunnelling spectroscopy of gate-tunable graphene, *Nature Physics* **4**(8), 627–630 (2008).
- [129] E.-A. Kim, A. H. Castro Neto: Graphene as an electronic membrane, *EPL (Europhysics Letters)* **84**(5), 57007 (5pp) (2008).
- [130] T. Yu, C. Ni, Z. Du, Y. You, Y. Wang, Z. Shen: Raman Mapping Investigation of Graphene on Transparent Flexible Substrate: The Strain Effect, *The Journal of Physical Chemistry C* **112**(33), 12602–12605 (2008).
- [131] T. M. G. Mohiuddin, A. Lombardo, R. R. Nair, A. Bonetti, G. Savini, R. Jalil, N. Bonini, D. M. Basko, C. Galiotis, N. Marzari, K. S. Novoselov, A. K. Geim, A. C. Ferrari: Uniaxial strain in graphene by Raman spectroscopy: *G* peak splitting, Grüneisen parameters, and sample orientation, *Phys. Rev. B* **79**(20), 205433 May 2009.
- [132] H. G. Tompkins, E. A. Irene, editors: *Handbook of Ellipsometry*, William Andrew Publishing/Noyes, 2005.
- [133] V. I. Fal'ko, personal communication, January 2010.
- [134] M. Shinohara, T. Ito, K. Wada, Y. Imamura: Electrical Properties of Oval Defects in GaAs Grown by MBE, *Japanese Journal of Applied Physics* **23**(Part 2, No. 6), L371–L373 (1984).
- [135] G. M. Metze, A. R. Calawa, J. G. Mavroides: An investigation of GaAs films grown by MBE at low substrate temperatures and growth rates, *Journal of Vacuum Science and Technology B: Microelectronics and Nanometer Structures* **1**(2), 166–169 (1983).
- [136] N. J. Kadhim, D. Mukherjee: SEM and EPMA studies of oval defects on MBE GaAs layers, *Journal of Materials Science Letters* **17**(7), 595–597 (1998).
- [137] J. Martin, N. Akerman, G. Ulbricht, T. Lohmann, J. H. Smet, K. von Klitzing, A. Yacoby: Observation of electron-hole puddles in graphene using a scanning single-electron transistor, *Nature Physics* **4**(2), 144–148 (2008).
- [138] B. Birkner: Spininjektion in Graphen, Diploma thesis, Universität Regensburg, 2009.

- [139] S. V. Morozov, K. S. Novoselov, M. I. Katsnelson, F. Schedin, L. A. Ponomarenko, D. Jiang, A. K. Geim: Strong Suppression of Weak Localization in Graphene, *Phys. Rev. Lett.* **97**(1), 016801 Jul 2006.
- [140] T. Ihn, D. Graf, F. Molitor, C. Stampfer, K. Ensslin: Phase-coherent transport in a mesoscopic few-layer graphite wire, *Physica E: Low-dimensional Systems and Nanostructures* **40**(6), 1851 – 1854 (2008), 13th International Conference on Modulated Semiconductor Structures.
- [141] K. K. Choi, D. C. Tsui, S. C. Palmateer: Electron-electron interactions in GaAs- $Al_xGa_{1-x}$ As heterostructures, *Phys. Rev. B* **33**(12), 8216–8227 Jun 1986.
- [142] M. Monteverde, C. Ojeda-Aristizabal, R. Weil, M. Ferrier, S. Gueron, Bouchiat H, J. N. Fuchs, D. L. Maslov: Transport and elastic scattering times as probes of the nature of impurity scattering in single and bilayer graphene, *arXiv:0903.3285v3* (2009).
- [143] M. Vaupel, personal communication, 2008.
- [144] E. D. Palik: *Handbook of Optical Constants of Solids*, Academic Press Inc, 2007.
- [145] C. Casiraghi, A. Hartschuh, E. Lidorikis, H. Qian, H. Harutyunyan, T. Gokus, K. S. Novoselov, A. C. Ferrari: Rayleigh Imaging of Graphene and Graphene Layers, *Nano Letters* **7**(9), 2711–2717 (2007).
- [146] D. A. Dikin, S. Stankovich, E. J. Zimney, R. D. Piner, G. H. B. Dommett, G. Evmenenko, S. T. Nguyen, R. S. Ruoff: Preparation and characterization of graphene oxide paper, *Nature* **448**(7152), 457–460 July 2007.
- [147] C. Ertler, S. Konschuh, M. Gmitra, J. Fabian: Electron spin relaxation in graphene: The role of the substrate, *Phys. Rev. B* **80**(4), 041405 Jul 2009.
- [148] P. E. Gaskell, H. S. Skulason, C. Rodenchuk, T. Szkopek: Counting graphene layers on glass via optical reflection microscopy, *Applied Physics Letters* **94**(14), 143101 (2009).
- [149] Y. Hernandez, V. Nicolosi, M. Lotya, F. M. Blighe, Z. Sun, S. De, I. T. McGovern, B. Holland, M. Byrne, Y. K. Gun'Ko, J. J. Boland, P. Niraj, G. Duesberg, S. Krishnamurthy, R. Goodhue, J. Hutchison, V. Scardaci, A. C. Ferrari, J. N. Coleman: High-yield production of graphene by liquid-phase exfoliation of graphite, *Nature Nanotechnology* **3**(9), 563–568 August 2008.

- 
- [150] L. A. Ponomarenko, R. Yang, T. M. Mohiuddin, M. I. Katsnelson, K. S. Novoselov, S. V. Morozov, A. A. Zhukov, F. Schedin, E. W. Hill, A. K. Geim: Effect of a High- $\kappa$  Environment on Charge Carrier Mobility in Graphene, *Phys. Rev. Lett.* **102**(20), 206603 May 2009.
- [151] C. Valle's, C. Drummond, H. Saadaoui, C. A. Furtado, M. He, O. Roubeau, L. Ortolani, M. Monthieux, A. Pe'nicaud: Solutions of Negatively Charged Graphene Sheets and Ribbons, *Journal of the American Chemical Society* **130**(47), 15802–15804 (2008).



# Vielen vielen Dank...

Ohne die vielfältige Hilfe die mir von allen Seiten zuteil wurde, wäre diese Arbeit unmöglich gewesen. Für all das möchte ich mich herzlichst bedanken! Mein besonderer Dank geht an

Prof. Dieter Weiss für die Offenheit und Bereitschaft diesem Thema gegenüber, die stete Ansprechbarkeit und die Freiräume, die ich erhielt. Sie ermöglichten erst den einen oder anderen Exkurs und trugen wesentlich zum Facettenreichtum der Arbeit bei. Zudem konnte ich meine eigenen Erfahrungen machen, gleichzeitig erhielt ich stets Absicherung und Rückendeckung, wofür ich sehr dankbar bin!

Prof. Franz J. Gießibl danke ich sehr, für hilfreiche Erklärungen die Rasterkraftmikroskopie betreffend. Das zusammen mit seinen aufgeschlossenen Mitarbeiter half oft, "Laborfrust" mit Distanz zu betrachten. Vielen Dank auch für die unkomplizierte Zusage als Zweitgutachter zu fungieren.

Externe Kooperationen und gemeinsame Messtage waren stets das Salz in der Suppe dieser Arbeit, dafür danke ich zum einem Dr. Matthias Vaupel, der mich schnell (manchmal zu schnell) in die abbildende Ellipsometrie einführte und zusammen mit Dr. Peter Thiesen und Christian Röling, die die Messresultate der optischen Eigenschaften maßgeblich erzeugten. Die Interpretation hat und wird weiterhin im engen Austausch stattfinden. Ebenso war die Durchführung erster SAW Experimente eine mehr als interessante Erfahrung - für die Ideen, Hilfestellungen, Erklärungen und die offene und sehr unkomplizierte Art sag ich Prof. Jens Ebbecke ein herzliches Dankeschön!

Einen Dank auch an Jonathan Eroms für so manche anregende Diskussion, auch wenn Sie nicht immer mit einem Konsens endete.

Wie viel Kraft, Zeit und Energie mir durch die folgenden Leute erspart wurde, kann ich nicht sagen, was ich aber weiß ist, dass ohne sie manches deutlich erschwert worden wäre: Allen voran unsere beiden Sekretärinnen - liebe Elke, liebe Claudia, ich hab immer bewundert wie perfekt Ihr zusammenarbeitet und Euch ergänzt! Ihr wusstet einfach immer Bescheid, Euch war keine Mühe zu groß und Ihr hattet auch noch offene Ohren für ein persönliches Wort - Danke! Selbiges gilt auch für Ulla Turba, die alle GK-Angelegenheiten stets mit einem Lächeln und meist in Sekunden erledigte.

Vielen Dank sag ich auch an die "coolen Jungs": Thomas und Christian. Ihr hattet (woher auch immer) irgendwie immer noch ein Könnchen Helium in der Reserve und habt auch

augenzwinkernd eine versehentlich noch gefüllte Heliumkanne wieder angenommen. Vieles sieht, lernt und erkennt man oft nur nebenbei, der Austausch und das Gespräch mit Kollegen machte (fast) immer Spaß und gewährte viele neue Einblicke. Als erstes möchte ich allen aktuellen und ehemaligen Kollegen des Lehrstuhls Weiss danken, ausdrücklich seien auch die Kollegen der AG Strunk erwähnt, die mir stets mehr als offen begegneten! Namentlich erwähnt seien: Silvia und Basti, die Freud und Leid einer Graphene-Doktorarbeit selbst am Besten einordnen können, Andi stellte nicht nur einen perfekten Admin dar, sondern wusste auch über so ziemlich jedes mögliche Reinraumrezept Bescheid - mit niemanden diskutierte ich lieber wer von uns beiden am Abend ans REM kann als mit Dir. Sepp und Tobias sag ich vielen Dank für das Wissen an dem Ihr mich von Anbeginn als Diplomand und später als Kollege teilhaben habt lassen!

Renate, Imke, Sigi und Didi danke ich sehr für viele schöne, unterhaltsame und interessante Gespräche und Einblicke wie's an einem anderen Lehrstuhl läuft. Markus, Tom, Lorenz und Sung-Ho danke ich für interessante und aufmunternde Gespräche und das eine oder andere was ich von Euch über aufgerollte Graphene-Schichten lernen durfte. Allen Bürokollegen danke ich für die Ruhe, die konzentriertes Arbeiten ermöglichte. Unsere Techniker Conny, Uli, Tom und Michael sollten nicht vergessen werden, die stets zur Stelle waren und das Ihre beitrugen damit die vielen kleinen und größeren Probleme, die es bei experimenteller Arbeit immer geben wird, beseitigt wurden oder gar nicht erst auftraten.

Einige Kollegen kamen auch in das zweifelhafte Vergnügen mein wirres Geschreibsel verständlicher machen zu dürfen. Euch allen danke ich herzlichst! Es waren dies: Paula, Silvia, Ursula, Jonathan, Basti, Andi und Didi.

Meinen Eltern, Schwiegereltern, Familie und Freunden möchte ich für die tolle Unterstützung und den mir bereiteten Weg ganz besonders herzlich danken!

Diese ganzen Seiten wären sicher nicht gefüllt wenn da nicht noch jemand im Hintergrund steht und mich mehr als unterstützt - Ursula! Sie war der Zündfunke dieser Arbeit und hielt mit Rat und Erfahrung den Motor am laufen! Oftmals waren dazu ordnende Gespräche mit viel Kaffee nötig um mich aus den Tiefen des Reinraum/REM/AFM Waldes zu holen oder meinen Blick nach vorne zu richten! Ich sag "meinem persönlichem Post-Doc" ein ganz herzliches Dankeschön für alles was ich (auch persönlich) lernen durfte und darf! Zugleich hast Du auch privat für etwas Abstand zur Physik gesorgt. Dies alles ist einfach unbeschreibbar - ich bin dankbar und glücklich mit Dir in dieselbe Richtung blicken zu dürfen und freu mich, dass wir uns dahin gemeinsam auf den Weg machen!

## Danke!